

DEVELOPMENT OF PLASMA ASSISTED IGNITION FOR WAVE ROTOR
COMBUSTION TURBINE

A Dissertation

Submitted to the Faculty

of

Purdue University

by

Ravichandra R. Jagannath

In Partial Fulfillment of the

Requirements for the Degree

of

Doctor of Philosophy

August 2019

Purdue University

West Lafayette, Indiana

THE PURDUE UNIVERSITY GRADUATE SCHOOL
STATEMENT OF DISSERTATION APPROVAL

Dr. Sally P. M. Bane, Chair

School of Aeronautics and Astronautics

Dr. M. Razi Nalim

School of Mechanical Engineering

Dr. Sergey Macheret

School of Aeronautics and Astronautics

Dr. Carson Slabaugh

School of Aeronautics and Astronautics

Approved by:

Dr. Weinong Chen

Head of the School Graduate Program

To my affectionate dog Freddie

ACKNOWLEDGMENTS

It's been a long journey and several people have helped me during this journey. I would like to first start by thanking my advisor, Professor Sally Bane who has been an excellent PhD advisor. Professor Bane has always encouraged me to pursue fundamental research problems and has been extremely patient while I worked on these problems. This is a hard quality to have in a world filled with Professors putting pressure on students to solve problems and publish papers in quick time. For someone with no prior background in experiments, she has shown great confidence in my abilities and trusted me to setup several different experiments throughout my PhD. I am really lucky to have an advisor like Professor Bane.

I started my PhD working on a device called wave rotor which involved some complicated gas dynamics. I had a great co-advisor in Professor Razi Nalim who was an expert in wave rotor physics and unsteady gas dynamics. He helped me take small steps to understand the big picture.

I would like to thank Professor Macheret and Professor Slabaugh for being part of committee. I have always enjoyed my interactions with them. Both have been kind enough to share their knowledge on plasma physics and combustion. I would also like to thank Professor Sullivan for teaching me schlieren and different aspects of aerodynamics while building the wind tunnel force balance during the summer of 2017. I would also like to thank Professor Heister, Professor Blaisdell and Professor Lucht for being great instructors. Professor Lucht has been a great motivation for me to understand lasers, non-linear optics and spectroscopy.

My most important acknowledgement goes to Dr. Aman Satija for sharing his knowledge on spectroscopy and making me a good experimentalist. He made me pay attention to detail in every experiment. I learnt a lot about optics and optical alignment from Aman. He would pose several scientific questions during the experiment,

which improved my understanding on the subject. He has explained the working of lasers, cameras and different spectroscopy experiments. I really enjoyed working with Aman and interactions with him. I can say for sure that it was the best year of my PhD. I am really lucky to have worked with Aman. I would also like to thank Ming-ming and Dustin for some wonderful scientific interactions during my experiments at ME-B102.

I have been part of a wonderful research group here at Purdue. Each member of the group has been supportive of the other and have enjoyed the success of every member in the group. I would like to acknowledge James, Prashanth, Angie, Lalit, Bhavini, Kyle, Paul and Nadia for being supportive labmates. I would like to thank Shanmukesh, Lalit and Harshad for being great friends. I had some wonderful roommates during the first few years at Purdue, so a word of acknowledgement goes out to Karthik Kamanna, Abhinav Chandrappa, Ganesh Gingade, Mahesh Ramesh, Pramod Magadi and Nishanth Swaroop for that. I am grateful to have some wonderful friends like Ashwin, Praveen, Hemant, Anup, Rajeshwar, Sarang, KJ and Mehul from BMSCE who have been with me through ups and downs of undergraduate life.

Finally I would like to thank my parents for supporting me through my PhD. They have made a lot of sacrifices to help me achieve my goal. I would like to thank my wife Suchitra and her parents for being patient and encouraging me to finish my PhD. I would like to thank my Grandmother, Prasanna uncle, Ashok uncle and Rattan uncle for their constant support during my schooling and PhD. I would like to thank Kailash and Jois Uncle for being great role models for me while growing up. I would also like to thank Latha Atthe for her love and affection. I would like to thank Subramanyam uncle and Uma aunty for their encouragement. I haven't missed family and Indian festivities over the last 6 years thanks to Vamshi, Sowmya, Kushal, Giri and Nethra, I am lucky to have such wonderful family away from home.

I would like to thank the School of Aero and Astro for providing funding through the numerous teaching assistantships during my PhD.

TABLE OF CONTENTS

	Page
LIST OF TABLES	ix
LIST OF FIGURES	x
ABSTRACT	xvi
1 Motivation and Objective	1
2 Development of Computational Tool for Non-Axial Wave Rotors	10
2.1 Literature Review	10
2.2 Numerical Model for Wave Turbines	15
2.2.1 Conservation Equations for a Wave Turbine	15
2.2.2 Incidence Loss at the Wave Rotor Inlet	24
2.2.3 Shaft Work Estimation	26
2.3 Verification of Numerical Model using Non-Reacting Flow Simulation	31
2.3.1 Single Port Wave Rotor	32
2.3.2 Three Port Wave Rotor	37
2.4 Application of Numerical Model for Wave Rotor Combustion Turbine	51
2.4.1 Axial Channel Wave Rotor Combustor With Correct Port Timing	51
2.4.2 Non-Axial Channel Wave Turbine Combustion	55
2.4.3 Shaft Work Estimation for Wave Turbine Combustor	61
2.5 Identification of Potential Technology Needed to Improve Wave Rotor Combustion Turbine	63
3 Design of Plasma Actuator for Volumetric Ignition	66
3.1 Pin-Annular electrode discharge characterization	67
3.1.1 Simultaneous ICCD and Schlieren imaging	73
3.1.2 Studying the effects of electrode polarity	79

	Page
4 Development of a novel experimental technique for making ultrafast measurements of plasma discharges	90
4.1 Introduction to Streak Camera and its Working Principle	90
4.2 Need for Streak Camera Based System to Study Plasma Discharges	93
4.3 Characterization of Experimental System Using a CW LightSource	95
4.3.1 Experimental System	95
4.3.2 Timing and Trigger System(excluded part of psst paper)	98
4.3.3 Results	99
4.4 Characterization of the Streak Camera System With CW LED Light	99
4.5 Time Resolved Imaging of Plasma Luminescence using Streak Camera	101
4.5.1 Effect of Electrode Gap	102
4.5.2 Effect of Pulse Width	104
4.5.3 Effect of Pulse Voltage	105
4.6 Time Resolved Optical Emission Spectroscopy for Lifetime and Temperature Measurements	107
4.6.1 Lifetime Measurements of Excited Nitrogen Created from Plasma Discharge	107
4.6.2 Ultrafast Heating from the Plasma Discharge	108
5 Demonstration of Plasma Assisted Ignition Inside Constant Volume Vessel	113
5.1 Literature review	113
5.2 Experimental System	119
5.3 Study of Plasma Assisted Ignition for Pin-Pin Discharges	122
5.4 Study of Plasma Assisted Ignition for Pin-Ring Discharges	126
5.5 Discussion of Flame Dynamics	130
6 Summary	143
7 Recommendations for Future Work	148
7.1 Wave Rotor Combustion Turbine Development	148
7.2 Use of Streak Camera for Future Measurements	149
7.3 Improvement to Plasma Assisted Ignition	150

REFERENCES 151

LIST OF TABLES

Table	Page
2.1 Input variables for wave rotor emptying process	34
2.2 Three-Port Divider Cycle Parameters	39
2.3 Three-Port Divider Cycle Parameters	47
2.4 Opening and closing locations of the ports and the inlet duct angle for different blade geometries	57

LIST OF FIGURES

Figure	Page
1.1 Comparison of Temperature-Entropy diagram of Humphrey and Brayton cycle [1]	2
1.2 A comparison of electronic temperature and electron number density of different plasma discharges [2]	4
1.3 A schematic describing the pathway for combustion enhancement by plasma discharges [2]	5
2.1 Experimental measurements and computational predictions of pressure ratio for a four-port wave rotor [14]	14
2.2 Unwrapped view of the three-port wave rotor with internal waves and velocity diagrams [15]	14
2.3 Schematic of a slanted or staggered straight wave rotor channel [31]	18
2.4 Schematic of a non-staggered symmetrically curved wave rotor channel [31]	19
2.5 Schematic illustrating the relative frame inflow angle of the flow at the wave rotor inlet [12]	24
2.6 Control volume used for estimating work output for the wave rotor and the channel geometry	28
2.7 Velocity triangles for (a) positive and (b) negative blade angle	30
2.8 Wave rotor geometry for code verification. (a) Axial channels; (b) Staggered and (c) Symmetric arc [20]	33
2.9 Axial velocity profile at the exit of wave rotor for the emptying process. . .	35
2.10 Variation of exit velocity profile with blade stagger angle	37
2.11 Variation of exit velocity profile due to change in blade camber	37
2.12 Mean channel pressure as a function of angular position of channel for different grid densities	41
2.13 Pressure at middle of the channel as a function of angular position of channel at different grid densities	42

Figure	Page
2.14 Velocity at inlet for three computational time steps. Zoomed-in view shows the shock wave timing at 108° and expansion wave profile at $159-162^\circ$. . .	43
2.15 Velocity at the outlet for three computational time steps.	43
2.16 Shaft power due to incidence mismatch for an axial channel	44
2.17 Relative frame inflow angle as a function of angular position of the channel for an axial-channel three-port wave rotor	45
2.18 Axial velocity, temperature and the logarithm of pressure for an axial-channel three-port wave rotor with optimal duct angle	46
2.19 Relative frame inflow angle with respect to channel inlet angle for $+30^\circ$ to -30° symmetric blade wave turbine	48
2.20 Axial velocity, Temperature and Log of Pressure (all non-dimensional) for three-port wave turbine with $+30^\circ$ to -30° symmetric parabolic blade and optimal duct angle	49
2.21 Shaft power due to flow turning in a wave turbine with symmetric blades .	50
2.22 Internal gas dynamics of wave rotor with internal combustion	52
2.23 Inlet side stagnation pressure as a function of angular position of channel .	53
2.24 Contour plot of mixture fraction of fuel, intermediate and oxidizer species .	54
2.25 Inlet side velocity as a function of angular position of channel	55
2.26 Inlet incidence angle as a function of angular position of channel	55
2.27 Velocity, Temperature and Pressure for full cycle axial channel wave rotor with internal combustion	56
2.28 Axial velocity at the inlet for different blade profiles	58
2.29 Velocity, Temperature and Pressure contour plots for wave turbine combustion simulation with blade angle of negative 15°	59
2.30 Species fraction for wave turbine combustion simulation with blade angle of negative 15°	59
2.31 Static pressure at inlet plane, mid-channel and exit plane of the wave rotor for axial and 15° blade.	60
2.32 Static pressure at inlet plane, mid-channel and exit plane of the wave rotor for axial and 30° blade.	61
2.33 Shaft work estimates for wave turbine combustion for blade exit angles ranging from 0 to -30°	62

Figure	Page
3.1 The different regimes of discharge integrated over 200ms of discharge time	67
3.2 Schematic of initial experiment for imaging plasma formation in quiescent non-reactive environment at atmospheric pressure	70
3.3 The three different regimes observed when a burst of 500 pulses is used to create discharge in pin-ring electrode	71
3.4 Energy per pulse at different applied voltages, repetition frequency and pulse width	71
3.5 The different regimes of discharge integrated over 10ms of discharge time .	72
3.6 The different regimes of discharge integrated over 200ms of discharge time	73
3.7 Spinning of positive polarity discharges recorded on a high speed camera at 10000 FPS	74
3.8 Experimental setup for simultaneous schlieren and iccd imaging	75
3.9 Long exposure iccd image for a 10ms discharge at 1kHz and gas expansion observed through schlieren at different intervals of time	76
3.10 Long exposure iccd image for a 10ms discharge at 100kHz and gas expansion observed through schlieren at different intervals of time	77
3.11 Long exposure iccd image for a 200ms discharge at 100kHz and gas expansion observed through schlieren at different intervals of time	78
3.12 Negative polarity discharge with central electrode as cathode and pulser input voltage=14.6 kV	82
3.13 Positive polarity discharge with central electrode as anode and pulser input voltage=14.6 kV	83
3.14 Negative polarity discharge with central electrode as cathode and pulser input voltage=16.7 kV	84
3.15 Positive polarity discharge with central electrode as anode and pulser input voltage=16.7 kV	85
3.16 Negative polarity discharge with central electrode as cathode and pulser input voltage=18.75 kV	86
3.17 Positive polarity discharge with central electrode as anode and pulser input voltage=18.75 kV	87
3.18 Negative polarity discharge with central electrode as cathode and pulser input voltage=20.8 kV	88

Figure	Page
3.19 Positive polarity discharge with central electrode as anode and pulser input voltage=20.8 kV	89
4.1 Schematic to show internal working principle of a streak tube [54]	92
4.2 Schematic of the experimental system for Streak-Direct Imaging of NRP plasma discharges [61]	96
4.3 Schematic of the experimental system for streak-OES of NRP plasma discharges [60]	97
4.4 Schematic of the experimental system for streak-OES of NRP plasma discharges [61]	99
4.5 Streak image of a constant intensity Light Emitting Diode (LED) at intensifier gain setting of 20, 30, 40 and 50	101
4.6 Characterization of the Streak Camera System	102
4.7 Streak camera imaging of a pin to pin single plasma discharge with 3 mm electrode gap, 25 kV breakdown voltage and 100 ns pulse duration	103
4.8 Streak camera imaging of a pin to pin single plasma discharge with 1 mm electrode gap, 25 kV breakdown voltage and 100 ns pulse duration	104
4.9 Streak camera imaging of a pin to pin single plasma discharge with 3 mm electrode gap, 25 kV breakdown voltage and 100 ns pulse duration	105
4.10 Streak camera imaging of a pin to pin single plasma discharge with 3 mm electrode gap, 25 kV breakdown voltage and 75 ns pulse duration	105
4.11 Streak camera imaging of a pin to pin single plasma discharge with 3 mm electrode gap, 25 kV breakdown voltage and 50 ns pulse duration	106
4.12 Streak camera imaging of a pin to pin single plasma discharge with 3 mm electrode gap, 25 kV breakdown voltage and 35 ns pulse duration	106
4.13 Streak camera imaging of a pin to pin single plasma discharge with 3 mm electrode gap, 17.5 kV breakdown voltage and 100 ns pulse duration	107
4.14 Accumulated streak spectrum of a single plasma pulse with temperature fits at $t = 8.6, 9.8,$ and 13.4 ns	110
4.15 Time resolved rotational temperature at PRF of 5, 20 and 50 kHz for pin-to-pin electrode with 1 mm electrode gap	111
4.16 Time resolved vibrational temperature at PRF of 5, 20 and 50 kHz for pin-to-pin electrode with 1 mm electrode gap	112

Figure	Page
5.1 Fuel consumption for different fuels as a function of temperature (a) with plasma and (b) without plasma. CH_4 (triangle), C_2H_6 (square), C_3H_8 (right angle triangle), C_4H_{10} (diamond), C_7H_{16} (circle)	117
5.2 Plumbing diagram for plasma assisted ignition	121
5.3 Schematic of the vessel used for ignition experiments	122
5.4 Optical setup for plasma assisted ignition experiment	122
5.5 A schlieren image to explain the objects in the field of view	124
5.6 Schlieren images of flame development at 0.1, 2, 4, 6, 8 and 10 ms for pulse repetition frequency of 5 kHz	125
5.7 Schlieren images of flame development at 0.1, 2, 4, 6, 8 and 10 ms for pulse repetition frequency of 10 kHz	126
5.8 Schlieren images of flame development at 0.1, 2, 4, 6, 8 and 10 ms for pulse repetition frequency of 20 kHz	127
5.9 Schlieren images of flame development at 0.1, 2, 4, 6, 8 and 10 ms for pulse repetition frequency of 50 kHz	128
5.10 Binary images of flame development at 0.1, 2, 4, 6, 8 and 10 ms for pulse repetition frequency of 5 kHz	129
5.11 Comparison of radius evolution as a function of time for the different pulse repetition frequencies for the pin to pin electrode configuration	130
5.12 Flame propagation speed as a function of energy deposited per plasma pulse	131
5.13 A schlieren image to explain the objects in the field of view	132
5.14 Schlieren images of flame development at 0.3, 2, 4, 6, 8 and 10 ms for pulse repetition frequency of 5 kHz	133
5.15 Schlieren images of flame development at 0.1, 2, 4, 6, 8 and 10 ms for pulse repetition frequency of 10 kHz	134
5.16 Schlieren images of flame development at 0.1, 2, 4, 6, 8 and 10 ms for pulse repetition frequency of 20 kHz	135
5.17 Schlieren images of flame development at 0.1, 2, 4, 6, 8 and 10 ms for pulse repetition frequency of 50 kHz	136
5.18 Binary images of flame development at 0.1, 2, 4, 6, 8 and 10 ms for pulse repetition frequency of 50 kHz	137
5.19 Comparison of radius evolution as a function of time for the different pulse repetition frequencies for the pin to ring electrode configuration	138

Figure	Page
5.20 Flame propagation speed as a function of energy deposited per plasma pulse for the pin to ring electrode	139
5.21 Flame speed comparison for the two electrode configurations at different pulse repetition frequencies	140
5.22 The main reactions for hydrogen nitrogen and oxygen mixture [2]	141
5.23 The main reactions for a hydrocarbon ignition [2]	142

ABSTRACT

Jagannath, Ravichandra R. PhD, Purdue University, August 2019. Development of Plasma Assisted Ignition for Wave Rotor Combustion Turbine. Major Professor: Sally P. M. Bane.

Gas turbines are important for power generation and aircraft engines. Over the past century, there has been improvements in components of the gas turbine such as compressors, turbines and nozzles, but very little progress has been made in combustor technology. The combustion still occurs at constant pressure and the only changes made are in terms of its design and mixing of fuel and air streams. These design changes have only allowed minimal improvements in gas turbine efficiency. To achieve a substantive improvement in efficiency, it is required to make a technology change such as the introduction of constant volume combustion.

In this work, one such constant volume combustion device in the form of wave rotor combustion is studied and further developed for use in gas turbines. Wave rotors are periodic-flow devices that provide dynamic pressure exchange and efficient energy transfer through internal pressure waves generated due to fast opening and closing of ports. In addition, there is also confined high speed turbulent deflagration. If the blades are curved, then the flow undergoes angular momentum change from inlet to outlet, generating shaft work. This will allow maximum extraction of work potential from the wave rotor. In addition, an attempt is made to check the applicability of plasma assisted ignition for wave rotors.

A computational tool is developed to understand physics of non-axial channel wave rotors. The governing equations are formulated in one dimension through a passage average approach. Shaft work is estimated using conservation of angular momentum and energy to verify the working of numerical model. The model shows

increase in shaft work with increase in blade curvature, but as the angle is increased, the possibility of igniting the reacting mixture becomes difficult since it is hard to move the mixture towards the ignition port.

An alternate ignition source using plasma discharges is investigated through experiments. Two experiments are developed, one to make ultrafast measurements of plasma properties such as gas heating and lifetime of electronically excited molecules, and a second experiment to understand ignition characteristics of a pin to ring electrode configuration. The experiments show that excited nitrogen which reacts with molecular oxygen to form atomic oxygen is short lived and forms oxygen atoms extremely rapidly. This rapid formation of oxygen atoms assists in fast ignition. The ignition experiment with pin to pin electrode showed that even though there is fast ignition, the propagation speed does not change significantly with pulse repetition frequency. Ignition with pin to ring electrode showed fast ignition and increase in flame speed with pulse repetition frequency. Results show that plasma discharge can be used as an ignition source for wave rotors but will need further investigation.

The development of computational tool and plasma discharge experiments has provided a solid base for future efforts in wave rotor combustion and design of full scale non-axial wave rotor combustor experiment.

1. MOTIVATION AND OBJECTIVE

In any commercial aircraft, the propulsion system has a compressor, combustor, turbine and a nozzle to generate thrust. There have been tremendous advances in both compressor and turbine technologies. Combustors, however, have been exclusively designed to operate at constant pressure, which causes appreciable loss in work potential. There has been minor changes to the combustor designs such as introduction of swirling flow and premixed gases, but these changes can only improve the efficiency of aircraft engines by only a few percentage points. It has become clear that new and novel combustor technologies are required to significantly improve performance. Two candidate technologies for drastic improvement of combustor performance are pressure gain combustion and plasma-assisted combustion. These two approaches are the subjects of this PhD thesis and are investigated through computational and experimental work.

A pressure gain combustion system follows the Humphrey cycle and can be represented using a temperature-entropy diagram as shown in Figure 1.1. In this cycle diagram, the process 1-2 is compression, 2-3 is heat addition which is at constant volume for the Humphrey cycle and constant pressure for the Brayton cycle and process 3-4 is expansion of the gas. It can be observed from the temperature-entropy diagram that in the case of Humphrey cycle, the entropy gain is lower, peak pressure and thermal efficiency are higher. A wave rotor is one such device that follows the Humphrey cycle where the gas entering the rotor is compressed due to the shock wave generated inside the rotor. If the device is designed as combustor, the gas undergoes confined pressure gain combustion followed by expansion at the exhaust port. However, if it is designed as a pressure exchanger, then high pressure gas exits the rotor due to expansion waves generated at the exhaust port.

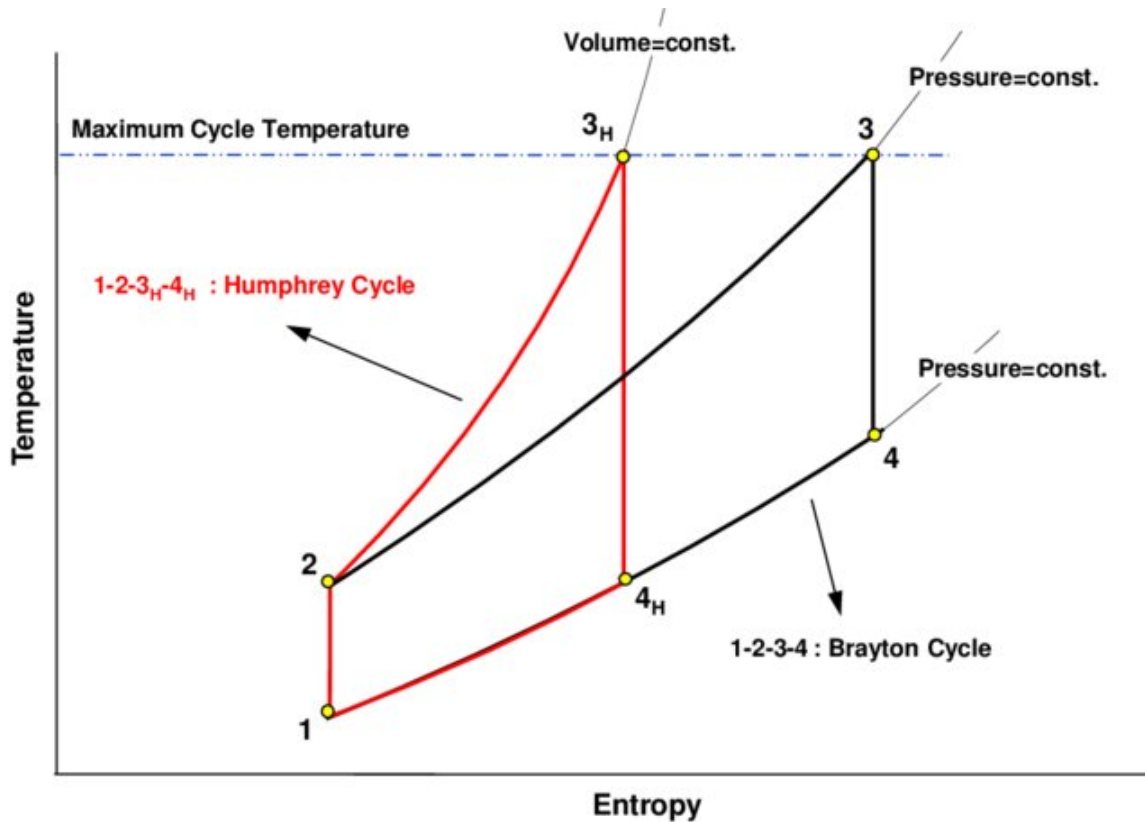


Fig. 1.1.: Comparison of Temperature-Entropy diagram of Humphrey and Brayton cycle [1]

Wave rotor combustors is a type of pressure gain combustion system that can operate either in detonation mode or fast deflagration mode, but it is preferred to operate in the fast deflagration mode. A wave rotor combustor consists of multiple passages arranged around the circumference of a shaft and housed within a rotating drum. The drum rotates between two stationary end plates, each of which has ports to control fluid flow through the passages. While the drum is rotating, the passages are periodically exposed to fluid flow through the ports. The sudden opening and closing of the ports initiate compression and expansion waves within the channels. The reacting gas mixture which is pre-compressed by these waves is ignited at one end, and the combustion wave propagates towards the opposite end and the combusted gas

is then purged out through the exhaust port. When the passages of the wave rotor are straight, the fluid does not change direction from inlet to outlet, which means there is no net change in angular momentum that can provide shaft work. Ideally when the passages are curved, the fluid tends to follow the curved path, resulting in change in angular momentum. This change in angular momentum generates shaft work from the wave rotor. Overall, the machine will provide pre-compression, combustion, expansion and shaft work in a single device, which could drastically improve efficiency of aircraft propulsion systems. In this work, the effect of curved passages on the wave rotor performance and its generation of shaft work is investigated.

A wave rotor combustor is a complex machine with many significant design challenges. One such challenge is reliable and efficient ignition of the reacting mixture. In a device that is spinning at thousands of revolutions per minute, a fast and reliable ignition source is needed such that the reacting mixture burns completely before it is expanded through the exhaust port. The pressure gain is lower, reducing performance and negatively affecting subsequent cycles. The existing method to initiate ignition is through a jet of hot turbulent gas which penetrates deep into the wave rotor channel. There are several challenges associated with this ignition method, including the need for a pre-chamber, prevention of leakage, and precise timing of the jet entry. In this research, an alternative technique, plasma assisted ignition is evaluated for applicability in wave rotor combustion.

Plasma can be observed in different forms such as flame, corona discharge, radio frequency discharge and nanosecond discharges. Nanosecond discharges have become important because they create a large pool of energetic electrons compared to other plasma sources as shown in Figure 1.2. These energetic electrons collide with surrounding molecules to produce electronically excited species. These electronically excited species assist in altering combustion kinetics, release heat when they relax to equilibrium and produce hydrodynamic flow over long time scales. The combination of kinetics, thermal and transport assist in combustion enhancement. A schematic describing the pathway of plasma enhancement in combustion is shown in Figure 1.3.

The advent of high voltage pulsers that can generate short duration high voltage pulses at high frequencies has promoted significant progress in plasma-assisted combustion research. Research has shown the use of plasma discharges can assist in fast ignition and combustion control through kinetic, thermal and hydrodynamic effects. For example, the unique kinetics of plasma discharges can permit ignition at much lower temperatures which can reduce NO_x. Plasma discharges have fast rise times in the order of tens of nanoseconds, they can be created at high frequencies, the timing of plasma can be controlled precisely and they don't require any mechanical parts like in the case of hot jet ignition. These advantages motivate the use of plasma discharges for wave rotor combustion.

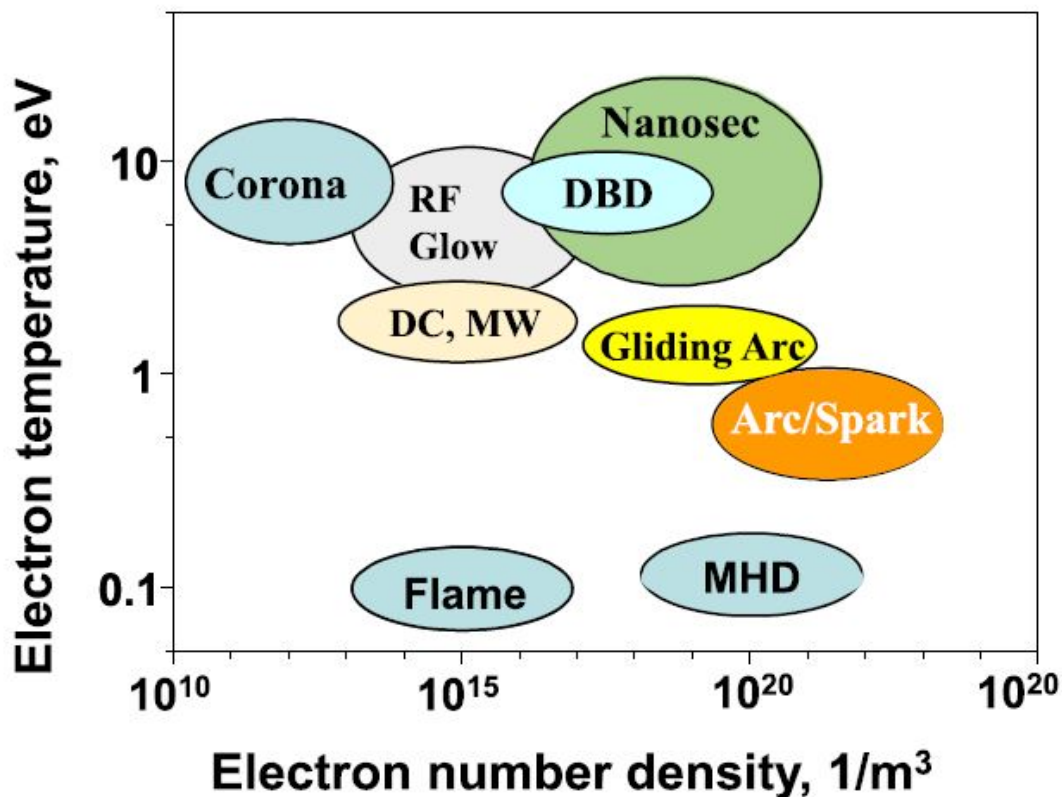


Fig. 1.2.: A comparison of electronic temperature and electron number density of different plasma discharges [2]

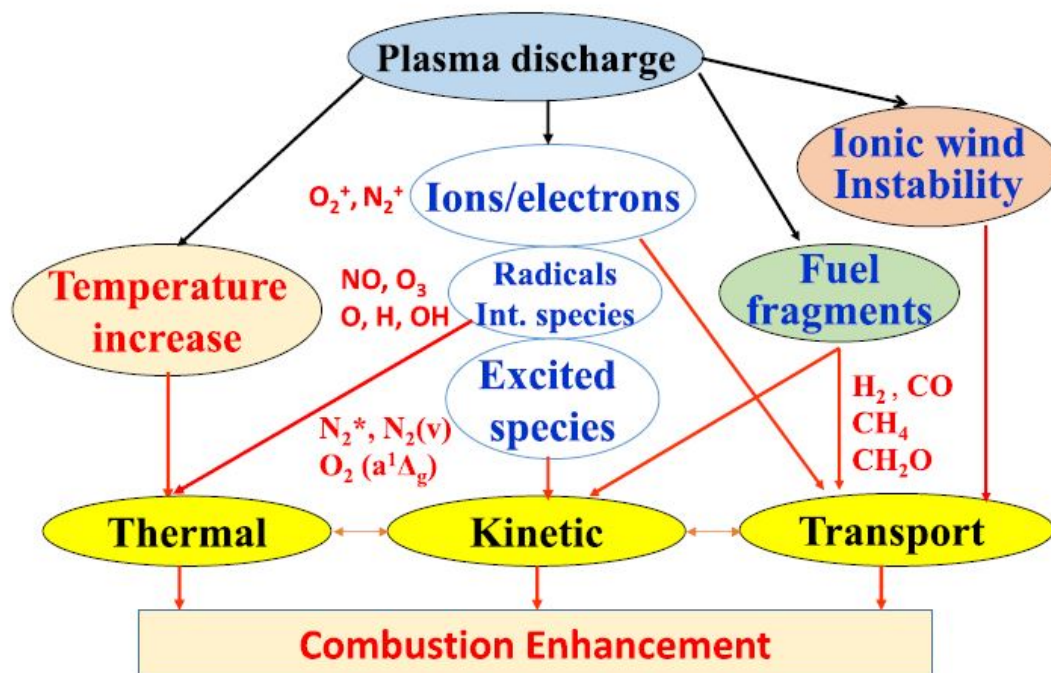


Fig. 1.3.: A schematic describing the pathway for combustion enhancement by plasma discharges [2]

Motivated by the need for improvement in wave rotor combustor design, including the techniques used for combustion initiation, four primary objectives were defined for this research:

1. **Develop a computational tool for non-axial wave rotors** - A wave rotor is a complex machine to design. The efficiency of the wave rotor depends on how the pressure waves are generated. These waves are generated due to instantaneous opening and closing of the ports and also the pressure ratio between inlet and exhaust ports. If these ports are opened or closed too early or late, it can result in flow reversal and leakage. The addition of combustion adds to the complexity of the device. It is required to trap the fuel air mixture within the wave rotor to maximize pressure gain. Performing experiments with such a

complex device requires a computational tool that simulates the flow physics of the wave rotor with different pressure ratios and port positions. This simulation can help optimize the wave rotor design for experiments, therefore minimizing time and expense.

A computational tool for the wave rotor was initially developed at NASA by Daniel Paxson for non-reacting flow, axial channel wave rotors. The numerical model was developed to accommodate 4 ports on either side of the wave rotor channel. In this model, the wave rotor was designed as pressure exchange device with external combustion. The model was later modified to have combustion inside the wave rotor. Transport equations for fuel, oxidizer and a simplified temperature based combustion model was used to simulate wave rotor with internal combustion. This model was used to design the axial channel wave rotor combustor experiment at Zucrow Labs. The next change for the wave rotor is the addition of curvature to the channels to generate internal shaft work. But the computational tool is limited to simulate axial channel wave rotors only.

The computational tool is now improved first to simulate a non-axial channel wave rotor and second to estimate the internal shaft work generated due to addition of blade curvature. Meeting the first object is slightly challenging. This is because the computational tool for axial flow is a quasi-1D model and addition of blade curvature will not provide 1-D flow, which means the same set of governing equations cannot be used. The governing equations will be written in channel average form to simulate flow physics of wave rotors with non-axial channel in 1-D. Second objective is to estimate the shaft work generated due to blade curvature. The shaft work is calculated using two different methods- conservation of angular momentum and conservation of energy. The computational tool will first be validated with simple expansion fan simulations from NASA and non-reacting three port divider cycle simulations. Since there are no experiments to validate the results, the two methods used for calculating

shaft work are used to verify the working of numerical model. Following these validations, the computational tool is used to simulate flow physics of reacting flow non-axial channel wave rotor combustor. The computational tool is used to optimize the inlet and exhaust port design for wave rotor combustor with different blade angles. Shaft work is then calculated using the two methods for numerical validation.

- 2. Design of plasma actuator for volumetric ignition** As mentioned previously, the potential for using plasma discharges for fast and reliable ignition in a wave rotor combustor is investigated in this work. Design of plasma actuator is critical for usage in the wave rotor. A wave rotor is rotating continuously at high speeds. This makes it hard to mount electrodes inside the wave rotor and make connections with high voltage power source. It is also important to mount the electrode in such a way that the rotation of wave rotor will not lead to breakage of electrodes. The design will therefore include a sharp pin electrode at high voltage mounted at the ignition port and the plasma will be formed from the pin electrode to the walls of the wave rotor channel. The pin electrode will be mounted flush with the ignition port opening. The walls of the wave rotor channel form a rectangular cross-section.

As a first step it is important to understand the functioning of the actuator. The actuator consists of a pin electrode and rectangular electrode. But for this preliminary design, a pin electrode and circular electrode are chosen. A lot of research in short duration plasma discharges have used a canonical pin to pin electrode geometry. In this type of electrode geometry, only one spark channel is formed. Changing the electrode configuration to pin and ring electrode provides a complex plasma discharge. This electrode configuration produces more number of spark channels compared to the pin to pin electrode configuration. The plasma formation depends on parameters such as pulse repetition frequency, pulse voltage, pulse duration and electrode gap. In the preliminary design of

the actuator, simple optical diagnostics like imaging the plasma discharge with intensified ccd camera and schlieren visualization of the induced flow are used to identify the different modes of operation of the plasma actuator and the hydrodynamic flow induced by these different modes.

3. **Development of a novel experimental technique for making ultrafast measurements of plasma discharges**

Plasma discharges used in this work and in general are ultrashort lasting few tens to few hundreds of nanoseconds. It is a well established fact that these ultrafast plasma discharges generate active radicals and electronically excited molecules. This is followed by a temperature rise of the surrounding gas which results in formation of the shock wave and hydrodynamic flow. When there is a reacting mixture to ignite, the active radicals generated by the plasma discharge produce new reaction pathways which help in initiating ignition faster. In order to understand the mechanism of plasma assisted ignition, it is important to make accurate measurements of these electronically excited molecules and the temperature rise induced by the plasma discharge.

Typically this measurement has been performed in the past using gated cameras or photo multiplier tube, both for direct imaging and optical emission spectroscopy. It is difficult to perform time resolved measurement with such instruments because they only provide part of the information from a plasma discharge. The camera is delayed to obtain sequence of images from multiple discharges, providing time resolved information. Such measurements are inherently uncertain because of electronic jitter.

To eliminate electronic jitter in the measurements and also to make single shot measurement of the entire emission from a single plasma discharge, a novel experimental technique is developed with a streak camera to directly image a plasma discharge and to perform optical emission spectroscopy (OES) measurements of plasma species and temperature. This experimental technique allows

measurements with time resolution of few hundred picoseconds and is extremely precise.

4. **Development of experimental facility to investigate plasma-assisted ignition** Prior to using a plasma discharge on a full scale wave rotor, the ignition performance of the plasma actuators is assessed in a simple, stationary ignition experiment. An experimental facility is developed to study plasma assisted ignition, including an optically accessible combustion chamber with high voltage connections. High speed schlieren visualization is used to study the ignition and flame propagation. The potential for volumetric ignition is assessed by comparison of the newly-designed plasma actuators with a canonical pin-to-pin electrode configuration.

The first objective, namely the development and use of a computational model for non-axial wave rotors with and without combustion, is described in Chapter 2. The second objective, development and characterization of plasma actuators for wave rotor ignition are discussed in Chapter 3, the development of streak-camera based measurements which is the third objective is presented in Chapter 4, the development of experimental facility for plasma assisted ignition is discussed in Chapter 5. Finally the summary and recommendations for future work are discussed in Chapter 6 and 7.

2. DEVELOPMENT OF COMPUTATIONAL TOOL FOR NON-AXIAL WAVE ROTORS

2.1 Literature Review

Oscillatory and pulsatile flows are ubiquitous in nature, and the potential for using unsteady flows in a wide range of engineering applications has long been recognized. One of the earliest uses of pulsatile flow was during the World War II in the making of the German V-1 Flying Buzz Bomb. The V-1 used a pulsejet engine with a resonant design that maintained cyclic jet discharge, filling, and firing without ignition. However, the potential of unsteady flow devices has largely been neglected due to the substantive improvements in conceptually simple semi-static devices, steady-flow devices or crypto-steady devices, e.g. turbomachines [3]. Understanding and exploiting such unsteady flows would enable significant improvement of engines and thermodynamic cycles for various applications. Shock tubes and pulsed combustors (including pulse detonation engines) are well-known examples of unsteady-flow devices. A less well-known example is the wave rotor, a technology that has shown unique capabilities to enhance the performance and operating characteristics of a variety of engines and machinery utilizing thermodynamic cycles. Wave rotors utilize non-steady but periodic flow in multiple channels or passages to generate internal pressure waves that can perform efficient energy transfer. Due to their mechanical simplicity, self-cooling, and fast time response, wave rotors can be used in a wide range of applications. An additional benefit is the production of shaft work due to flow turning in non-axial wave rotor channels, which can be used to power other devices, for example a fan or compressor in a gas turbine engine.

In general, a wave rotor consists of a row of shrouded blades (forming a set of channels) mounted on a rotating drum. A stationary plate at each end of the drum

closely seals the channels except for port openings for inflow and outflow of channel gases to and from corresponding stator ducts. The number of ports per cycle of operation depends on the application; for example, a three-port wave divider has one inflow and two outflow ports, a three-port joiner cycle has two inflow and one outflow port, and a four-port pressure-exchange wave rotor has two inflow and two outflow ports. As the drum rotates, the gas in the channels is exposed to these ports in turn. The instantaneous opening of a port to a channel initiates a pressure wave that draws the gas into the rotor through an inflow port or pushes the gas out through an outflow port. In addition, the pressure differential between the port and the channel either drives a shock wave that compresses the gas in the channel or an expansion fan that expands the gas in the channel, and the end walls cause wave reflections that further change the pressure. A well-designed wave rotor operating at design speed is theoretically highly energy efficient due the fact that energy exchange occurs through precisely timed waves instead of mechanical components; however, the complex gas dynamics present some challenges for optimized design and practical use with predictable performance. For example, flow separation can occur at the channel inlet and across curved blades in the case of non-axial channels, but the effect can be mitigated by optimized design of the inlet duct and limiting curvature. Another potential issue is controlling thermal expansion and cooling of wave rotor channels. At typical operating conditions, the cycling frequency is high and channel walls reach a predictable equilibrium temperature distribution that is constant and moderate relative to peak gas temperature. This allows thermal management and clearance control to accommodate heating and expansion effects. In spite of the practical challenges, the efficient pressure and energy exchange along with simultaneous shaft work production set the wave rotors apart from standard turbomachinery. The wave rotor concept originated around 1928 with the filing of a patent in Germany to use a wave rotor as a dynamic pressure exchange device. The Brown Boveri Corporation (BBC) implemented the wave rotor in locomotive gas turbines and diesel engine superchargers. The most successful commercial implementation of wave rotors was

the Comprex, a supercharger developed by BBC used in Mazda diesel engine cars [4]. The wave rotor superheater high-enthalpy high-Mach wind tunnel made by Cornell Aero Labs was useful in testing spacecraft models for atmosphere re-entry. In the mid-1950s, the Ruston-Hornsby turbine company designed a wave rotor with helical channels to provide a turbine effect and generate internal shaft work. The rotor was tested over a wide range of operating conditions and was reported to produce 35 hp of shaft work. Later, General Power Corporation developed a pressure-exchange wave turbine for Ford Motor Company [5]. A thorough review of the history of wave rotor development and application is given in Reference [3].

Over the past 25 years, there has been renewed interest and research on wave rotors using progressively more advanced manufacturing and modeling capabilities [6–9]. In the 1980s Mathur et. al. developed a first order finite difference scheme to perform wave rotor cycle analysis [10]. In the early 1990s, significant progress on wave rotor development, both computationally and experimentally, was made by researchers at NASA GRC. A quasi-1d (Q1d) numerical model was developed to simulate the flow in axial-channel wave rotors [11]. The model includes multiple ports on each end with subsonic or supersonic inflow and outflow, partially open channels and inflow that is incident on the channel at a non-zero angle. Subsequent versions of the model included source terms to account for end-gap leakage, wall friction, heat transfer, turbulent eddy diffusion, fuel stratification and internal combustion [12]. Due to limited computational resources available at the time, most of the wave rotor simulations have been quasi-1d. A limited number of 2-D simulations were conducted [13]. Detailed simulation of wave rotor cycles in multi-dimensions is even now computationally expensive, time-consuming, and requires the use of multiple processors. Therefore, a quasi-1d simulation with empirical or semi-analytical models to capture effects of turbulence, heat transfer, friction, mass leakage, flow incidence, and partially open end effects was developed, allowing for efficient simulation of multiple cases with varying wave rotor geometry.

The model has been validated over a wide range of operating conditions by NASA GRC [14] and Nalim et. al [9] as shown on Figure 2.1. The model development was complemented by experimental efforts at both NASA GRC and Purdue University. A wave rotor with a three-port flow-divider cycle was developed at NASA for investigation of fundamental wave rotor physics and for calibration of the Q1d model for different loss mechanisms such as port opening time, friction, leakage and heat transfer [15]. With accurate calibration of such losses, the model can then be adapted to simulate any wave rotor with arbitrary port configurations. The three-port cycle acts as a flow divider where a certain fraction of the incoming flow undergoes compression to leave the rotor at a high pressure while the remaining flow undergoes expansion to leave the rotor at a low pressure. The internal gas dynamics of a three-port wave rotor are illustrated in Figure 2.2. The wave rotor can also be designed as a reacting flow device, resulting in pre-compression, mechanically confined constant-volume combustion and expansion in a single device. Nalim and co-workers have studied internal combustion wave rotors extensively through both computational and experimental work [9, 16–27].

The previous experimental and numerical work on wave rotor development focused on characterizing the wave processes that result in pressure exchange and on internal combustion, and therefore mostly concentrated on axial channels. As discussed earlier, a second major advantage of the wave rotor is the production of shaft work when curved channels are used, but little work has been done on developing or simulating such wave turbines. Experimental testing of multiple wave turbines with varying blade and stator duct geometries can be extremely costly. Therefore, the development of the numerical model is critical for efficient analysis of loss mechanisms, investigation of the wave dynamics for designing optimal port timings, and testing with a range of blade shapes, duct angles, and boundary conditions. The model can then be used to determine the optimal wave turbine designs for experimental investment. In the current work, the Q1d numerical model was extended to account for blade curvature

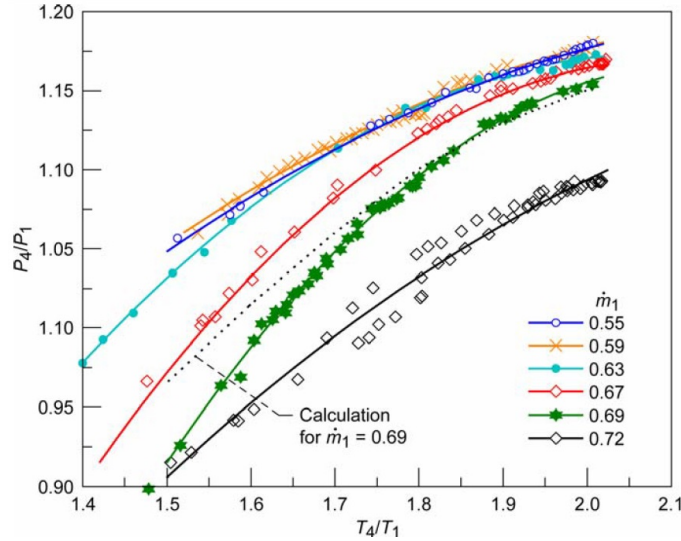


Fig. 2.1.: Experimental measurements and computational predictions of pressure ratio for a four-port wave rotor [14]

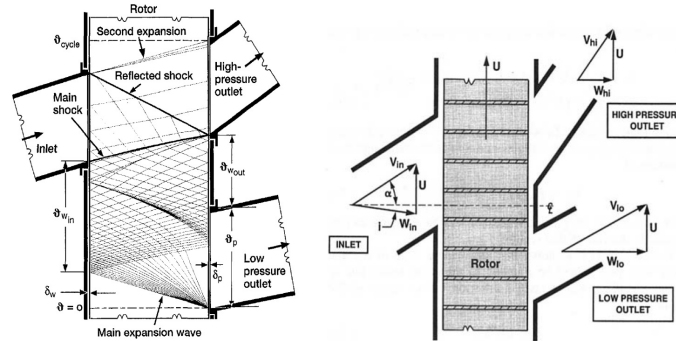


Fig. 2.2.: Unwrapped view of the three-port wave rotor with internal waves and velocity diagrams [15]

and the equations were modified to use the same numerical integration scheme as the axial flow model. A model to estimate losses due to flow incidence at the channel inlet [12] was also implemented. Then, a methodology for estimating the shaft work due to flow incidence and flow turning along the blades was developed. Finally, the extended model and the methodology for estimating shaft work was used to simulate a three-port divider cycle with axial and curved channels. The three-port divider

cycle is chosen as a first test case due to the extensive prior studies on this cycle performed at NASA, and also because it provides a case with both compression and expansion in a single device. The model is first used to simulate the three-port cycle with axial channels and the inlet duct design is determined to minimize incidence loss and incidence torque. The optimal inlet duct angle calculated for the axial channel is then incremented or decremented in subsequent simulations for curved channels to arrive at an optimal duct design for the non-axial channel. The shaft work is then estimated for the curved channel case, with minimal incidence torque.

2.2 Numerical Model for Wave Turbines

The available quasi-1d numerical model for wave rotors was limited to axial channels. Following prior work at NASA GRC [28, 29], the conservation equations are re-derived and implemented in the model to allow for blade curvature. A model for incidence loss at the wave rotor inlet [12] is also implemented. Finally, two methods for estimating shaft work are developed based on conservation of energy and of angular momentum.

2.2.1 Conservation Equations for a Wave Turbine

In this section, the re-formulation of the conservation equations to account for blade curvature is presented. First, the original model equations developed for axial channels are discussed, followed by derivation of the passage-averaged equations for non-axial channels. Finally, the passage-averaged equations are algebraically manipulated so they can be solved using the numerical scheme developed for axial flow.

Conservation Equations for Axial Channel Wave Rotors

The conservation equations used in the quasi-1d code for axial channels with variable axial cross-section $A(x)$ and constant mean radius are given by [19]:

$$\frac{\partial}{\partial t'} \begin{bmatrix} \rho' A'_c \\ \rho' A'_c u' \\ \rho' A'_c \left(\frac{p'}{\gamma \rho(\gamma-1)} + \frac{u'^2}{2} + \sum_{j=1}^3 z'_j q'_j \right) \\ \rho' A'_c z'_j \end{bmatrix} + \begin{bmatrix} \rho' A'_c u' \\ \frac{\rho' A'_c u'^2}{2} + \frac{p' A'_c}{\gamma} \\ \rho' u' A'_c \left(\frac{p'}{\rho(\gamma-1)} + \frac{u'^2}{2} + \sum_{j=1}^3 z'_j q'_j \right) \\ \rho' A'_c u' z'_j \end{bmatrix} = \psi \quad (2.1)$$

where the prime notation denotes a non-dimensional variable. The current work is focused on non-reacting flow, therefore the conservation equations for chemical species are not included here but are given in [19]. In general, the source vector ψ includes contributions from two categories of loss mechanisms: 1) friction, heat transfer to the walls and turbulent eddy diffusion effects throughout the length of the channel, and 2) radial and circumferential leakage only at the two ends of the channel [18]. A third category of loss mechanisms, which include end-region flow separation during periods of partial (gradual) opening of channels and due to flow incidence, are built into the application of boundary conditions, and thus not included in the source term. In general, the source vector ψ includes two components, the first part deals with friction, heat transfer, turbulence and species conversion to account for combustion. The second component consists of radial and circumferential leakage applied to channel boundaries. The source vector can be written as:

$$\psi = \psi^{int} + \psi_{rad}^{leak} + \psi_{cir}^{leak} \quad (2.2)$$

The contribution from friction, heat transfer, turbulence and species conversion can be written as:

$$\psi_{int} = \begin{bmatrix} 0 \\ \frac{\epsilon_t}{Re} \frac{\partial^2 u}{\partial x^2} + \sigma_2 u |\rho u|^{0.75} \\ \frac{\epsilon_t}{Re} \frac{\partial^2}{\partial x^2} \left(\frac{u^2}{2} + \frac{T}{(\gamma-1)Pr_t} + \sum_{j=1}^{n_s} \frac{z_j q_j}{Sc_t} \right) + \sigma_3 u |\rho u|^{0.75} (T - T_w) \\ \frac{\epsilon_t}{Re Sc_t} \frac{\partial^2 z_j}{\partial x^2} + \rho \min\left\{z_f, \frac{z_o}{A/F}, \frac{g_w z_I}{1+A/F}\right\} \left(\begin{cases} k_r, & \text{if } T \geq T_{ign} \\ 0, & \text{otherwise} \end{cases} \right) \end{bmatrix} \quad (2.3)$$

Where σ_2 is a semi-empirical correlation for friction source term and is proportional to the passage geometry and inversely proportional to Reynolds number of the the flow. The heat transfer source term σ_3 is derived from Reynolds-Colburn skin friction analogy. The non-dimensional terms for Reynolds number, Prandtl number and Schmidt number is represented by Re , Pr and Sc respectively. T_w is the wall temperature, ϵ_t is the turbulent eddy viscosity and z represents the species fraction and k_r the reaction rate. The leakage source term is shown by in reference [30].

Conservation Equations for Non-Axial Channel Wave Rotors

The conservation equations in 2.1 cannot be used for non-axial channels because they do not include blade forces and fluctuations along the spanwise and pitchwise directions which arise due to suction and pressure along the top and bottom surfaces of the blade. To account for these effects, the conservation equations for a channel of arbitrary curvature in the tangential and radial directions are averaged over the channel cross-section to reduce the number of spatial variables to one, hence reducing the three-dimensional equations to quasi-1d equations. The averaging of the governing equations is presented in detail by Welch et. al. [28], and the final channel averaged equations (not including loss source terms) [29] are given by:

$$\frac{\partial}{\partial t} \begin{bmatrix} \bar{\rho} A_c \\ \bar{\rho} A_c \bar{u}_x \delta^2 \\ \bar{\rho} A_c \bar{e}_I \end{bmatrix} + \begin{bmatrix} \bar{\rho} A_c \bar{u}_x \\ \bar{\rho} A_c \bar{u}_x^2 \delta^2 + \bar{p} A_c \\ \bar{\rho} A_c \bar{h}_I \bar{u}_x \end{bmatrix} = \begin{bmatrix} 0 \\ F_B + F_C \\ Q_C \end{bmatrix} \quad (2.4)$$

The overbar in the governing equations denotes an unweighted passage average and the double overbar denotes a density-weighted passage average [29]. The geometries for slanted and curved channels are illustrated in Figure 2.3 and Figure 2.4, respectively. The momentum equation involves axial, radial and tangential components, where the tangential and radial velocity components are written in terms of the axial component. This leaves a blockage term in the momentum equation. In general, the blockage term is a function of the blade angle and meridional angle and is written as $\delta^2 = 1 + \overline{\tan(\zeta)^2} + \overline{\tan(\phi)^2}$ [15]. The angle ζ is the local blade angle measured in the plane tangent to the axial-azimuthal (x-h) surface, relative to the rotor axial direction (x), and the angle ϕ is the meridional angle measured in the plane tangent to the axial-radial (x-r) surface, relative to the rotor axial direction (x). As shown in Figure 2.4, ϕ is measured with respect to the rightward horizontal, with counter-clockwise taken to be positive. The blade angle is constant for the slanted or staggered straight blade case and varies along the axial direction for the curved blade case.

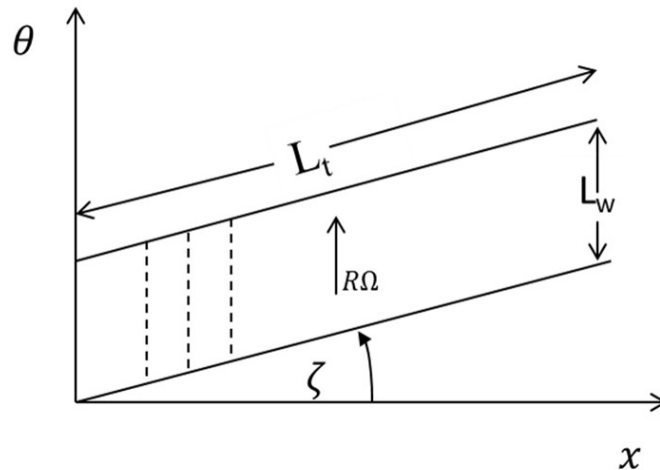


Fig. 2.3.: Schematic of a slanted or staggered straight wave rotor channel [31]

The source terms F_B and F_C represent blade forces and momentum correlation terms, respectively, and Q_C represents heat flux terms in W due to friction and heat transfer between the gas and the channel walls. The momentum source term

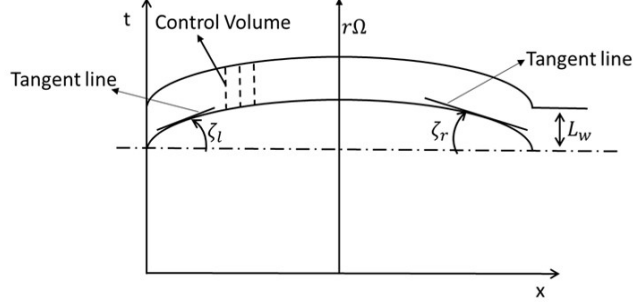


Fig. 2.4.: Schematic of a non-staggered symmetrically curved wave rotor channel [31]

F_C and heat flux term Q_C contain the correlation terms obtained from averaging the three-dimensional gas momentum and energy equations, which are nonzero when there are spanwise and pitchwise flow-field variations due to entropy gradients, local acceleration, and wave refraction. However, in the one-dimensional model, these terms can be neglected without obscuring the basic physics of the problem [15].

The momentum source term F_B is due to the blade force, which is important when there is change in angular momentum due to flow turning. The source term can be expressed in terms of pressure (p), area (A_c), and blade angle [15]:

$$F_B = \frac{\rho(\overline{u_x})(\overline{u_x})A_c}{2} \frac{\partial \delta^2}{\partial x} + \overline{p}A_c \left[\frac{\Delta_\theta(\tan(\zeta))}{\overline{r}(\theta_P - \theta_S)} + \frac{\Delta_r(\tan(\phi))}{(r_T - r_H)} \right] \quad (2.5)$$

Simplified Equations for Non-Axial Channel Wave Rotors

To solve the equations as written in 2.4, the entire numerical scheme used for an axial flow wave rotor would need to be altered as the equations in 2.4 are substantially different from the equations in 2.1 for axial flow. In the current work, the passage-averaged equations are manipulated algebraically such that the additional terms from blade curvature in the momentum equation are moved to the source vector and the left hand side of the equation becomes identical to 2.1. This will allow the model to retain the numerical scheme used for axial channels by simply adding extra terms to the source vector in the code.

The first step involves expressing the change in blade angle (ζ) and meridional angle (ϕ) in terms of the change in cross-sectional area along the axial direction, reducing Eq. 2.5 to the simpler form:

$$F_B = \frac{\rho(\overline{u_x})(\overline{u_x})A_c}{2} \frac{\partial \delta^2}{\partial x} + \overline{p} \frac{\partial A_c}{\partial x} \quad (2.6)$$

The averaged pressure in the momentum equation can be written in terms of the axial velocity component and rotational speed as

$$\overline{p} = (\gamma - 1)\overline{\rho}(\overline{\tilde{e}}_I - \frac{(\overline{u_x})(\overline{u_x})\delta^2}{2} + \frac{(\overline{r\Omega})^2}{2}) \quad (2.7)$$

where the local specific rothalpy is given by

$$\begin{aligned} \overline{\tilde{h}}_I &= \overline{\tilde{e}}_I + \overline{p}/\overline{\rho} \\ \overline{\tilde{e}}_I &= \frac{\overline{p}}{(\gamma - 1)\overline{\rho}} + \frac{(\overline{u_x})(\overline{u_x})\delta^2}{2} - \frac{(\overline{r\Omega})^2}{2}. \end{aligned} \quad (2.8)$$

Substituting Eq. (2.6-2.8) into Eq. (2.4) and normalizing using reference conditions for pressure (P/P^*), temperature (T/T^*), velocity (V/V^*), density (ρ/ρ^*), area (A^*/L^{*2}) and rotational speed ($\Omega L^*/a^*$). The reference velocity is the speed of sound at a reference temperature of 300K. The reference length is the length of the channel which is 31 inches and the reference pressure is 101325 Pa. The conservation equations can be written in the simplified form

$$\begin{aligned} \frac{\partial}{\partial t'} \left[\begin{array}{c} \overline{\rho}' A'_c \\ \overline{\rho}' A'_c U'_x \delta^2 \\ \overline{\rho}' A'_c \left[\frac{p'}{(\gamma-1)\rho'} + \frac{U_x^2 \delta^2}{2} - \frac{r' \Omega'^2}{2} \right] \end{array} \right] + \frac{\partial}{\partial x'} \left[\begin{array}{c} \overline{\rho}' A'_c U'_x \\ \rho' A'_c U_x^2 \delta^2 + \frac{p' A'_c}{\gamma} \\ \rho' A'_c \left[\frac{p'}{(\gamma-1)\rho'} + \frac{U_x^2 \delta^2}{2} - \frac{r' \Omega'^2}{2} \right] U'_x \end{array} \right] = \chi + \psi \\ \chi = \left[\begin{array}{c} 0 \\ \frac{\rho' U_x'^2 A'_c}{2} \left(\frac{\partial}{\partial x'} \delta^2 \right) + p' \left(\frac{\partial A'_c}{\partial x'} \right) \left(\frac{1}{\gamma} \right) \\ 0 \end{array} \right]. \end{aligned} \quad (2.9)$$

Once again, the use of prime variables in Eq. (2.9) indicates non-dimensional quantities and should not be confused with fluctuation terms used in turbulence models.

The reference conditions for normalizing the different variables are obtained at ambient conditions of 14.7 psi and 520° Rankine. It is assumed that the channels have a constant mean radius about which the hub and tip shroud are symmetric, the mean meridional angle is zero ($\tan(\phi) = 0$), and the blockage term can be written as $\delta^2 = 1 + (\tan(\zeta^2))$. When the rotor wheel speed Mach number is low, due to gradual opening of the channel to the port, there is flow distortion at the fluid contact interface which is moving behind the shock. At very high Mach numbers, there is radial distortion of this fluid contact interface due to the centripetal effect. An intermediate wheel speed Mach number is chosen so that both the gradual opening time effect and the centripetal effect can be minimized [32]. Therefore, the assumption of neglecting radial distortion is reasonable. For perfectly axial channels, $\tan(\zeta) = 0$ and $\delta^2 = 1$, thus reducing the governing equations to the classical quasi-1d equations in (2.1). The equations in (2.9) have additional terms in the momentum and energy equations as a result of the blade force due to flow turning and therefore could be difficult to implement in the original numerical scheme used to solve the equations for the axial flow case. To address this issue, the additional terms can be moved to the right-hand side of the momentum and energy equations through careful algebraic manipulations that account for how the equations are coupled. The terms are then combined with the source vector, leaving the left-hand side of the equations identical to (2.1), so that the numerical integration scheme used for axial channels can be used without change in the quasi-one-dimensional code. The final form of the conservation

equations with new definitions of the variables w , $f(w)$, and χ , obtained after the algebraic manipulations described above is given by:

$$\begin{aligned} & \frac{\partial}{\partial t'} \begin{bmatrix} \rho' A'_c \\ \rho' A'_c u'_x \\ \rho' A'_c \left[\frac{p'}{(\gamma-1)\gamma\rho'} + \frac{u_x'^2}{2} \right] \end{bmatrix} + \frac{\partial}{\partial x'} \begin{bmatrix} \rho' A'_c u'_x \\ (\rho' A'_c u_x'^2 + \frac{p' A'_c}{\gamma}) \\ \rho' A'_c \left[\frac{p'}{(\gamma-1)\rho'} + \frac{u_x'^2}{2} \right] u'_x \end{bmatrix} = \chi + \psi \\ \chi = & \begin{bmatrix} 0 \\ \frac{1}{1+\tan^2(\zeta)} \frac{-\rho' (u_x'^2) A'_c}{2} \frac{\partial(1+\tan^2(\zeta))}{\partial x'} + \frac{p'}{\gamma} \frac{\partial A'_c}{\partial x'} + \frac{1}{1+\tan^2(\zeta)} \frac{A'_c \tan^2(\zeta)}{\gamma} \frac{\partial}{\partial x'} (p') \\ -\rho' A'_c u'_x \frac{\partial}{\partial x'} \left[\frac{u_x'^2 \tan^2(\zeta)}{2} - \frac{(r'\Omega')^2}{2} \right] - \rho' A'_c \frac{\partial}{\partial t'} \left[\frac{u_x'^2 \tan^2(\zeta)}{2} - \frac{(r'\Omega')^2}{2} \right] \end{bmatrix}. \end{aligned} \quad (2.10)$$

The terms due to blade curvature have been moved to the right hand side as part of the source vector and the left-hand side is identical to that of Equation (2.1). The modified blade-force source vector χ is added to a modified loss source vector ψ to produce an overall source term vector. The contributions due to mass leakage, wall shear stress and heat transfer are not considered in this work; thus, the modified source vector ψ is not described here. Eq. (2.10) represents the general quasi-1d model for a wave turbine with curved blades of arbitrary profile.

The numerical model presented in this work is a single passage model and quasi-1d. It may not be able to capture the strong gasdynamic interaction between the rotor and port flow fields which is multidimensional. The incidence loss at the inflow plane is solved using a model that treats the incidence separation as a converging diverging nozzle. This is highly simplified, and does not consider that the separation bubble may extend a significant length into the channel. The blade force model developed in this work ignores some of the correlation terms that arise from averaging the conservation equations. The validity of ignoring these terms will need to be analyzed by including these terms and modeling them appropriately. Even with these modeling assumptions, the Q1d solver has been shown to predict the wave rotor performance with reasonable accuracy [14]. In addition, the Q1d model has correlations for its source terms that have been calibrated with previous experiments and therefore provide confidence in prediction with respect to experimental results, although not used in the present work. It is recognized that the incidence loss model requires improvement, possibly with the

use of multidimensional transient modeling of small scale separation phenomena that will be substantially more expensive than the current model.

Numerical Integration Scheme

This conservation equations for curved channels given in (2.10) are solved in a manner similar to the equations for an axial channel wave rotor using an explicit second-order Lax-Wendroff total-variation-diminishing (TVD) scheme with Roes flux-averaging technique to capture discontinuities. A total of 200 computational cells are used for the current work, which provides a non-dimensional computational cell size of 0.005. A short study was conducted to verify that the results are independent of cell size (for grid sizes of 200 cells and larger), details are given in Section 3. The non-dimensional time step was set to 0.001 to maintain a Courant number of 0.2 for numerical stability of the model. In prior work by NASA GRC, Eq. (2.4) and (2.5) were used in their model. This would mean the numerical integration scheme developed for axial channel had to be changed to account for additional terms due to blade curvature. In the current work, Eq. (2.4) and (2.5) were modified to Eq. (2.10) and solved using the same numerical scheme as axial channels. The modified equations for a wave turbine were verified against numerical predictions from NASA GRC [29] for the specific case of an expansion wave originating at one end of a non-axial channel, traveling through the length of the channel and reflecting at the end wall [20]. The results confirmed that in a non-axial channel the arrival of the wave after reflection from the end wall is delayed, consistent with the increased length of travel for the wave. Therefore, the port timing should be optimized for the specific geometry of the channel, including its length. For a straight, slanted channel, the gas axial velocity was verified to be proportional to the cosine of the blade angle, consistent with the wave strength for a given expansion pressure ratio. Further verification was also performed by setting the blade angle ζ to zero and verifying that the axial channel results could be reproduced.

2.2.2 Incidence Loss at the Wave Rotor Inlet

The gas flow into the rotor channel in the channel frame of reference is rarely aligned and most often enters at an angle with respect to the channel, called the relative frame inflow angle, i . The flow incidence leads to stagnation pressure loss at the inlet and flow separation may form a vena contracta as illustrated in Figure 5. As the flow turns to align with the channel direction it generates an incidence torque. In the case of a non-axial channel wave rotor, it is important to distinguish between torque contributions from incidence and from blade curvature. Since incidence results in total pressure loss, it is usually desirable to design the inlet duct to minimize the contribution due to incidence, i.e. minimize the relative-frame inflow angle. However, incidence can usually be minimized only on average over a given port and for a given operating condition, since the channel inlet velocity typically varies over the port and its distribution changes with operating conditions.

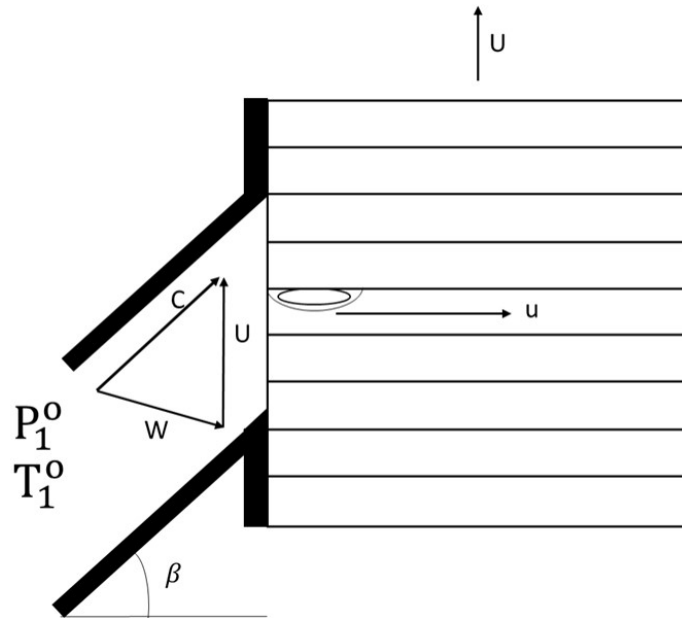


Fig. 2.5.: Schematic illustrating the relative frame inflow angle of the flow at the wave rotor inlet [12]

In the current work, the relative frame inflow angle is estimated as:

$$i = \tan^{-1} \frac{(\vec{U}_e \sin(\beta_{duct}) + \vec{\Omega R})}{\vec{U}_x} - \zeta_l \quad (2.11)$$

and the optimal duct angle is achieved when the relative frame inflow angle is zero in an average sense. The incidence turning is implemented in the wave rotor model by treating the vena contracta created by the flow separation bubble as a backward-facing step [12] occurring within a negligibly short distance from the inlet plane. The inlet stagnation pressure, stagnation temperature, and duct angle are provided as input boundary conditions, with the initial conditions in the first computational cell also known, while the flow velocity entering the channel from the inlet duct both in the channel frame of reference and stationary frame of reference are unknown. An initial guess is made for the static pressure in the duct and used in two ways to calculate the velocity entering the first cell after flow re-attachment in the channel. First, the velocity is found using conservation of mass, momentum and energy (entropy generation), by assuming isentropic nozzle flow from the inlet stagnations conditions to wall-parallel flow at the step, followed by reattachment. The height of the vena contracta and the downstream velocity is obtained based on whether or not the nozzle is choked. Second, the initial guess for the static pressure is used to calculate the velocity into the first computational cell using Roes approximate-Riemann flux-averaging method, similar to the method used to calculate the velocity between the interior cells in the channel. Any difference between the two values of velocity requires correction of the initially assumed static pressure by iteration until the two velocities are equal. Details of the method are given in [12]. The flow conditions determined through this iterative process are then used for the flow in the duct. Using the calculated flow conditions, the duct angle, and the rotational speed, the flow velocity in the stationary frame of reference and relative frame inflow angle, i can be calculated. The incidence torque and the rotor torque can be calculated using the flow conditions at the wave rotor inlet and exit using the methodology described in the following section.

2.2.3 Shaft Work Estimation

The gas undergoes changes in angular momentum due to flow incidence at the inlet as well as flow turning along the curved surface of the channel, resulting in work being transferred into or out of the gas to satisfy conservation of angular momentum. The gas also does work on the blades leading to a change in the stagnation enthalpy. If the system, consisting of a wave rotor blade channel in this case, is considered to be adiabatic with no heat transfer through its walls then the change in stagnation enthalpy must be equal to the work being transferred into or out of the gas to satisfy conservation of energy. Therefore, work transfer estimated through conservation of energy and conservation of angular momentum should be equal. Note that although the flow within the wave rotor is non-steady, it is periodic and so there is no net accumulation of angular momentum or energy over a complete cycle. Comparing the work transfer calculated using the two different methods provides an internal consistency check in the modeling, while validation of the model itself awaits experimental research.

Shaft Work Estimation using Conservation of Angular Momentum

The net rotor torque, which is the sum of incidence torque and torque due to flow turning, is calculated from the Euler work equation as the difference in angular momentum from the rotor inlet to the outlet, and the torque is multiplied by the rotor speed to get work rate or power. Because the velocity components and mass flux calculated using the computational model are non-dimensional, it is important to non-dimensionalize the torque in a similar manner. The contribution to the angular momentum flux, JF , for one channel over one cycle can be written as:

$$JF = RA_c \int_0^{t_{cy}} \rho u c_t dt \quad (2.12)$$

Using reference density ρ^* , reference speed of sound a^* , channel axial length L and reference time L/a^* to respectively non-dimensionalize density, velocity, channel radius and time in Eq. (2.12), the angular momentum flux can be written as:

$$JF = \frac{2\pi Rh}{N} \rho^* a^{*2} \frac{L}{a^*} L \int_0^{t_{cy}} R' \rho' u' c'_t dt' \quad (2.13)$$

where N is the number of channels in the rotor, R the channel mean radius, h is the channel height and L the channel length. The term inside the integral is the non-dimensional angular momentum flux through one port for a single channel over one cycle. The angular momentum flux can be expressed in terms of the non-dimensional flux, JF' :

$$JF = \frac{2\pi Rh}{N} \rho^* a^* \frac{L^2}{J} F' \quad (2.14)$$

The net torque for all ports over n_{cy} cycles per revolution, τ , is the difference in angular momentum flux from the inlet to the outlet:

$$\tau = \left(\frac{N n_{cy}}{t}\right) \frac{2\pi Rh}{N} \rho^* a^* L^2 [JF'(Port_{in}) - JF'(Port_{out})] \quad (2.15)$$

Writing the time for one revolution of the rotor as $\frac{2\pi}{\Omega}$ and normalizing the rotational speed using $\frac{L}{a^*}$ gives the final expression for the net torque:

$$\tau = Rh \rho^* a^{*2} L \Omega' [JF'(Port_{in}) - JF'(Port_{out})] n_{cy} \quad (2.16)$$

The shaft power P_{JF} is the product of rotor torque and angular velocity:

$$P_{JF} = Rh \rho^* a^{*3} \Omega'^2 [JF'(Port_{in}) - JF'(Port_{out})] n_{cy} \quad (2.17)$$

If the torque τ and rotational speed Ω are of opposite sign, work is transferred from the rotor to the gas similar to a compressor, and if they are of like sign, work is transferred from the gas to the rotor as in the case of a turbine.

Control Volume and Velocity Calculation

The work equation described in (15) requires calculation of tangential velocity components at the inlet and exit of the rotor. However, unlike traditional turbomachines, in the case of wave rotors a mean value for velocity cannot be used for

calculating work because the flow inside the wave rotor is non-steady. The presence of ports creates internal pressure waves leading to non-uniform velocity at the inlet and exit. Therefore, the instantaneous rate of work is estimated as a function of angular position of the channel and integrated across a cycle of rotation to calculate overall work transfer.

The flow work is estimated using a control volume approach with velocity triangles at the inlet and exit. The control volume, shown in Figure 2.6, encompasses the entire wave rotor and is assumed to have adiabatic walls with no external heat transfer in the present work.

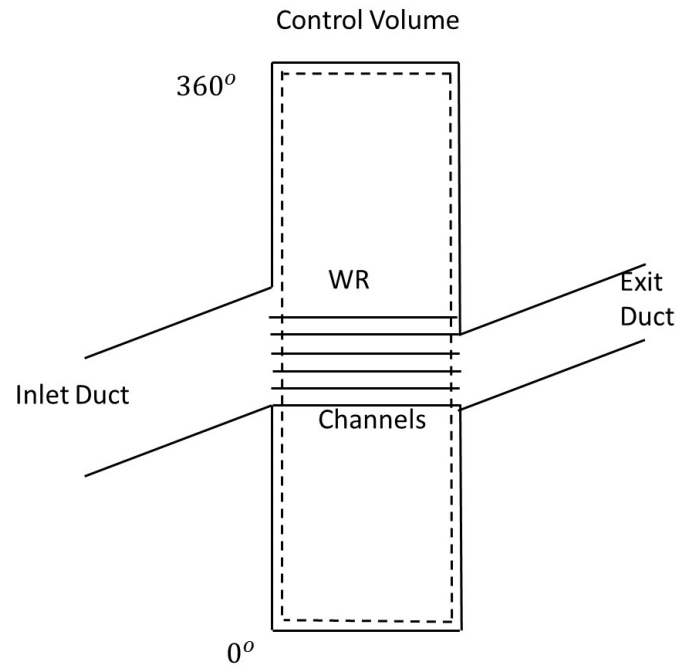


Fig. 2.6.: Control volume used for estimating work output for the wave rotor and the channel geometry

Velocity triangles are shown in Figure 2.7 for general cases of positive and negative ζ that may occur at either end of the channel. In the velocity triangles, c is the velocity in the stationary frame of reference, w is the velocity in the channel frame of reference, c_t and w_t are the tangential component of velocity in the stationary and channel frame

of reference, respectively, u is the axial component of velocity, and Ω and R are the rotational speed and channel mean radius of the rotor. The vector algebra of velocity triangles is applied at each end of the channel and for each computational time step as the channel completes one cycle of rotation. The duct angle β , blade angles ζ_r , ζ_l and rotational velocity ΩR are specified as design conditions. From the known conditions and the channel axial velocity distribution obtained at the end of simulation, the unknown velocity components in the velocity triangle can be calculated at each time step. When the flow is entering the channel (illustrated for the case of entry at the left end in Figure 2.7), the velocity components are calculated as follows:

$$c = \frac{u}{\cos(\beta)}, c_t = u \tan(\beta), w_t = c_t - \Omega R \quad (2.18)$$

The angle i , the relative frame inflow angle previously defined in Eq. (2.11), must be equal to zero on average to avoid incidence loss. When the flow is leaving the channel (illustrated for the case of exit at the right end in Figure 2.7), the velocity components are calculated using:

$$w_t = u \tan(\zeta_r), c_t = \Omega R + w_t, c = \sqrt{u^2 + c_t^2} \quad (2.19)$$

Shaft Work Estimation using Conservation of Energy

A numerical model must satisfy physical laws, be internally consistent, and ultimately validated through experiments. Many sub-models in the current model such as friction, heat transfer and mass leakage are based on empirical relationships calibrated from previous experimental research. Although these loss mechanisms are omitted in the current work, they will be needed in future efforts to provide the realism needed for experimental validation. The current model is passage-averaged to solve the governing equations in one dimension. Experimental testing is also needed to quantify the errors from this simplification in estimation of shaft work, mass flow rate, and other performance parameters. There are no reported experiments with non-axial wave rotors with details of boundary conditions to validate the present

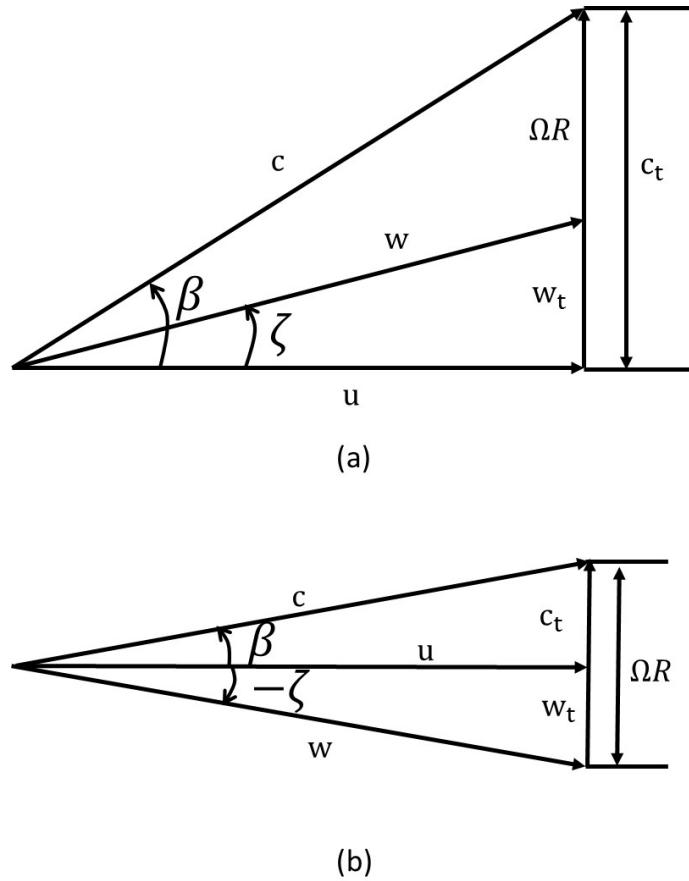


Fig. 2.7.: Velocity triangles for (a) positive and (b) negative blade angle

model. The present work includes a check of the internal consistency of shaft work calculation. In the previous section, the shaft work was estimated using the principle of conservation of angular momentum. A second estimate of the shaft work can be obtained using conservation of energy. If the numerical model is developed correctly, the two approaches should agree.

The second approach for calculating the shaft power uses the enthalpy change and conservation of energy. The conservation of energy for an arbitrary control volume is:

$$\dot{Q} - \dot{W} = (\dot{m}h_o)_{out} - (\dot{m}h_o)_{in} \quad (2.20)$$

and assuming the control volume to be adiabatic and gas to have a constant specific heat, the equation can be rewritten as:

$$-\dot{W} = (\dot{m}h_o)_{out} - (\dot{m}h_o)_{in}; h_o = c_p T_e + \frac{c^2}{2} \quad (2.21)$$

The energy equation in (2.21) is non-dimensionalized in a manner similar to the torque equation. The work output for one channel over one cycle is given by:

$$-W = \left[\frac{2\pi Rh}{N} a^{*3} \rho^* \left(\frac{L}{a^*} \right) \left(\frac{1}{\gamma - 1} \right) \int_0^{t_{cy}} \rho' U' \left(T_e' + \left(\frac{\gamma - 1}{2} \right) c'^2 \right) dt' \right] \quad (2.22)$$

The terms inside the integral can be written as the non-dimensional enthalpy flux, EF' which reduces Eq. (2.22) to :

$$-W = \frac{2\pi Rh}{N} a^{*2} \rho^* L \left(\frac{1}{\gamma - 1} \right) [EF'(Port_{out}) - EF'(Port_{in})] n_{cy} \quad (2.23)$$

The net shaft work output from conservation of energy for all the channels over one revolution is given by:

$$P_{EF} = Rh \rho^* a^{*3} \Omega' \left(\frac{1}{\gamma - 1} \right) [EF'(Port_{out}) - EF'(Port_{in})] n_{cy} \quad (2.24)$$

The computation of angular momentum and stagnation enthalpy is made in the stationary, inertial frame of reference. The stagnation temperature is T with subscript e denotes temperature in stationary frame of reference. The power calculated from Eq. (2.17) and Eq. (2.24) should match if the numerical model is formulated and implemented correctly. The sign convention in Eq. (2.24) gives positive power if work is transferred from the gas to the rotor in the stationary frame of reference. The reference power used to convert from non-dimensional form to dimensional form is $Rh \rho^* a^{*3}$ and is same in both the angular momentum formulation and conservation of energy formulation.

2.3 Verification of Numerical Model using Non-Reacting Flow Simulation

The numerical model is first verified for previously published work from NASA [29] followed by a simple three port wave rotor cycle [31]. The verification is necessary

before attempting to use the numerical model for more complex geometries and reacting flow. This section will first describe the simple case of wave rotor emptying process with one single port, followed by a full cycle simulation of the three port wave rotor cycle.

2.3.1 Single Port Wave Rotor

Model Verification

The current model was verified using the previously published data of Paxson et al. [29] who simulated the non-combusting flow in a single wave rotor channel. Three different wave rotor channel geometries were considered: (a) axially aligned; (b) - 45° stagger and uncambered and (c) symmetric arc with 30° angle at the inlet and -30° at the exit. The three geometries are shown in Figure 8. The initial state of the gas inside the wave rotor and at the ports are set to the same conditions listed in Table 2.1 for all three cases, with the gas inside the rotor set to a high pressure and at rest relative to the spinning rotor.

As the channel opens to the exhaust port, an expansion wave propagates into the rotor, discharging gas through the port. The expansion wave accelerates from the open end of the channel, reflect off the opposite end wall and reach the open end as the exhaust port is closing. The reflected wave will stop the outflow, bringing the gas back to rest. In the staggered wave rotor arrangement the axial velocity is reduced by a factor of $\cos(\zeta)$ from the unstaggered wave rotor but the flow velocity at the exhaust plane remains uniform during the entire time the port is open. This result can be explained by the fact that the blades are uncambered. Without camber there is no flow turning from inlet to exit, and thus there are no pitchwise nonuniformities and negligible local acceleration due to the expansion fan. In the wave turbine, the blades being cambered induces flow turning which causes relative unsteadiness in the flow field along the pitchwise directions which results in local acceleration. This effect can

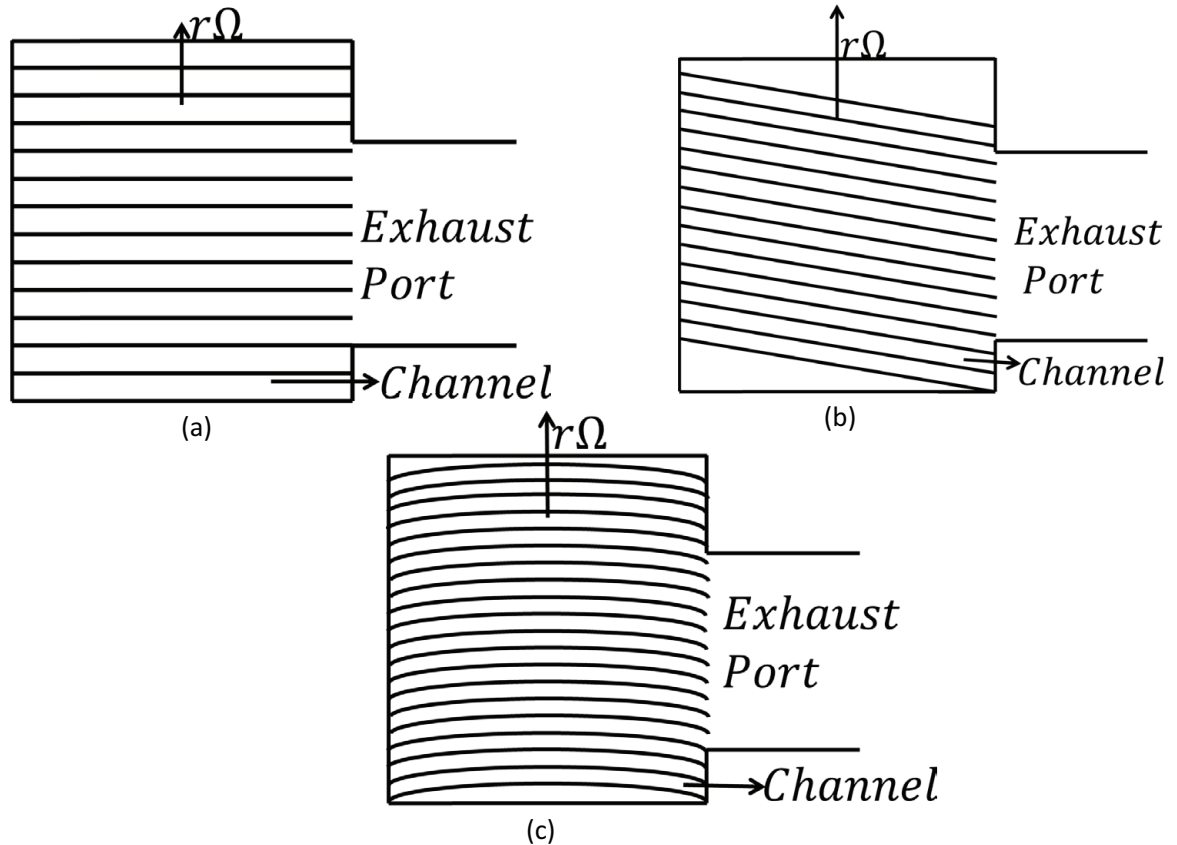


Fig. 2.8.: Wave rotor geometry for code verification. (a) Axial channels; (b) Staggered and (c) Symmetric arc [20]

be observed in the velocity profile of the jet at the channel exit in Figure 2.9(c) where the profile is no longer uniform over the time the port is open like in the staggered or axial channels. This result also implies that the source terms are indeed accounting for the blade force due to flow turning.

The axial component velocity profiles of the jet at the channel exit over the integration period for the three different test cases are plotted on Figure 2.9(a), (b) and (c). The velocity profile for the three cases are compared with the data obtained by Paxson *et.al.* [29] and match very closely. One noticeable difference is that the velocity profile in the current work turns more sharply at the end of port opening than the

Table 2.1.: Input variables for wave rotor emptying process

Parameter	Axial Channel	Staggered Channel	Curved Channel
Pressure Ratio	0.4	0.4	0.4
Passage Opening Time (radians)	0.476	0.3031	0.2244
Non-Dimensional Rotor Speed	0.15	0.467	0.467
Inlet Blade Angle (°)	0	-45	30
Exit Blade Angle (°)	0	-45	-30
Port Opening Angle (radians)	0	0	0
Port Closing Angle (radians)	2.552	3.5935	2.667
Simulation Time	2.552	3.5935	2.667

profile from Paxson *et.al.* [29]. This difference can be attributed to improvement in the resolution of numerical integration.

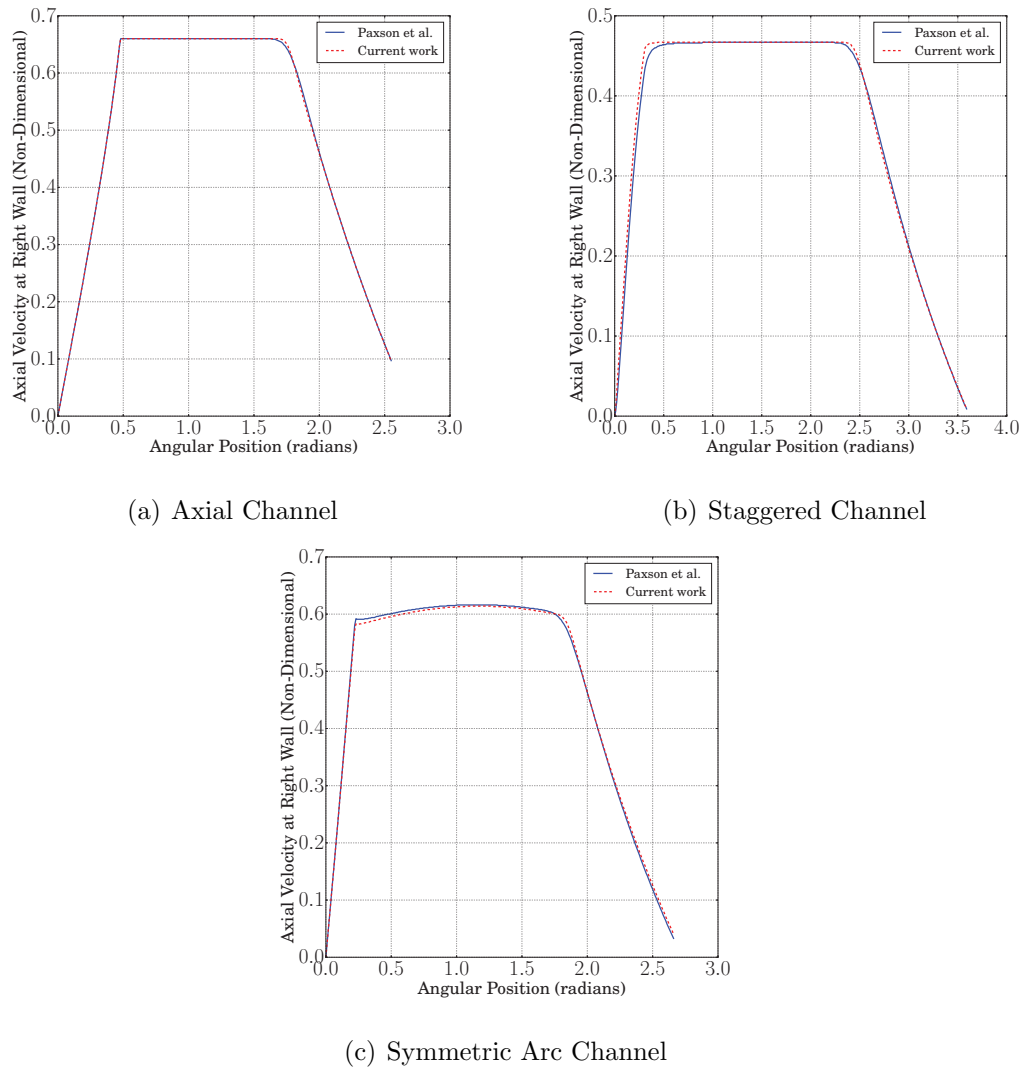


Fig. 2.9.: Axial velocity profile at the exit of wave rotor for the emptying process.

Effect of Blade Angle and Camber on the Expansion Wave

The effect of blade angles for the non-reacting expansion fan process was investigated. The resulting discharge axial velocity profiles for negative and positive stagger are shown on Figure 2.10(a) and Figure 2.10(b) respectively. For a fixed expansion

pressure ratio, the discharge velocities in the channel direction should be identical to that of the axial channel ($\beta = 0$) as shown in Figure 2.10, and remain constant until the reflected expansion wave arrives back at the port. It is verified that increasing the blade stagger angle reduces the axial velocity component of gas discharged through the exhaust port by a factor of $\cos(\beta)$. The reflected wave takes a longer time to reach the right wall due to the increase in channel length with the larger stagger angle; thus the time when the velocity starts decreasing is delayed as shown in Figure 2.10. This also suggests that a port opening period optimal for 45° stagger would be too long for a 30° stagger, resulting in back flow, emphasizing the importance of port timing in wave rotor design. It should also be noted that the axial velocity component is the same with positive or negative stagger angles as the physical process is the same in the channel lengthwise direction.

A parametric study on the effect of camber was first performed on a symmetric channel with increasing camber of parabolic curvature. Increasing camber tends to reduce the gas discharge velocity similar to the staggered case; however the local acceleration due to flow turning provides convexity to the shape of the velocity profile as observed in Figure 2.11. The convexity can be explained from the momentum equation source term, which involves an axial variation of the blade angle ζ and pressure. The blade force in a staggered case is only due to spatial variation of pressure, while for the cambered blade there is an additional force due to spatial variation of ζ which is responsible for local acceleration or deceleration and the convexity in velocity profile. The parametric study demonstrates that the code is indeed performing as expected and further study can be done with full cycle computations. Later, additional cases are presented with parabolically curved channel where the left side of the channel is set to 0° and the right side blade angle is varied.

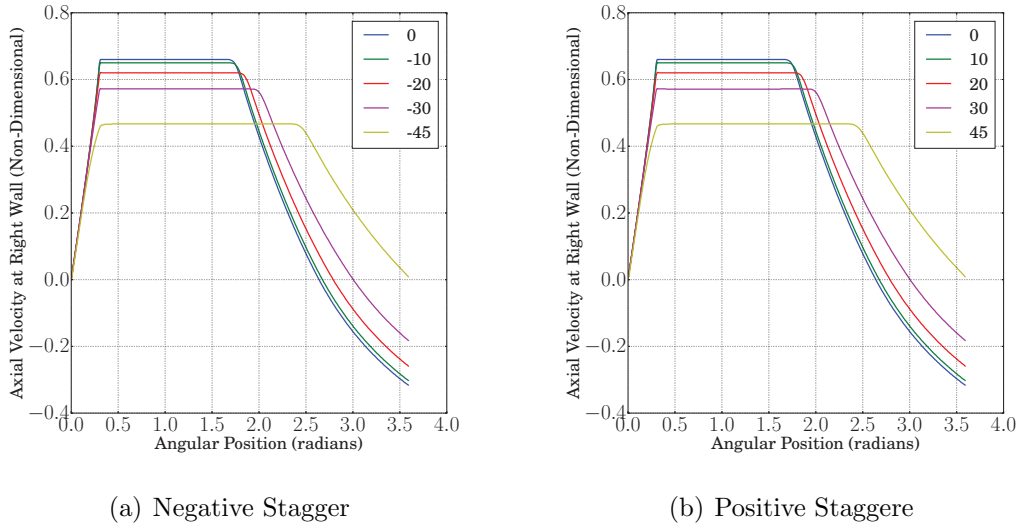


Fig. 2.10.: Variation of exit velocity profile with blade stagger angle

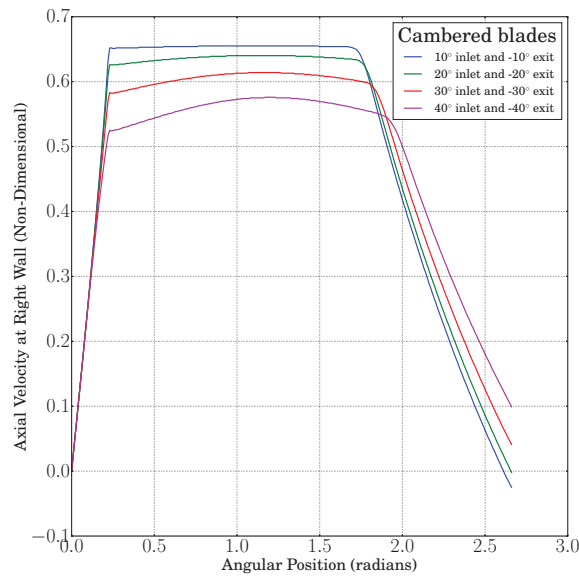


Fig. 2.11.: Variation of exit velocity profile due to change in blade camber

2.3.2 Three Port Wave Rotor

A three-port divider cycle wave rotor, a simple cycle that combines both compression and expansion and that has been studied extensively in prior work [15]. The model input parameters such as the pressure ratios, port opening and closing

time and rotor speed were kept constant for all simulation and are given in Table 2.2. All loss mechanisms were neglected except the flow incidence loss, in order to isolate the contributions of the blade forces to the overall work transfer. First, a three-port cycle with axial channels was simulated, and brief grid independence study was conducted. The flow incidence angle, and hence the incidence loss and torque, was then minimized in the axial configuration by changing the inlet duct angle. The optimal duct angle found in the axial case was then translated to the case with curved blades and the shaft power was estimated. The wave processes are also briefly described and analyzed in both the axial and non-axial channel cases. Achieving a repeating identical limit cycle solution is based on net zero mass accumulation over a cycle with no further change in the mass fluxes of ports. It is observed that constant port fluxes of mass usually ensures that fluxes of any other quantity like enthalpy and momentum becomes a constant over one cycle and the time-history of the cycle repeats exactly, making it periodic. A mass flux difference of 0.01% between inflow and outflow is used to check for a repeating cycle.

Table 2.2.: Three-Port Divider Cycle Parameters

Parameter	Value (Non-Dimensional)
High Pressure Ratio	1.8
Low Pressure Ratio	1.8
Channel Opening Time	0
Inlet Blade Angle ($^{\circ}$)	0
Exit Blade Angle ($^{\circ}$)	0
Inlet Port Opening Time	1.89
Inlet Port Closing Time	2.83
High Pressure Port Opening Time	2.38
High Pressure Port Closing Time	3.11
Low Pressure Port Opening Time	0
Low Pressure Port Closing Time	0.9
Rotor Speed	0.5
Radius	1

Effect of Computational Grid Size

To study the effect of grid density on the wave rotor gas dynamics, calculations were performed using both a low grid density (200 computational cells) and a high grid density (800 computational cells). The time steps for both cases were chosen to maintain a Courant number of 0.2. The mean channel pressure was calculated at every time step and is plotted for both grids in Figure 2.12. The difference in mean pressure for 200 and 800 computational cells is less than 1% indicating that the solution is highly grid independent. Further, the pressure at the middle of the channel is plotted in Figure 2.13 for both 200 and 800 computational cells. The mid-channel pressure for both grid densities are within 1%, indicating that 200 computational cells

are sufficient for the current work. Based on this brief grid study, 200 computational cells were used for the studies described in this section, with a non-dimensional computational cell size of 0.005 and a non-dimensional time step of 0.001, corresponding to a nominal Courant number of 0.2. In the case of non-reacting flow, only the contact interface needs to be resolved which can be done with 200 cells, but for wave rotors with reacting flow a higher grid density may be required to predict the speed and thickness of the flame front. It is noted that with shock-capturing numerical methods such as Roes method, the accurate prediction of shock and pressure wave speeds has been accomplished with relatively coarse grids. As the wave rotor rotates and the channel aligns itself with the ports, pressure waves are generated through instantaneous opening and closing of the ports. Choosing an appropriate computational time step is critical to accurately capture the waves. If the time step is too large then the waves are not captured accurately, but a time step that is too small will require unnecessarily high computational resources. In the current work, the time step used for the full cycle simulation of the wave rotor is 0.001 to maintain a nominal Courant number of 0.2, as stated above. To verify that this time step is sufficiently small to capture the waves, two simulations with shorter time steps were conducted with the same computational cell size of 0.005. The velocities at the inlet and outlet are plotted in Figure 2.14 and Figure 2.15, respectively, for three time steps: 0.0001, 0.0005 and 0.001. As expected, as the time step is decreased the temporal rise in pressure and velocity across any shock is sharper. However, as the time step is increased, the timing of travel is not noticeably changed. The code captures shocks and predicts wave speeds consistently; for example, even the sharp expansion wave at the inlet end around 162° is essentially unchanged. Therefore, a time step of 0.001 is sufficient for the present simulations.

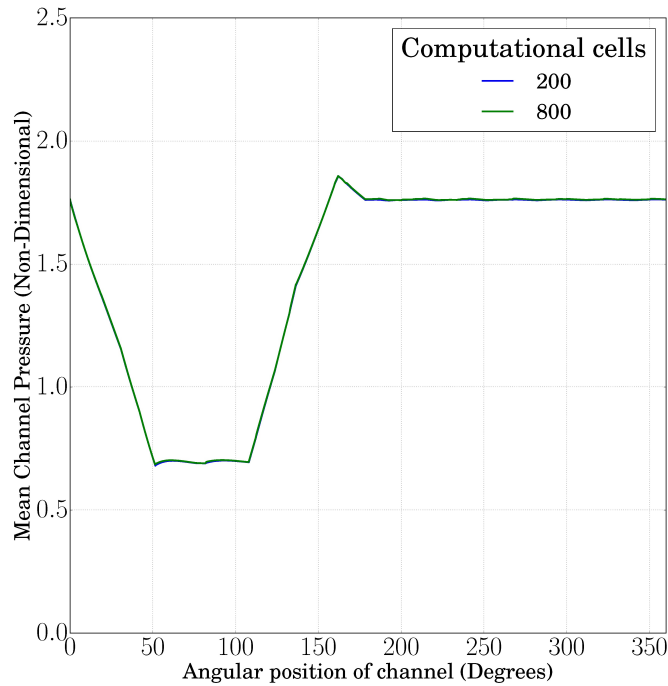


Fig. 2.12.: Mean channel pressure as a function of angular position of channel for different grid densities

Three-Port Axial Channel Wave Rotor

The inlet duct needs to be designed to produce minimum possible incidence loss. In the simulation, the duct angle is an input parameter and can be varied to obtain the minimum incidence using a manual trial-and-error process. For an axial channel wave rotor, the only source of torque is through inflow incidence, as the outflow is axial and creates no torque, and therefore a duct angle designed to produce net zero incidence torque can be considered as the definition of the minimum incidence duct angle. The minimum incidence duct angle calculated for an axial channel serves as a starting point for minimizing incidence loss for the non-axial channel wave turbine.

To simulate an axial channel wave rotor using the wave turbine model, the blade angle was set to zero at both the inlet and outlet. The inlet duct angle was initialized

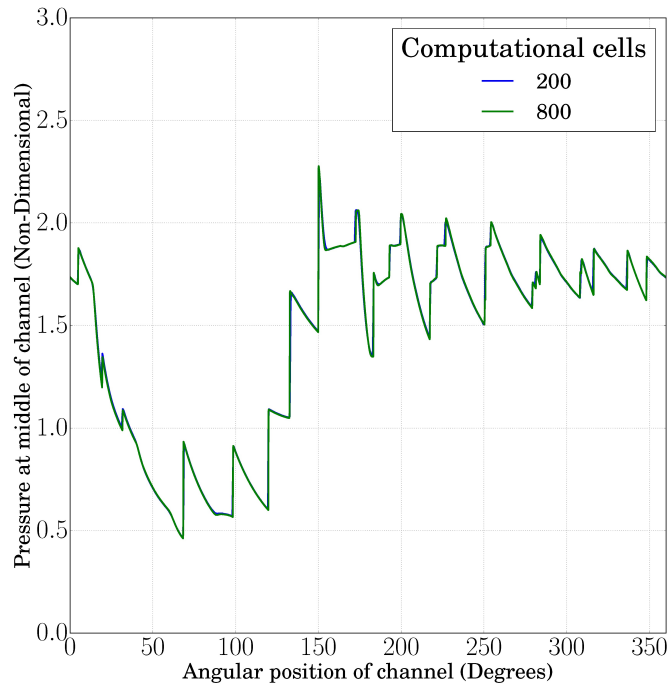


Fig. 2.13.: Pressure at middle of the channel as a function of angular position of channel at different grid densities

at 0° and then increased in increments of 5° until the relative frame inflow angle i with respect to the channel reduced to zero, indicating minimum incidence loss. The shaft work associated with flow incidence in each channel is calculated as a function of its angular position over one cycle using both methods described in Section 1.2.3, and then integrated to get the overall torque and shaft power due to incidence mismatch for one cycle of rotation of the wave rotor. The shaft power is negative for small duct angles, indicating work being done on the gas by the rotor due to incidence. The shaft power becomes less negative as the duct angle is increased and reaches zero for a particular duct angle, indicating that there is minimum incidence loss on average for the entire cycle. Further increasing the duct angle will result in positive shaft power where work is transferred from the gas to the rotor.

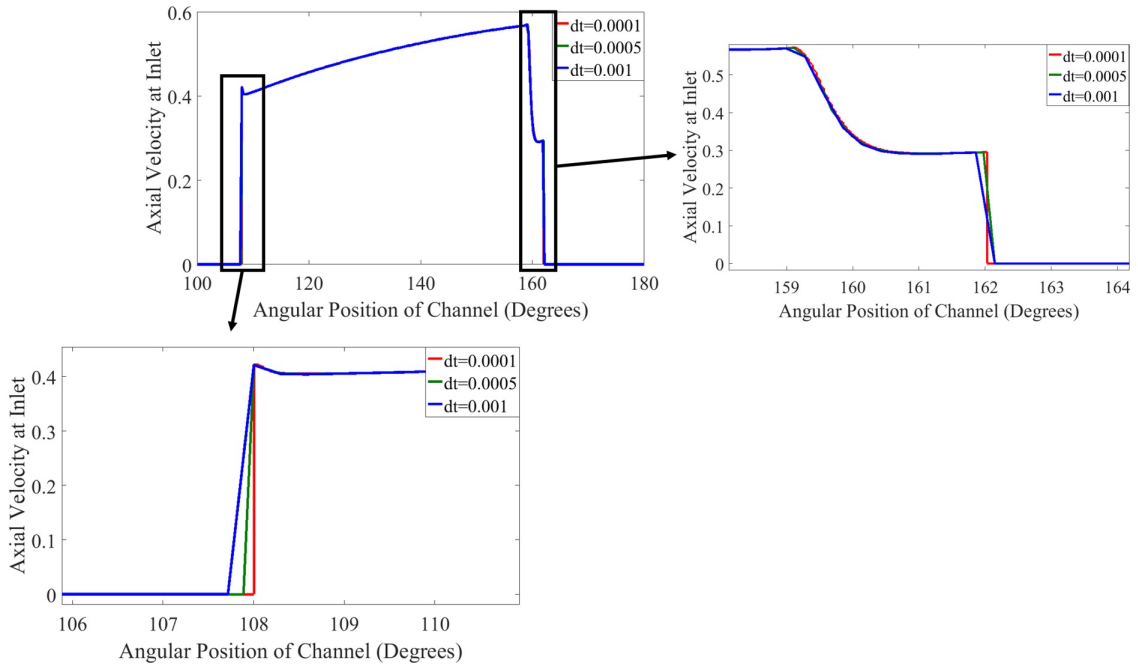


Fig. 2.14.: Velocity at inlet for three computational time steps. Zoomed-in view shows the shock wave timing at 108° and expansion wave profile at $159\text{--}162^\circ$

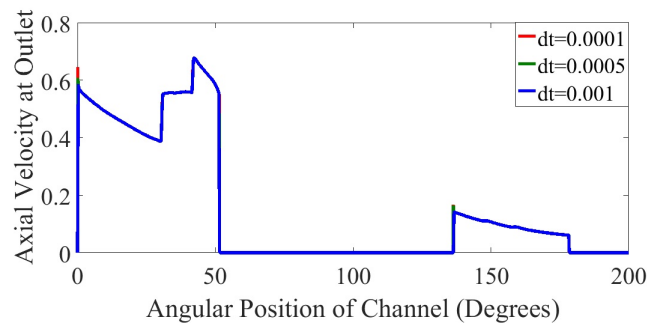


Fig. 2.15.: Velocity at the outlet for three computational time steps.

In the present case, the duct angle where the shaft power reduces to zero for the boundary conditions specified in Table 2.2 was found to be 38.1° as shown on Figure 2.16. The relative frame inflow angle, i , is also calculated from Eq. (16) as a function of angular position of the channel from inlet opening angle to inlet closing

angle and is plotted in Figure 2.17 for every 10° change in duct angle. For a duct angle of 38.1° , the relative frame inflow angle is negative for the first half of the port open time and positive for the remaining half, providing 0° incidence on average at the design-point operating condition. This optimal duct angle is dependent on the operating conditions of the wave rotor, and thus a fixed duct angle will be optimal only at its design-point condition. A more sophisticated inlet system could include variable-angle inlet guide vanes and a control system to vary the duct angle based on the particular operating conditions. To illustrate the predicted flow over one cycle

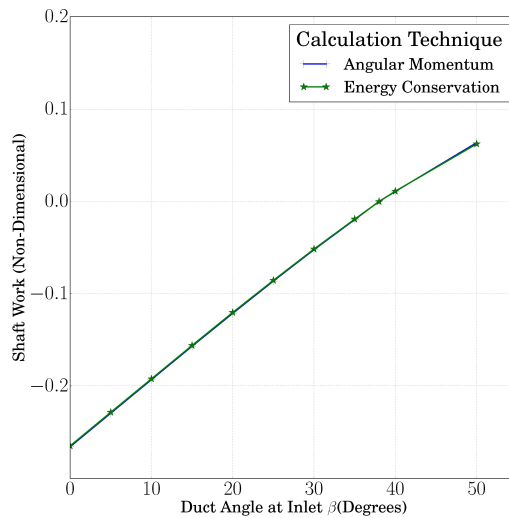


Fig. 2.16.: Shaft power due to incidence mismatch for an axial channel

of operation, an x-t diagram of temperature and pressure within the channel and an axial velocity plot at the inlet and exit plane are shown in Figure 14. The non-dimensional axial velocity is indicated by a red dashed line for the right-side (outlet) ports and with a solid blue line for the left side (inlet) port. The low-pressure outflow port opens at 0° at the right end wall, initiating an expansion wave to accelerate and vent gas out through the port. The port then closes at 51.5° generating a compression wave. The intermediate pressure inlet port opens at 108° and closes at 162° on the left end wall, where the propagation of shock wave pulls fresh gas into the rotor. The

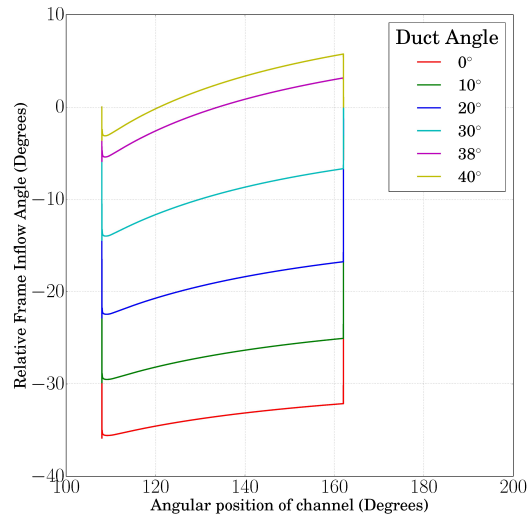


Fig. 2.17.: Relative frame inflow angle as a function of angular position of the channel for an axial-channel three-port wave rotor

shock wave increases the pressure of the gas in the channel as it is pushed through the high-pressure port between 136.36° and 178.42° at the right end wall. At the close of the high-pressure port another shock wave is generated which undergoes multiple reflections at both left and right end walls. The shock and its multiple reflections increases the pressure as the channel aligns itself with the low pressure exhaust port. These gas dynamics throughout one cycle (from 0 to 360°) can be observed in the contour plot of temperature and pressure in Figure 14.

Three-Port Wave Turbine

In a wave rotor with non-axial blades, the shaft power or work rate transfer between the gas and the wave rotor has two components: work transfer from flow turning due to inlet incidence and work transfer due to angular momentum change through the length of the wave rotor channel. In an axial channel with no net flow turning, the only contributing component is from inlet incidence. As shown in the

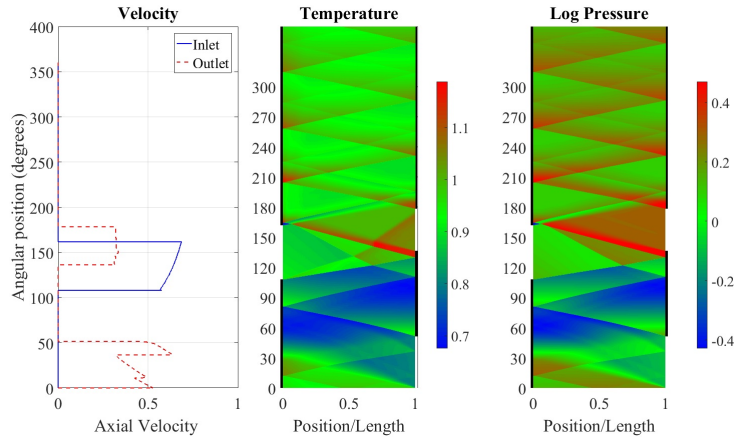


Fig. 2.18.: Axial velocity, temperature and the logarithm of pressure for an axial-channel three-port wave rotor with optimal duct angle

previous section, designing the inlet duct at an optimal angle can minimize inlet incidence and work transfer. For the case considered here (three-port cycle with operating conditions given in Table 2.2), the work rate of the axial-channel wave rotor reduces to zero at an inlet duct angle of 38.1° . A similar procedure must be followed for the non-axial channel case to find the duct angle that produces minimum incidence, i.e. the net torque due to incidence is zero. Using this optimum duct angle, the overall shaft work calculated will be due only to the flow turning along the length of the curved channel.

Consider a wave turbine where the channels follow a parabolic blade profile with a left-end blade angle of ζ_l and a right-end blade angle of ζ_r , as illustrated in Figure 2.4. The values of ζ_r and ζ_l then uniquely determine the blade shape. Both values set to zero degrees will produce an axial channel. In the current work, one specific blade shape used is parabolic and symmetric and so the exit and inlet angles are equal with opposite sign, although the model can handle any complex blade shape. The optimal inlet duct angle calculated for the axial channel is used as an initial guess for the optimal duct angle for the non-axial (parabolic) channel. The duct angle is changed in small increments or decrements depending on a positive or negative

inlet blade angle until the relative-frame inflow angle i matches the left-end blade angle ζ_l on average over the inlet port open time. The duct angles that minimize incidence for different inlet blade angles, ζ_l , for the particular pressure boundary condition in Table 2.2 were estimated and shown in Table 2.3. The relative frame inflow angle i with respect to channel direction and as a function of angular position of the channel for a $+30^\circ$ at the left to -30° at the right symmetric blade angle case is shown in Figure 2.19. Similar to the relative frame inflow angle for the axial channel case (Figure 2.17), the curved channel case also has a angle for the earlier part of the inlet port open time and positive angle for the later part, giving an average incidence of -0.12° over the entire inlet port open time. The incidence angle at the port opening and closing boundaries is often sharply different velocity direction.

Table 2.3.: Three-Port Divider Cycle Parameters

Inlet End Blade Angle ($^\circ$)	Duct Angle ($^\circ$)
0	38.1
5	43.1
10	46.4
15	48.7
20	51.6
25	55.4
30	58.4

An $x - t$ plot of temperature, pressure and axial component of velocity for a symmetric $+30^\circ$ to -30° parabolic channel is shown in Figure 2.20. The port timing is identical to the timing in the axial channel case and the gas dynamics in terms of compression and expansion waves are similar to the axial channel. However, one noticeable difference is that the axial velocity component is lower for the non-axial channel compared to the axial channel. In the curved channel case, the tangential component of velocity contributes towards work transfer, which effectively causes a reduction in kinetic energy in the flow in the stationary frame-of-reference as it passes

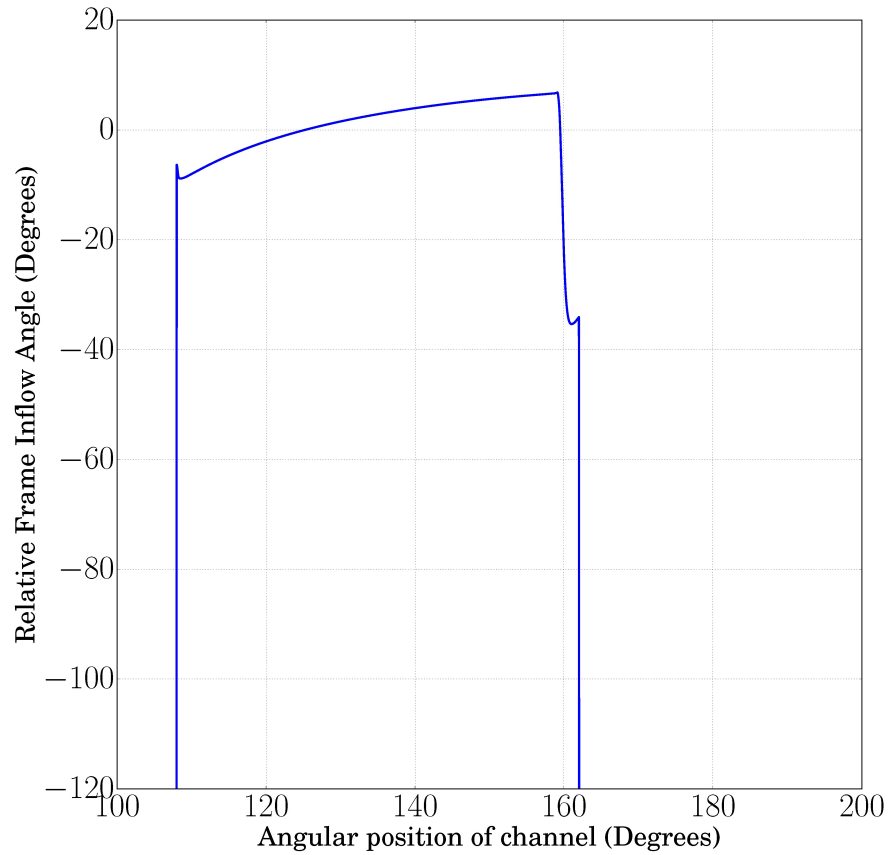


Fig. 2.19.: Relative frame inflow angle with respect to channel inlet angle for $+30^\circ$ to -30° symmetric blade wave turbine

through the channels. In addition, the curvature of the blade increases the length of the channel and therefore the waves takes longer to travel the entire length of the channel.

The duct angle that minimizes incidence loss is calculated for the different blade angles using the methodology mentioned above. With the optimal duct angles listed in Table 2.3, pressure boundary condition in Table 2.2 and the corresponding blade angles, the effect of flow turning on shaft work is now analyzed. Since the blades are symmetric, as the inlet blade angle is varied from 0° to 30° an overall flow turning

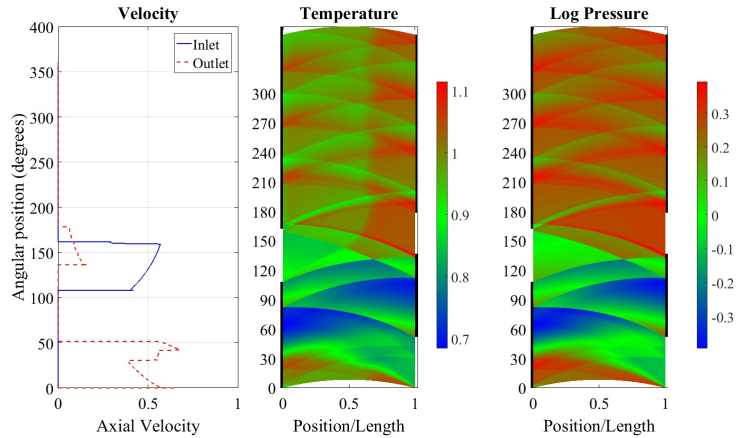


Fig. 2.20.: Axial velocity, Temperature and Log of Pressure (all non-dimensional) for three-port wave turbine with $+30^\circ$ to -30° symmetric parabolic blade and optimal duct angle

angle of 0° to 60° is obtained. The overall shaft power is estimated using the methods described in Section 1.2.3 for each of the blade angles and a plot of shaft power vs. blade angle is shown in Figure 2.21. The non-dimensional shaft work increases from 0 for the axial channel wave rotor to 0.16 for the 30° symmetric channel wave rotor. The positive sign indicates that work is being done by the gas on the rotor and the shaft power increases with blade angle due to the increase in flow turning and angular momentum change from the inlet to the exit of the channel.

According to Eq. 2.17 and 2.24, the shaft power is normalized using $Rh\rho^*a^{*3}$. An experimental axial channel wave rotor [9] is used to obtain these reference conditions, with the expectation that this rig could be redesigned to accommodate a wave rotor with curved channels. In the experimental design, the mean radius R is 0.19 m, the passage height is 0.07 m, the reference speed of sound is $a^*=338.40$ m/s and the reference density is $\rho=1.22$ kg/m³. Using the reference values, the dimensional shaft work for the 30° symmetric blade angle is found to be 100 kW or 135 hp. If we assume a turbomachine that expands flow from high pressure to low pressure, such that the pressure ratio is equal to the ratio between inlet port and low pressure port of the

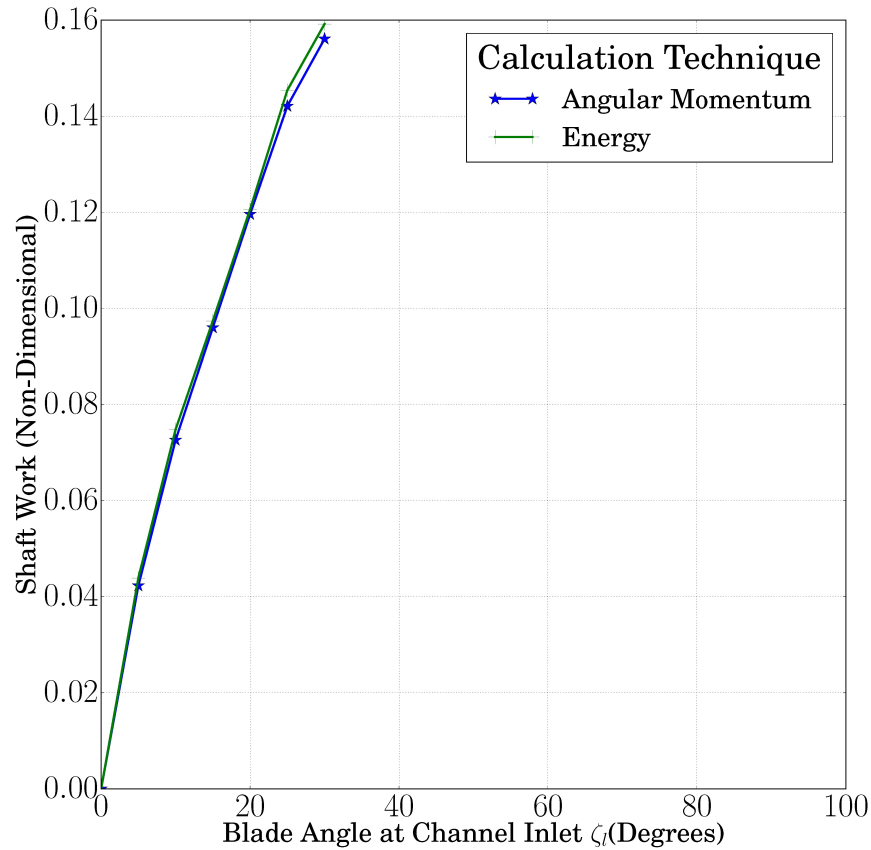


Fig. 2.21.: Shaft power due to flow turning in a wave turbine with symmetric blades

three-port wave rotor and works with the same mass flow rate then the turbomachine provides 210 kW. If we compare the wave rotor work with the turbomachine work, then the three-port wave turbine is capable of providing 52% of the turbomachine work. It should be noted that this power is calculated while neglecting heat transfer, frictional losses, leakage effects, finite port opening time and windage losses. Including these effects could lower the shaft work produced by flow turning inside the wave rotor. On the other hand, the port timings that were optimized for an axial channel may be suboptimal for the curved channel, and more optimal timing may improve the work output. These effects will be studied in future work.

The extended model was then used to simulate a single port wave rotor and three-port divider wave rotor cycle with both axial and curved channels. Simulating the two simple cases provided validation for the numerical model. The resulting transient flow field and wave patterns were analyzed using $x - t$ diagrams of temperature and pressure as well as plots of the flow velocity at the inlet and exit planes. The flow incidence torque was minimized by varying the inlet duct angle and the shaft power for the rotor was estimated for different blade angles. The shaft power was shown to increase with blade angle due to increase in flow turning and hence change in angular momentum. An initial estimate of dimensional shaft work for an experimental wave rotor with effective camber of 60° is predicted to be about 100 kW in the ideal scenario where all loss generating mechanisms such as heat transfer, friction, leakage and windage are absent.

2.4 Application of Numerical Model for Wave Rotor Combustion Turbine

The main motivation to develop the numerical model is to design a wave rotor with non-axial channels and internal combustion. A schematic for a wave rotor with internal combustion is shown below in Figure 2.22. A wave rotor with internal combustion typically has one air-fuel inlet port and one rotor end and one exhaust port at the other rotor end. The reactants mixture enters through the inlet port. The burnt gases are then purged through the exhaust port. A small orifice (on the exhaust side in the current design) supplies a high-speed jet of hot gas to ignite the mixture. This orifice is treated as an additional port of narrow width in the numerical model. The timing of the opening and closing of these ports is critical for optimizing performance of the wave rotor.

2.4.1 Axial Channel Wave Rotor Combustor With Correct Port Timing

The inlet port opening, exhaust port closing and inlet port closing are considered to be the most important parameters. The design starts with the exhaust port which

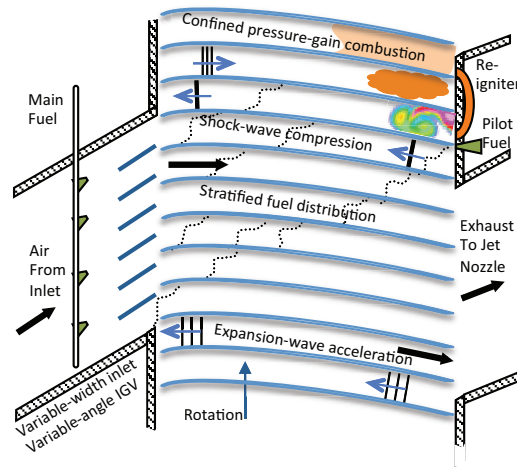


Fig. 2.22.: Internal gas dynamics of wave rotor with internal combustion

is set to open at time $t = 0$ sending an expansion wave towards the inlet port which decreases the rotor pressure. The pressure trace on the inlet side is tracked as shown in Figure 2.23 and the inlet port is set to open when this pressure is equal to the inlet stagnation pressure. In this case the inlet stagnation pressure at the port was set equal to 1.22, so the inlet port should open at 48° .

The inlet port opening generates a shock wave which draws fresh reactant mixture into the rotor towards the exhaust port. The exhaust port is designed to close on the arrival of fuel at the exhaust side, approximately at 135° as shown in Figure 2.24.

The closing of the exhaust port produces a hammer shock that propagates towards the inlet port. The inlet port is designed to close on the arrival of hammer shock at the inlet port. This timing can be determined by tracking velocity at the inlet and closing the port when velocity drops to zero which in this case is 166° as shown in Figure 2.25. This timing scheme ensures that there will be minimal leakage.

The duct angle that minimizes incidence loss will be estimated from the filling process and the incidence angle as a function of angular position of the channel during the time the inlet port is open is shown in Figure 2.26. It can be observed from the plot that the incidence angle changes as a function of angular position of

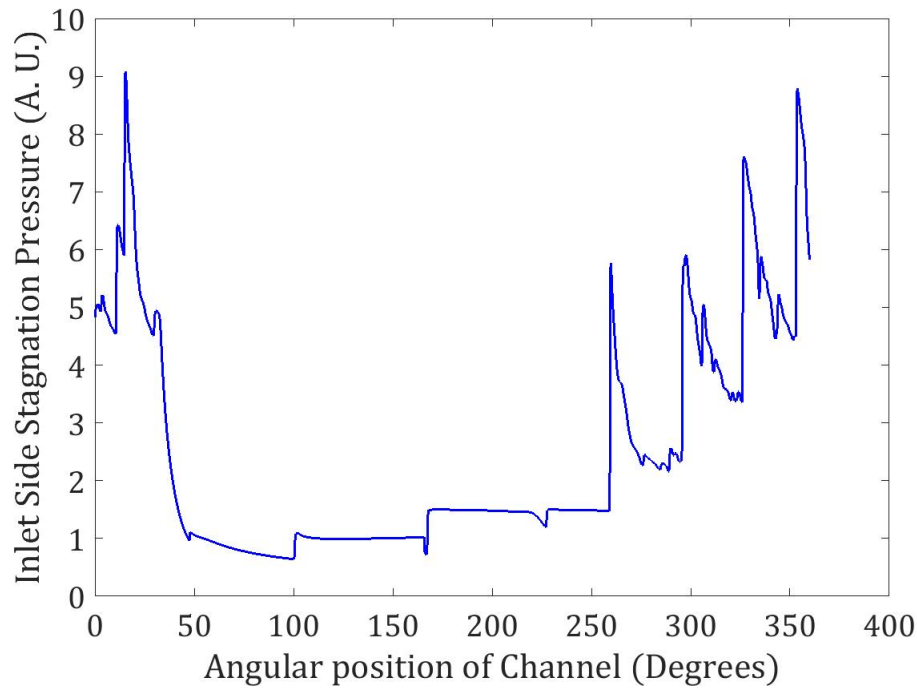


Fig. 2.23.: Inlet side stagnation pressure as a function of angular position of channel

channel due to pressure waves at the inlet. However, on average over the inlet port opening time, the net incidence is only 3° .

The wave processes described above are illustrated in the reacting wave rotor schematic shown in Figure 2.22. The internal gas dynamics of the full cycle simulation is shown below in 2.27. The pressure waves can be visualized from the contour plots of pressure. There is an expansion wave that propagates from the exhaust as it opens, then we have shock wave that propagates from inlet to exhaust as the inlet port opens and finally we have a hammer shock as the exhaust port closes. Ignition of the reactant mixture increases the pressure, which can be observed from about 240° . Due to combustion there should be a temperature rise corresponding to a pressure rise, which can be clearly seen in the temperature contour plot. The contour plot for mixture fraction of fuel, intermediate and oxidant is shown in Figure 2.24. From the fuel fraction contour plot, it can be observed that all the fuel is getting trapped

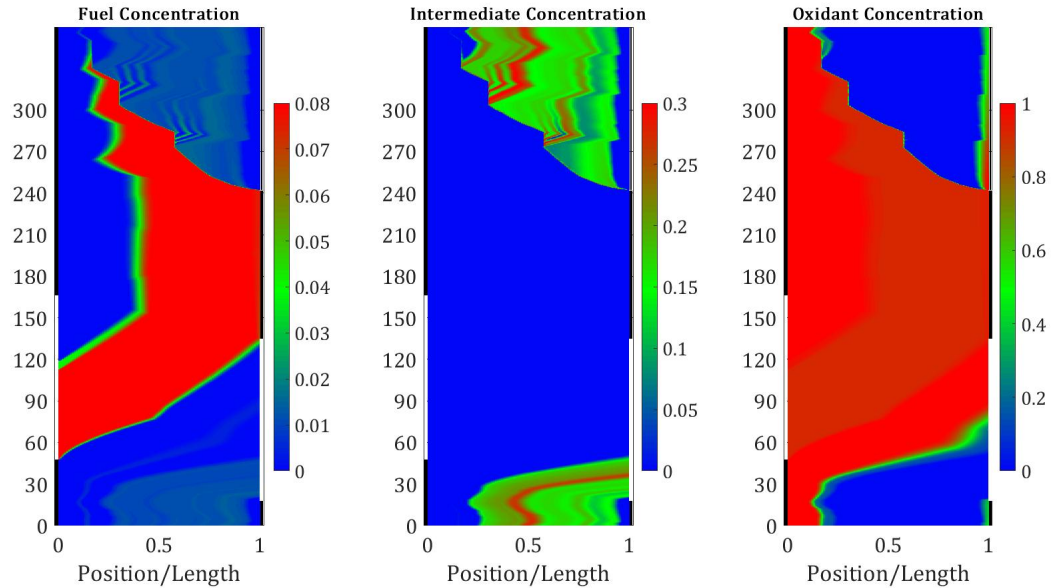


Fig. 2.24.: Contour plot of mixture fraction of fuel, intermediate and oxidizer species

inside the rotor with minimum spillage, followed by combustion at the ignition port location. The intermediate and oxidizer contour plot shows that all oxidizer is used up to burn the fuel through a two step reaction. This provides a baseline simulation for axial channel wave rotors with internal combustion. The inlet duct is also optimized to minimize incidence loss at the inlet.

With this baseline port timing, the channel curvature can be varied. Although the numerical model can be used for any blade curvature, the current work will only focus on axial flow at the inlet and non-axial flow at the outlet. This would mean the blade angle would be 0° at the inlet and an arbitrary angle at the outlet. This will also help in maintaining the same duct angle for all the subsequent numerical simulations since the inlet side blade angle is axial always. The addition of blade curvature slows down the pressure waves and therefore the port timing may no longer be optimal and a non-optimal port timing may lead to failed ignition. Therefore the port timing needs to be re-optimized for any change in blade curvature.

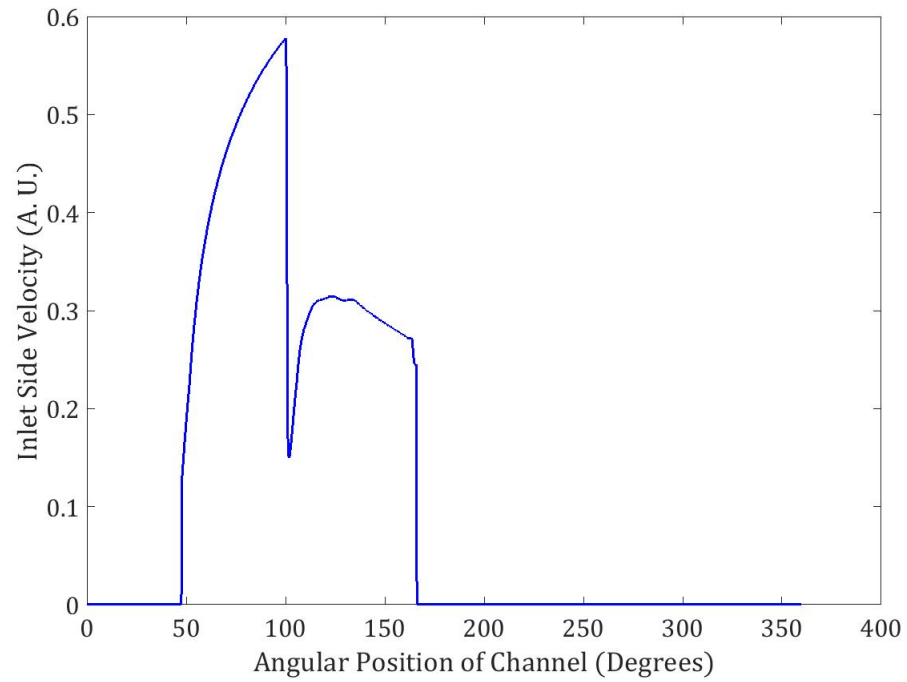


Fig. 2.25.: Inlet side velocity as a function of angular position of channel

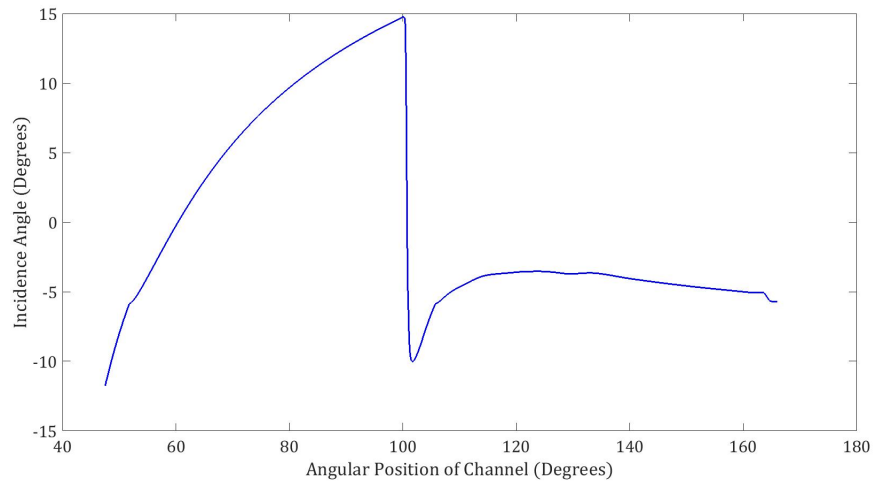


Fig. 2.26.: Inlet incidence angle as a function of angular position of channel

2.4.2 Non-Axial Channel Wave Turbine Combustion

The baseline simulation of an axial channel wave turbine with optimal port timing and inlet duct was performed in the previous section. Now the blade angle at the

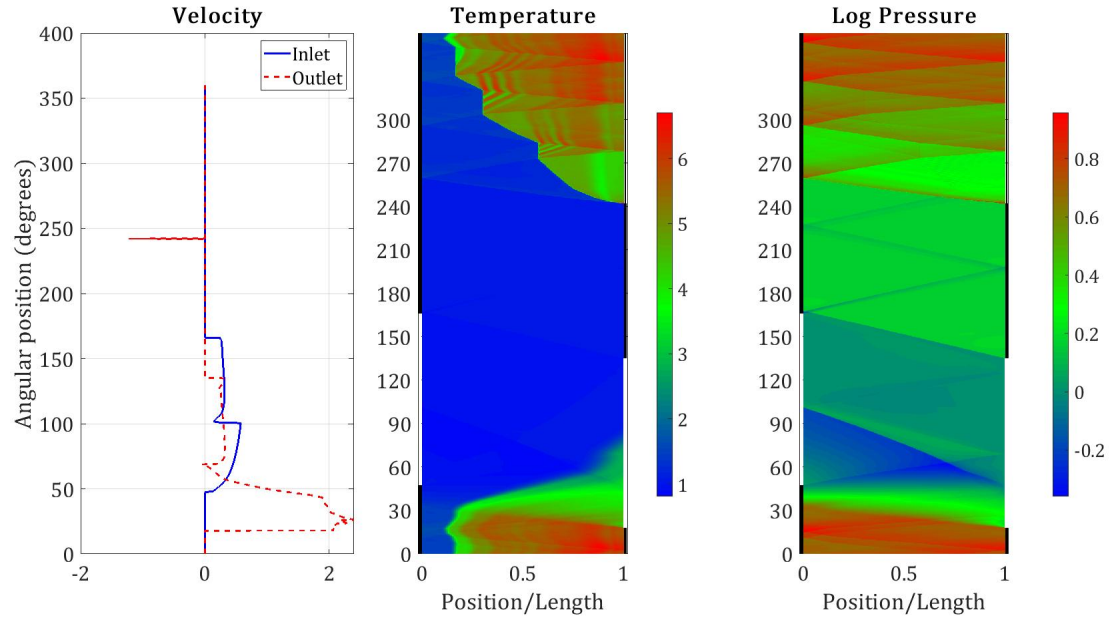


Fig. 2.27.: Velocity, Temperature and Pressure for full cycle axial channel wave rotor with internal combustion

exhaust end of the channel is varied from 5° to 30° and the angle at the inlet end of the channel is maintained at 0° . This ensures that the inlet duct used for the axial channel can still be used for non-axial channel simulation. The change in blade curvature adds additional path length for both the shock and expansion waves. Due to the additional path length, the waves take longer to arrive at either end and causes the ports to be mistimed. The mismatch between arrival of waves and opening and closing of the ports causes the reacting mixture to arrive at the right hand side wall at a different time which leads to a misfire. The slowing down of waves can be observed in the inlet velocity for the different blade angles as shown in Figure 2.28. It can be observed that as the inlet port opens at 45° , the velocity begins to rise and have a peak due to the shock wave generated at the inlet opening. The rise of velocity is slower and the peak value reduces as the blade curvature is increased. The peak value reduces by roughly the cosine of the blade angle. The fluid flow at the inlet is stopped

by the arrival of the hammer shock generated at the closing of exhaust port. Since the path length is increased due to introduction of blade curvature, the hammer shock takes longer to travel from exhaust to inlet, therefore the axial velocity at inlet goes back to zero at a later time for increase in blade curvature. Since the inlet velocity goes back to zero at a later time, the inlet port also should be closed at a later time. The exhaust port closing is also slightly delayed because the fuel air mixture at the inlet is coming in slower and will arrive at the exhaust end slightly later in time. The port timing is adjusted for the different blade curvatures and simulation is performed until a limit cycle is obtained for the different cases. The pressure at the inlet and exhaust port is maintained same as the axial channel wave rotor simulation. The change in port timing for the different blade angles is indicated in table 2.4. It can be observed that the inlet port closing location changes from 166° for axial channel to 198° in the case of 30° blade angle. The closing of exhaust port is also delayed due to blade curvature and the closing location changes from 135° for axial channel to 198° for blade angle of 30° . As the blade angle is increased, it gets harder to burn the mixture of fuel and air. For a blade angle of 30° , with the same pressure boundary condition, the change in inlet and exhaust port closing location was nearly 25° . Even the inlet duct angle changed by 10° in order to minimize incidence loss at the inlet.

Table 2.4.: Opening and closing locations of the ports and the inlet duct angle for different blade geometries

Blade Exit Angle	Duct Angle	Inlet Port Open	Inlet Port Close	Exhaust Port Open	Exhaust Port Close	Ignition Port Open	Ignition Port Close
0	52.71	47.55	166	18	134.94	241.95	242.36
-5	52.71	47.55	167.3	18	135.1	241.95	242.36
-10	52.71	47.55	168.45	18	135.67	241.95	242.36
-15	52.71	47.55	169.6	18	136.82	241.95	242.36
-20	52.71	48.7	171.77	18	138.37	241.95	242.36
-25	52.71	48.7	174.18	18	140.15	241.95	242.36
-30	62.45	51	198	18	165	242.52	242.93

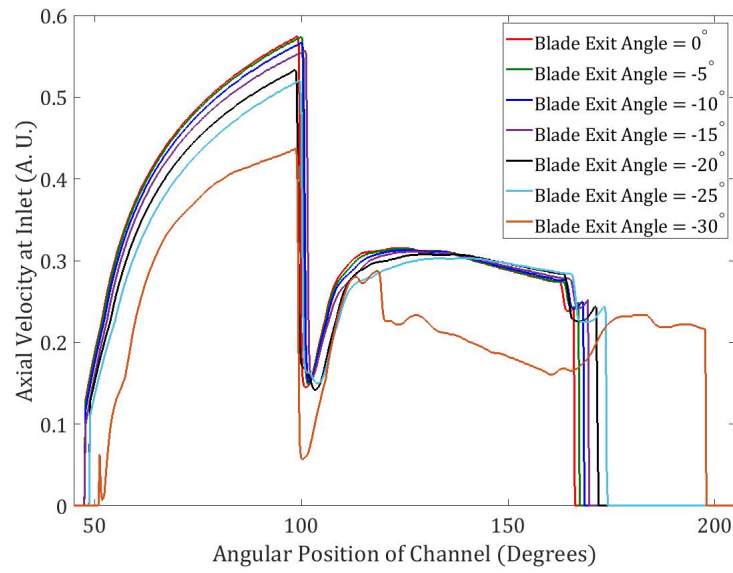


Fig. 2.28.: Axial velocity at the inlet for different blade profiles

The port timing is adjusted for the different blade angles and simulation is performed. The internal gas dynamics can be understood through a contour plot of pressure, temperature and species fraction. The gas dynamics is similar to axial channel wave rotor, the exhaust port opens to generate an expansion wave that accelerates towards inlet port and lowering the pressure. Once the pressure reaches inlet boundary condition, the port is opened, generating a shock wave that increases pressure in the rotor and pulls fluid into the rotor. The reacting mixture from the inlet moves towards the right side wall and the moment it reaches the right wall, the exhaust port is closed, generating a hammer shock that moves towards the inlet port. The hammer shock stops the fluid entering from the inlet port. The inlet port is closed when the hammer shock arrives at the inlet port.

The contour plot for both the axial and non-axial channel look very similar, but the difference between the two can be clearly seen by plotting pressure at inlet, mid-channel and exit plane of the rotor. As mentioned earlier, the blade curvature increases the path length and the waves take longer to arrive at either end of the wave rotor. The pressure at inlet plane, mid-channel and exit plane of the wave rotor

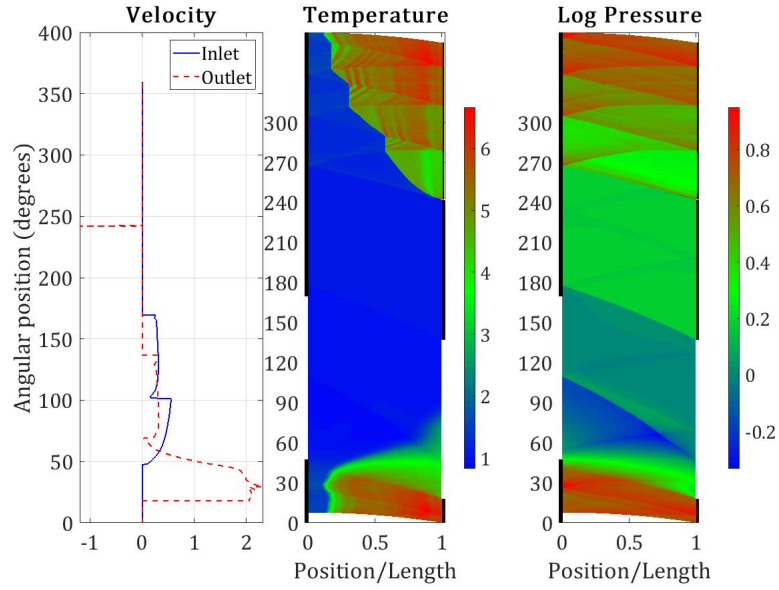


Fig. 2.29.: Velocity, Temperature and Pressure contour plots for wave turbine combustion simulation with blade angle of negative 15°

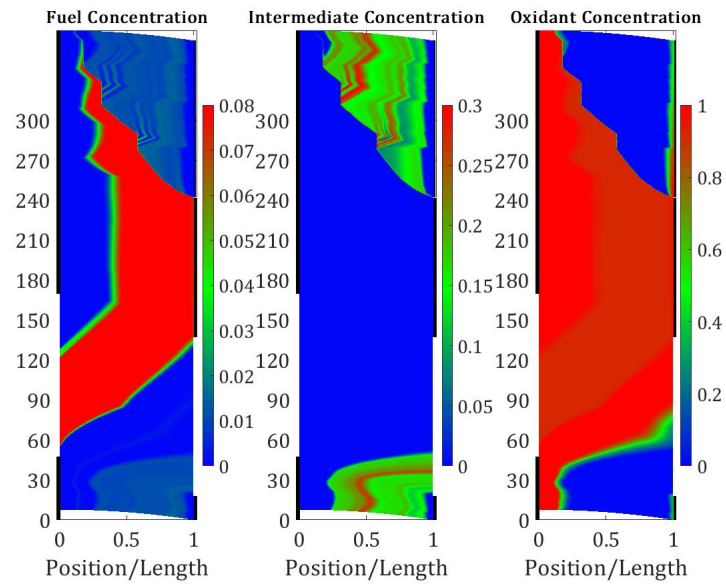


Fig. 2.30.: Species fraction for wave turbine combustion simulation with blade angle of negative 15°

is plotted in Figure 2.31 for a 15° blade and in Figure 2.32 for a 30° blade. It can be observed that for the 15° blade, the pressure shown in red is slightly behind the blue line which indicates the waves are taking longer to travel. In the case of 30° blade, the pressure in red is much lower than axial channel and also the hammer shock takes longer which is indicated by the pressure jump beyond 100° . It goes to show that increasing blade curvature may lead to higher angular momentum change but the probability to achieve combustion reduces. The same is also confirmed in the velocity plot on Figure 2.28.

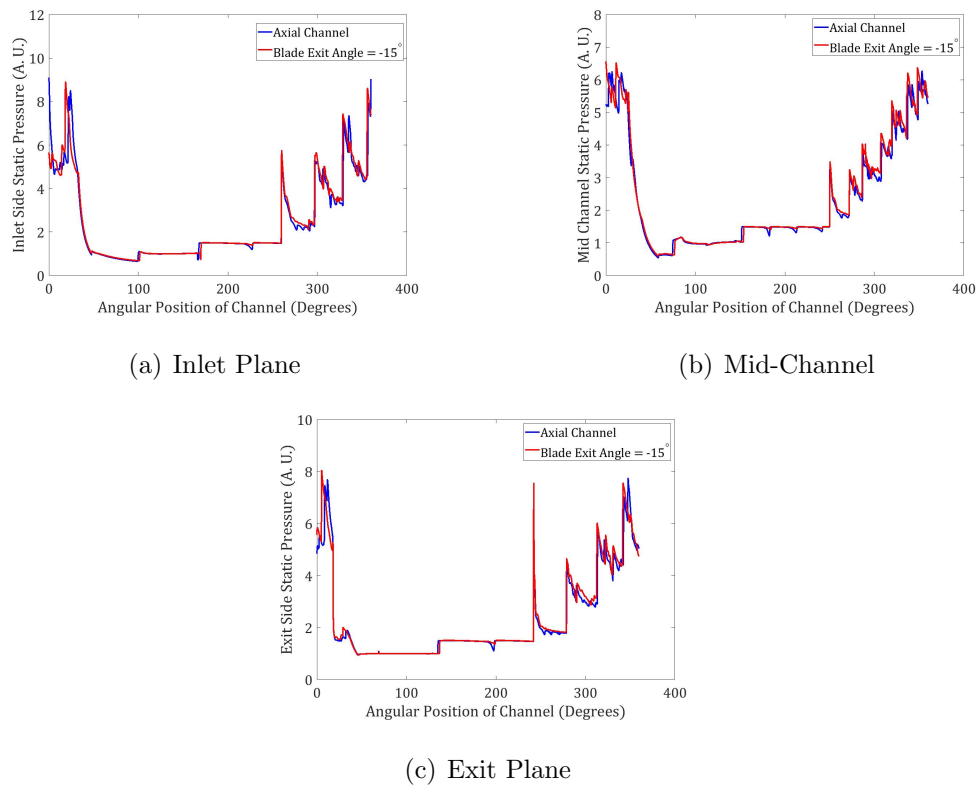


Fig. 2.31.: Static pressure at inlet plane, mid-channel and exit plane of the wave rotor for axial and 15° blade.

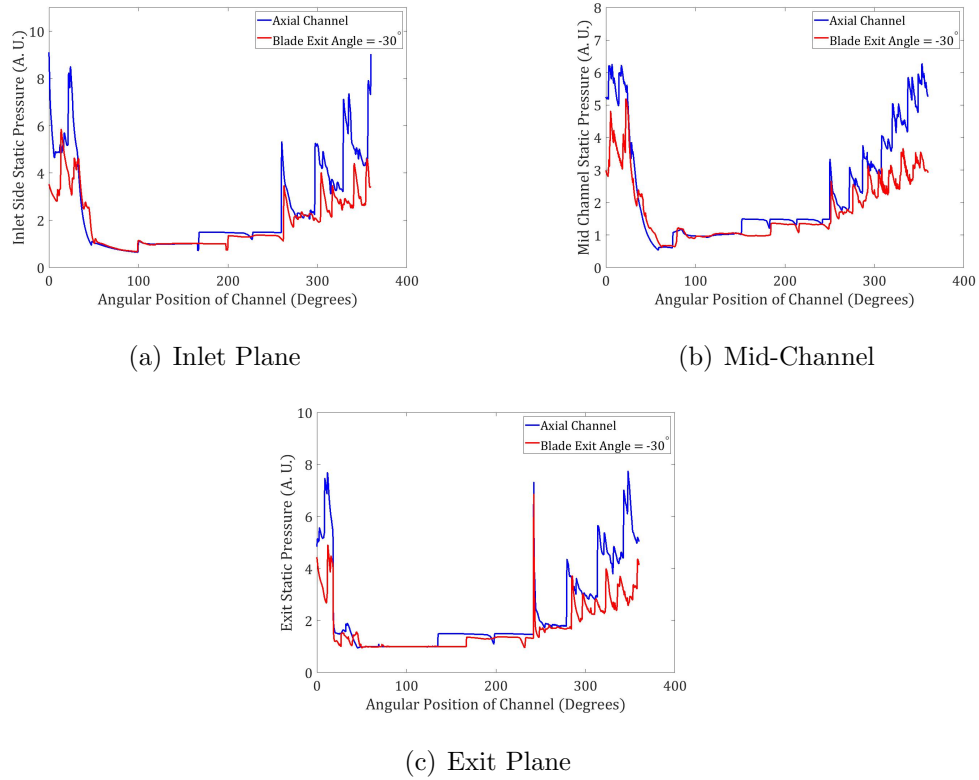


Fig. 2.32.: Static pressure at inlet plane, mid-channel and exit plane of the wave rotor for axial and 30° blade.

2.4.3 Shaft Work Estimation for Wave Turbine Combustor

The non-axial channel with internal combustion produces shaft work due to angular momentum change similar to the three-port wave rotor. The addition of combustion provides chemical energy from the reacting mixture that needs to be accounted in shaft work calculation. The chemical energy term needs to be included while calculating shaft work from energy conservation, while the shaft work calculation from angular momentum remains the same as Equation 2.17. The equation for shaft-work from energy conservation for wave turbines with internal combustion is given in Equation 2.25.

$$P_{EF} = Rh\rho^*a^{*3}\Omega'\left(\frac{1}{\gamma-1}\right)[EF'(Port_{out}) - EF'(Port_{in}) + (\gamma-1)\rho uZ_fq_f]n_{cy} \quad (2.25)$$

Where Z_f is the mixture fraction of fuel and q_f is the heat release from the fuel. Shaft work is now calculated using Equations 2.17 and 2.25 for blade angles ranging from 0 to -30° . The shaft work from the two methods are plotted in Figure 2.33. The two methods give similar results for blade angles of 0, 10 and 15° , while at other angles the difference is less than 10%. The difference between the two methods at some angles could be due to convergence. Currently the numerical simulation is considered to be converged only if the mass flow between inlet and outlet ports are balanced, however it may not be converged in terms of energy. There might be only a slight mismatch in energy between inlet and outlet ports leading to a small difference in shaft work calculation between the two methods. This will be corrected in future work. Another thing to note is that the shaft work is estimated for a wave turbine design without leakage, friction, heat loss and port opening time. So the shaft work estimated in the current work is in the ideal case without these loss mechanisms. Future work will consider these loss terms to estimate shaft work for a real wave turbine cycle.

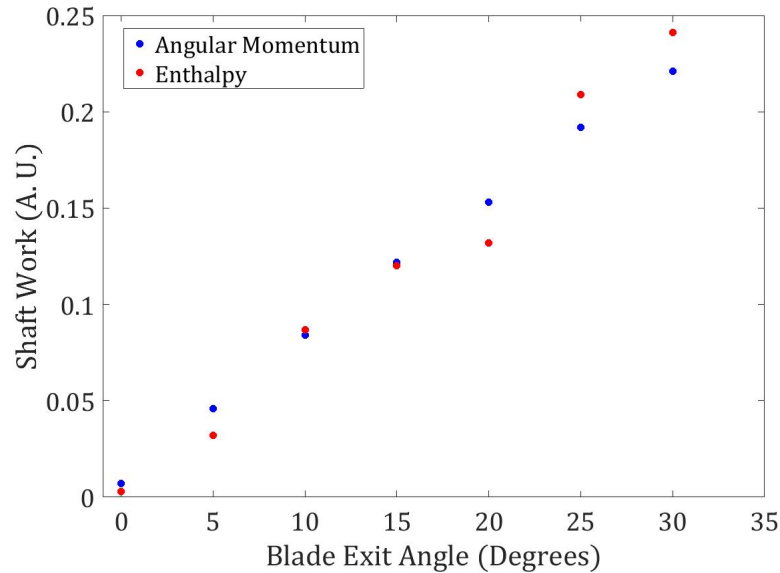


Fig. 2.33.: Shaft work estimates for wave turbine combustion for blade exit angles ranging from 0 to -30°

2.5 Identification of Potential Technology Needed to Improve Wave Rotor Combustion Turbine

A wave rotor is extremely complex and every aspect must be carefully considered and designed for efficient performance. In the case of non-reacting flow wave rotors, the inlet and exhaust ports must be timed precisely to match the arrival of compression and expansion waves. If the ports are opened for a longer time or closed too early, it will result in leaking fluid out through the inlet port or entraining excess fluid through the exhaust port. The inlet port opening, exhaust port closing and inlet port closing are the three parameters that need to be optimized for a given pressure boundary condition. A mismatch in the timing of one has a cascading effect on the other two, making it a complex optimization problem.

Introduction of combustion inside the wave rotor adds to the complexity. The exhaust port closing must be timed for the arrival of fuel injected through the inlet port, as any mismatch will result in fuel spillage. This spillage will have a cascading effect in subsequent cycles because less fuel is contained in the rotor and hence the combustion pressure rise is reduced which will result in weaker expansion and compression waves. Therefore, the shock wave at the inlet will not have strength to carry the fuel oxidizer mixture all the way to the exhaust end wall, resulting in a misfire. Another important aspect in a reacting flow wave rotor is high speed ignition and combustion. A typical wave rotor spins at approximately 3000 rpm, which translates to roughly 7.5 ms from the ignition port opening to the exhaust port opening. Implementing non-axial channels provides additional shaft work, resulting in an even smaller time delay between port opening. Therefore a fast-acting, efficient, ignition system with minimal ignition delay is vital for the success of wave rotor combustion.

Traditional spark plug igniters have been reported to have ignition delays of tens of milliseconds and require higher energy to create a spark discharge, making them less useful for wave rotor applications. Researchers working on wave rotor development have moved towards hot jet ignition, where a turbulent high pressure hot jet is created

in a pre-chamber and injected through the ignition port into the rotor. The turbulent jet entrains the fuel oxidizer mixture in the rotor and the high temperature of the jet ignites the mixture. A primary advantage of hot jet ignition is that the jet can penetrate far downstream in the wave rotor channel, igniting a much higher fraction of the reactive mixture. A significant disadvantage is the additional complexity involved in designing a pre-chamber to generate the hot jet. Also, hot jet ignition involves a considerable physical delay due to mixing time between the hot jet and cold reactant mixture, and the active radicals in the hot jet may get quenched due to the presence of a cold mixture [33]. These challenges with hot jet ignition motivated the current study to investigate using transient plasma ignition for wave rotor applications.

The challenges to optimize a wave rotor design were discussed in the preceding paragraphs. To summarize, the port timings, fuel injection and ignition can be listed as the main challenges and the three issues are interlinked. A non-optimal design of one aspect can have cascading effect on the other two. The port timings and fuel injection can be optimized using the quasi-1d model, but the ignition model requires experimental data. Therefore, the current study involves designing an experiment to explore plasma-assisted ignition concepts and using optical techniques to gather experimental data which can then be used in the wave rotor numerical model. It is anticipated that a volumetric transient plasma discharge can be used to provide a better ignition source compared to a hot jet or traditional spark ignition.

Traditional form of ignition depends on providing sufficient heat to the reacting mixture such that its temperature is raised beyond auto ignition temperature. However, in the case of nanosecond plasma discharges, energy is deposited for a short duration during which there is a high level of electronic excitation. As these electronically excited radicals relax back to their ground state, they react with other atoms and molecules to initiate oxidation of the reacting mixture. The relaxation also leads to ultrafast heating of the gas within the first few nanoseconds. The gas heating leads to production of shock wave which propagates through the medium and produce vorticity and mixing. In order to correctly model the ignition mechanism,

correct understanding of energy deposition into plasma volume, radical lifetime, the resulting gas heating and induced hydrodynamic effects are needed. These aspects will be carefully studied during the second phase of work. The energy deposition, radical lifetime and gas heating will be investigated through optical emission spectroscopy and the induced hydrodynamic effect will be investigated through high speed schlieren. The information from this investigation will lay a solid foundation for experimental plasma assisted ignition for wave rotors.

3. DESIGN OF PLASMA ACTUATOR FOR VOLUMETRIC IGNITION

From the preceding chapter, the optimization of wave rotor combustion turbine is a multi disciplinary problem and this dissertation will only focus on one aspect which is developing a new ignition source. Implementing plasma assisted ignition inside a wave rotor is extremely challenging since it is a rotating device, so designing the electrode configuration, precise timing and generation of plasma at different operating conditions is critical to its success. The wave rotor geometry is shown in Figure 3.1. The reacting mixture needs to be ignited as the channel comes in line with the ignitor. Plasma discharge needs to be created from the ignitor location shown in the figure. Since the rotor is spinning, it is difficult to mount electrodes penetrating into the channel. A possible way use plasma discharge in such a spinning device is to mount one of the electrodes at the ignitor location and have the plasma created to the walls of the channel which act as the second electrode. In the actual wave rotor device the cross-section of the channel is rectangular, so it will be similar to designing a pin-rectangle electrode configuration creating plasma discharge as shown in Figure 3.1. Such a plasma actuator has never been investigated to understand plasma characteristics or ignition and flame enhancement. However, there are prior experimental results for a pin-ring electrode configuration. In the current work, a pin-ring electrode will be used to understand discharge formation and its performance as an ignitor. These results will help in designing a pin-rectangle actuator for the wave rotor.

Prior to ignition testing it is important to characterize the discharge and arrive at the correct pulse parameters that can provide a more volumetric discharge within the ignition time scale of 1-50ms. As pointed out in Chapter 1, a lot of research has been done in a traditional pin-pin electrode configuration and very little in pin-

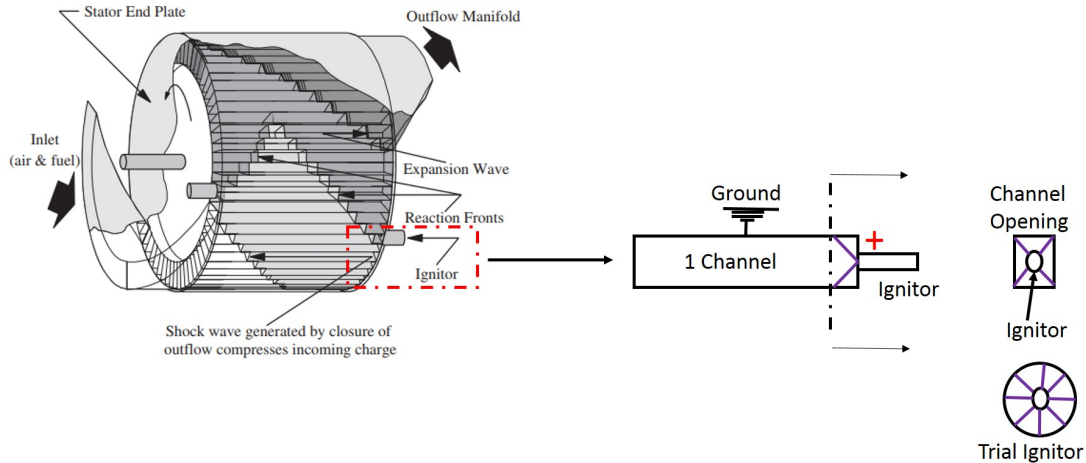


Fig. 3.1.: The different regimes of discharge integrated over 200ms of discharge time

annular electrode. However, research in pin-ring electrode has shown the existence of different regimes and dependence of regime transition on input voltage and repetition frequency. Given the complexity of the discharge, the primary focus will be to achieve a volumetric discharge and understanding how the geometry, electrode polarity, voltage and repetition frequency play a role in achieving the same. Once a clear understanding is obtained regarding the discharge, the focus will then shift to studying volumetric ignition inside a constant volume vessel. The two parts of this work will lay a good foundation for future efforts to study ignition in a flow using a pin-ring electrode.

3.1 Pin-Annular electrode discharge characterization

Nanosecond repetitively pulsed discharges have different regimes- corona, glow and streamer. Transition between these regimes are dependent on electrode gap, input voltage, repetition frequency and gas temperature. A detailed study was done by Pai et al. and provided a theoretical basis for such transitions at atmospheric pressure [34]. In this framework Pai et al. use dielectric breakdown, avalanche to

streamer transition and thermal ionization instability to explain corona to glow and glow to streamer transition. The dynamics of glow regime has three events. First phase is a cathode directed streamer which creates a conducting channel in the gap. During the second phase the return wave redistributes potential, creating a plasma structure similar to a glow discharge. Now there is a positive column and a space charge at the cathode. Final phase is driving the current through the discharge channel. The Laplacian electric field is used to describe the field for the streamer phase and for the conduction phase, it is assumed that space charge imposes a cathode fall region and a uniform field in the positive column.

From the three phases you can observe corona to glow transition and glow to streamer transition in NRP discharges. In order to achieve corona to glow transition, the applied field must be strong enough to initiate avalanche to streamer transition and maintain plasma during the conduction phase. The breakdown voltage is used to identify corona to glow transition. For the next phase of glow to streamer transition, a thermal ionization instability is used to explain the process. In the case of NRP discharges, there is incremental heating over a number of pulses. Gas heating and ionization couple with each other during the pulsed period. It was also experimentally observed that NRP glow to streamer transition happens after a number of pulses. This indicates the process is a slow one and happens over a millisecond time scale, while the chemical kinetic mechanisms happen over nanosecond timescale. Due to long time scale for this transition, thermal ionization instability is considered the driving force for this transition.

To study the regime transition for pin-ring electrode, an experiment is performed where discharge is created by varying voltage from 12 kV to 20 kV, repetition frequency is changed from 1 to 50kHz and the number of pulses to in the pulse train is set to 500. This provides 500ms of discharge time at 1kHz and 10ms at 50 kHz. In each experiment the first 1000 pulses in the train are used to establish a "steady-state" plasma for all pulser parameters and the last set of 500 pulses are used for imaging. The electrodes used for this experiment is a 1 inch diameter stainless steel ring

machined to be concentric with a 1/8" tungsten pin electrode. Both the electrodes are machined to minimize surface roughness and are cleaned with iso-propyl alcohol before every experiment. The electrodes are placed on opposite ends of an acrylic mount that is machined precisely so the two electrodes are concentric. The tip of the center electrode is aligned with the end of the cylinder electrode to produce plasma in a single plane. An ICCD camera is used to visualize the discharge and identify the different regimes. The images from the iccd camera are all long exposure images that provide an image integrated over the discharge time. The high voltage pulses are generated using a custom-built NSP-3300-20-F nanosecond pulser from Eagle Harbor Technologies. The pulse parameters can be varied, with peak voltage up to 20 kV, pulse duration from 20 ns to 110 ns, and pulse repetition frequency (PRF) up to 400 kHz. The pulser is powered by a TDK-Lambda power supply that can operate between 0 and 600 V DC. The pulser output scales linearly with the power supply input voltage, where 0-600 V on the power supply is equivalent to 0-25 kV at the output; however, the resistive load at the pulser output restricts the voltage to a maximum of 20 kV. The output of the pulser is floating and the potential is symmetric with respect to ground. Therefore, during a pulse one electrode is at positive potential while the second electrode is at negative potential. For the current experiment to identify the regimes, the pin electrode is set to positive potential. This is done mostly following previous work by other research groups for this electrode configuration. A voltage probe and current probe are connected at the output to get voltage and current characteristics of the discharge. The product of voltage and current integrated over time provides energy per pulse deposited to create the discharge. The experimental setup is shown below in Figure 3.2. The results from this experiment show the existence of three regimes-streamer corona, distributed spark and localized spark. The streamer corona is formed at low repetition frequencies and low input voltage, while the distributed spark is formed at intermediate frequencies of 10kHz and the localized spark is formed at high repetition frequencies of 50kHz. The three regimes can be seen in Figure 3.3 The energy per pulse at different applied voltages and repetition frequency

is shown below in Figure 3.4. The energy plot shows that as the pulse repetition frequency is increased, there is a decrease in the energy per pulse to create the discharge. At the same frequency there is an increase in energy per pulse as the voltage is increased. A similar observation was made by Starikovski *et.al.* [35] for a burst of 100 pulses was used to create the discharge.

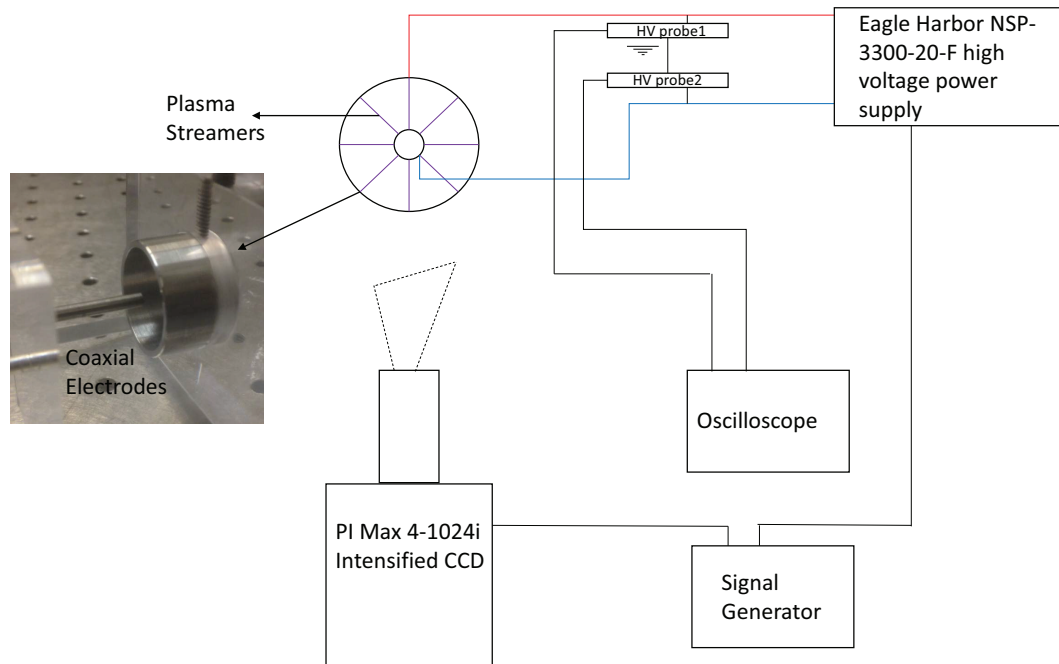


Fig. 3.2.: Schematic of initial experiment for imaging plasma formation in quiescent non-reactive environment at atmospheric pressure

Having seen the different regimes with a burst of 500 pulses, it made more sense to observe the trends at shorter time scales relevant for an ignition event. Generally an ignition event happens around 10ms, so a total discharge time of 10ms is taken to study the regime transition. The total discharge time is held fixed and number of pulses in the burst is varied for the different repetition frequencies to match the discharge time. Currently only images are captured using an iccd camera, however both current and voltage measurements will be captured in the next phase of work to estimate energy per pulse. The discharge for different frequencies is shown below

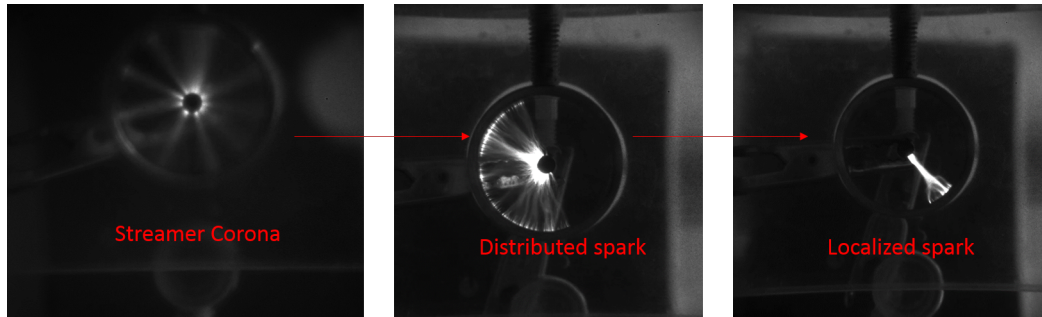


Fig. 3.3.: The three different regimes observed when a burst of 500 pulses is used to create discharge in pin-ring electrode

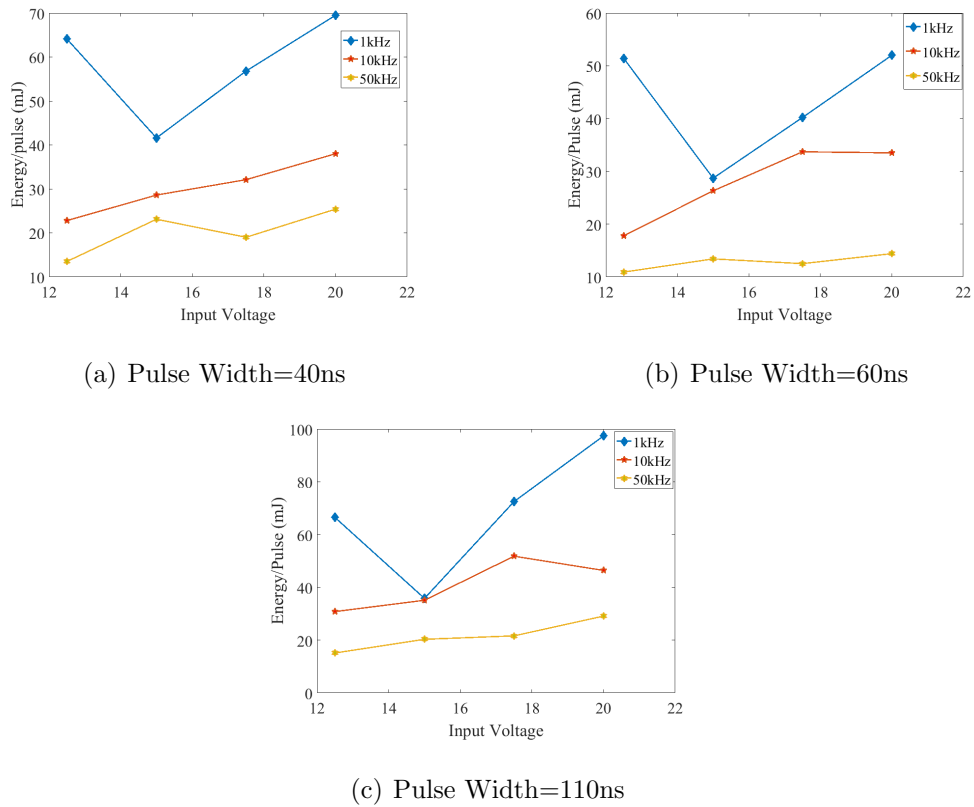


Fig. 3.4.: Energy per pulse at different applied voltages, repetition frequency and pulse width

in Figure 3.5. From the images, it can be observed that at 1kHz, the discharge with 10 pulses has distinct streamers. As the frequency is increased to 5kHz, the number of

pulses in the discharge increases leading to the formation for a localized hot spark and few faint streamers. With further increase in frequency a burst of 100 pulses at 10kHz produces two hot spots and other faint streamers. With 500 and 1000 pulses in the discharge there is a distributed spark. It is clear from the images that its not just number of pulses but also depends on frequency with which the pulses are sent. This clearly shows that as the number of pulses is increased in the discharge, thermal ionization instability kicks in to give localized sparks. Analysis similar to Pai *et.al.* [34] will be used to study this transition event.

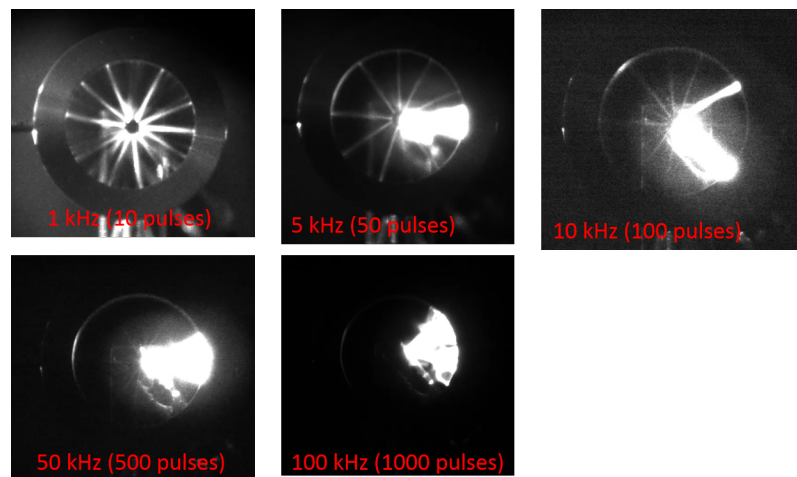


Fig. 3.5.: The different regimes of discharge integrated over 10ms of discharge time

When the discharge time is increased to longer durations of the order of 200ms, the discharge tends to become more uniform. Although this time scale is not relevant for ignition, it may well be useful for other applications like flame stabilization and control of combustion instability. The images show that as the frequency and number of pulses are increased the area covered by the discharge increases and at 50 and 100 kHz, the discharge has filled the entire circular cross-section. It can be observed that the discharge area is dependent on repetition frequency because in all the cases the total discharge time is maintained constant at 200ms but only at higher frequencies the discharge is more uniform. It should be noted that the image captured at 50 and 100kHz are of long exposure and not instantaneous. A high speed camera was used to

capture instantaneous snapshot of the discharge and it was found that the discharge forms at one location and spins around the circumference to fill the entire area.

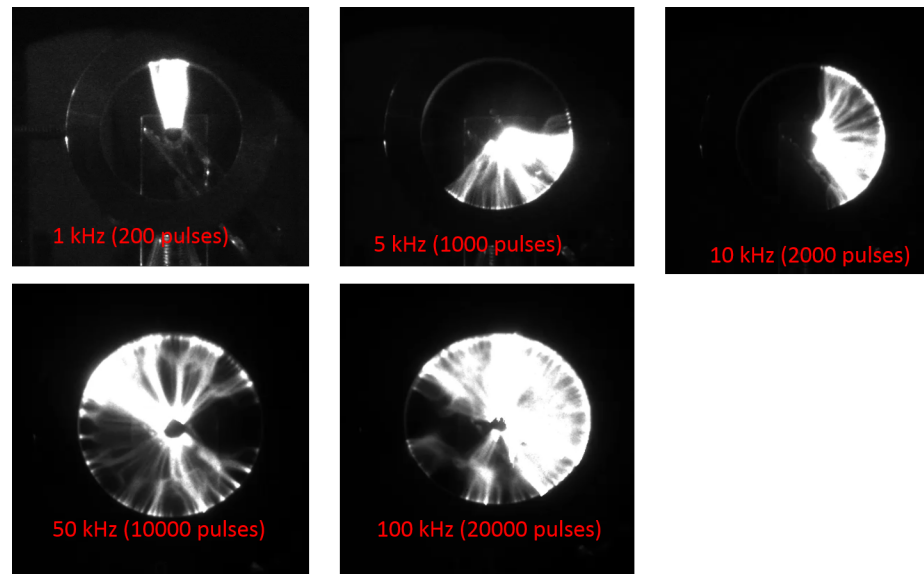


Fig. 3.6.: The different regimes of discharge integrated over 200ms of discharge time

3.1.1 Simultaneous ICCD and Schlieren imaging

Transient plasma discharge have been found to heat the surrounding gas that produces a shock wave. As the shock propagates out from the electrode gap, the baroclinic effect induces vorticity and mixing. The density gradients and shock wave can be visualized through schlieren imaging. The experimental setup is shown below Figure 3.8. Since the flow induced by the discharge diffuses out axially and tangentially, it is important to get both perspective from schlieren. It is possible that the gas heating that moves tangentially is causing thermal ionization instability and leading to movement of the discharge from one location to the other. First the schlieren is done looking perpendicular to electrode gap and then schlieren is done looking straight into the gap. The iccd camera provides a long exposure image of the discharge to correlate with the schlieren image. There are three tests which are shown below in

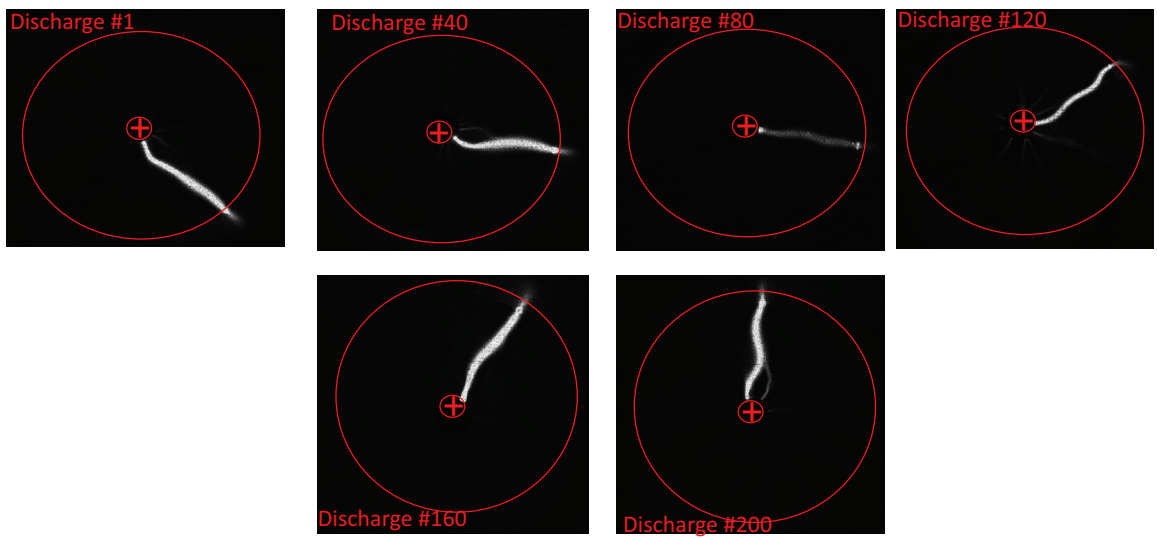


Fig. 3.7.: Spinning of positive polarity discharges recorded on a high speed camera at 10000 FPS

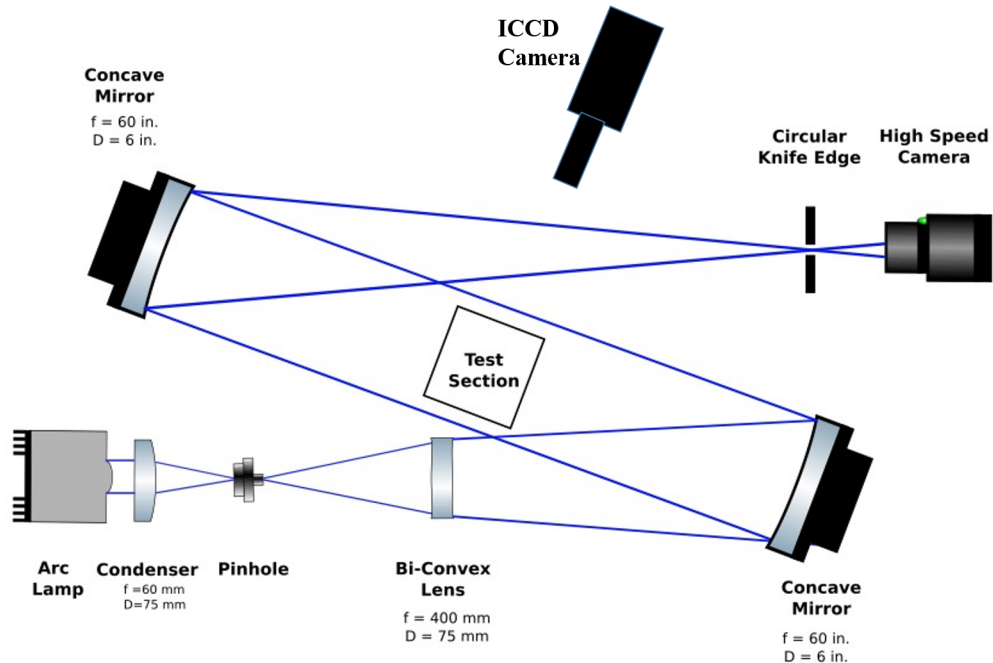


Fig. 3.8.: Experimental setup for simultaneous schlieren and iccd imaging

Figures 3.9-3.11. The first image is for a discharge at 1kHz and a total discharge time of 10ms, second image is for the same discharge time but at 100kHz and the last image is for a discharge time of 200ms at 100kHz. In the first case at 1kHz, there was no flow observed to diffuse in the axial direction, therefore only the view looking into the ring is shown. Although the streamers are bright in the iccd image, the gas flow is very weak. As the number of pulses in increased at higher repetition rate, there is lot more flow induced by the discharge. For a 200ms discharge time, the iccd image shows a uniform discharge and the corresponding schlieren image indicates the fast gas expansion and vorticity induced by the discharge. As mentioned earlier, this long time scale may not be beneficial for ignition but can be used for flame stabilization or combustion instability.

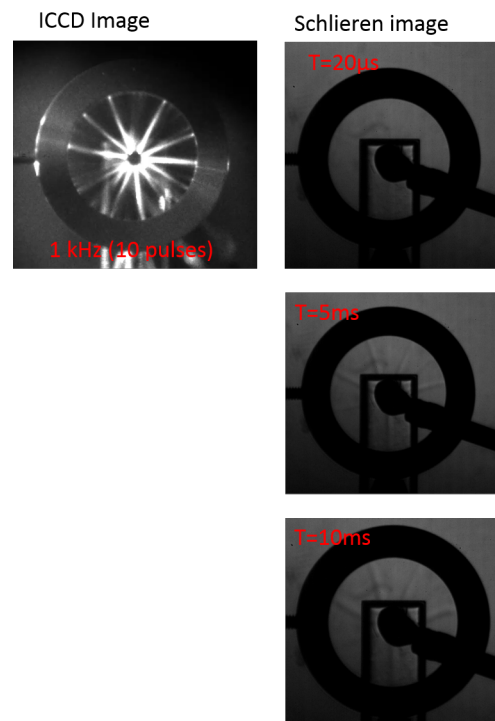


Fig. 3.9.: Long exposure iccd image for a 10ms discharge at 1kHz and gas expansion observed through schlieren at different intervals of time



Fig. 3.10.: Long exposure iccd image for a 10ms discharge at 100kHz and gas expansion observed through schlieren at different intervals of time



Fig. 3.11.: Long exposure iccd image for a 200ms discharge at 100kHz and gas expansion observed through schlieren at different intervals of time

3.1.2 Studying the effects of electrode polarity

Since the pulser is on floating ground, both the electrodes are at high voltage. One electrode will be at positive high voltage and the second electrode will be negative high voltage. This helps in switching the polarity between the two electrodes. In the case of pin-pin electrode, the polarity may not play a significant role. But in the case of pin-plane, pin-ring or a dielectric barrier discharge, the characteristics of the discharge will be different depending on the potential of the electrode. In the case of pin-ring electrode, when the pin electrode is at positive electrode a cathode directed streamer is formed and when the pin electrode is at negative potential then anode directed streamers are formed. The anode directed streamer fades and disappears halfway through the gap, whereas the cathode directed streamer slows down to a constant speed as the streamer propagates through the gap [36] due to photoionization and electric field direction. Even in the case of plasma jets, anode driven plasma plume is found to travel three times longer than cathode driven plume. The reason for this behavior is attributed to difference in direction of transient electric field from the high voltage pulse and the field formed between propagating ionization fronts and charge accumulated dielectric surface at the nozzle exit [37]. This provides another tool to classify the discharge based on polarity, a preliminary study of which was presented earlier in the year [38].

When the central electrode is at negative polarity (Figure 3.12) and at 1 kHz PRF, the discharge appears quite uniform with diffuse discharge channels spaced at even intervals around the electrode circumference. There is little change in the discharge appearance when the pulse duration is increased from 40 to 110 ns. The plasma mode is similar for 10 kHz PRF, though the discharge channels appear a bit more constricted and the plasma emission intensity increases significantly as the pulse duration increases. The discharge propagation distance is also smaller for 10 kHz vs. 1 kHz, except for the case with 110 ns pulse duration. At the highest PRF (50 kHz) the discharge channels form distinct streamers and both the plasma propagation distance

and the emission intensity decrease drastically. The drop in emission intensity forced the use of intensifier gain on the camera and therefore saturating some of the images. To maintain consistency, the number of pulses imaged was limited to 500, but in future work a larger number of pulses may be used to increase the total emission. As the voltage is increased, the negative polarity discharge transitions to an arc and behaves like the positive polarity discharge for a few pulse parameters as shown in 50 kHz for Figures 3.14 and 3.16 and most of Figure 3.18. The positive polarity discharge on the other hand forms an arc discharge for most of the pulse parameters. At low PRF, it starts off as a single arc that spins about the axis and at higher PRFs, a higher number arcs coalesce together to form an arc at a random spot on the outer cylinder. The fact of spinning discharge was confirmed through the use of a high speed camera and the images are shown in Figure 3.7 . The discharge was created with a PRF of 2 kHz and the high speed camera was operated at 10000 frames per second. The high speed video showed that when there is a positive polarity discharge, there is one strong arc and several other weak ones. The strong arc is seen rotating by more than 90° in Figure 3.7.

To summarize, at the lowest peak pulse voltage, the following observations can be made for negative polarity discharges where the central electrode is at negative potential and the images are shown in Figure 3.12:

- For low to moderate PRF (1-10 kHz), the discharge takes the mode of diffuse discharge channels spaced somewhat evenly around the electrode.
- As the PRF increases, the discharge channels become more constricted and their propagation distance also decreases.
- At low PRF (1 kHz) and high PRF (50 kHz), an increase in pulse duration does not appear to have much effect on the plasma; at moderate PRF (10 kHz), increasing the pulse duration from 60 to 110 ns causes a significant increase in both plasma propagation distance and emission intensity.

- The discharge channels did not reach the outer electrode for any combination of pulse parameters.

While for the positive polarity discharges shown in Figure 3.13 where the central electrode is at a positive potential and a low input voltage of 14.6 kV is supplied, the following observations can be made :

- For most of the pulse parameters, an arc is formed on the outer cylinder and tends to spin around at the pulse repetition frequency. This can be observed in the images from the high speed camera.
- At low PRF (1 kHz), one single arc is formed at a random spot for 40 and 60 ns, while for the high pulse width of 110 ns a higher number of arcs Coalesce over one half of the outer cylinder and propagate the entire distance between the two electrodes. However, there are also some tiny streamers on the opposite half which do not propagate the entire distance.
- At an intermediate PRF (10 kHz), there are a large number of constricted arcs for higher pulse widths, while for the low pulse width of 40 ns, it's not highly constricted but there are a lot more streamers compared to PRF of 1 kHz. Unlike the low PRF, the tiny streamers are missing in this case.
- At high PRF of 50 kHz, the discharge is again to a random spot, but the discharge channels tend to twist and bend on their way to the cathode. This observation is true for all the pulse widths. With such twisting and bending, the flowfield induced by this discharge can be interesting to study as part of future work.

As the input voltage is increased to 16.7 kV, the negative polarity discharge behaves similar to the low voltage case with increase in emission intensity at 10 kHz and constricted distinct streamers at 50 kHz. The only difference is at high PRF and pulse width of 60 and 110 ns where the discharge behaves similar to positive polarity discharge as shown in Figure 3.14. The positive polarity discharges on the other hand

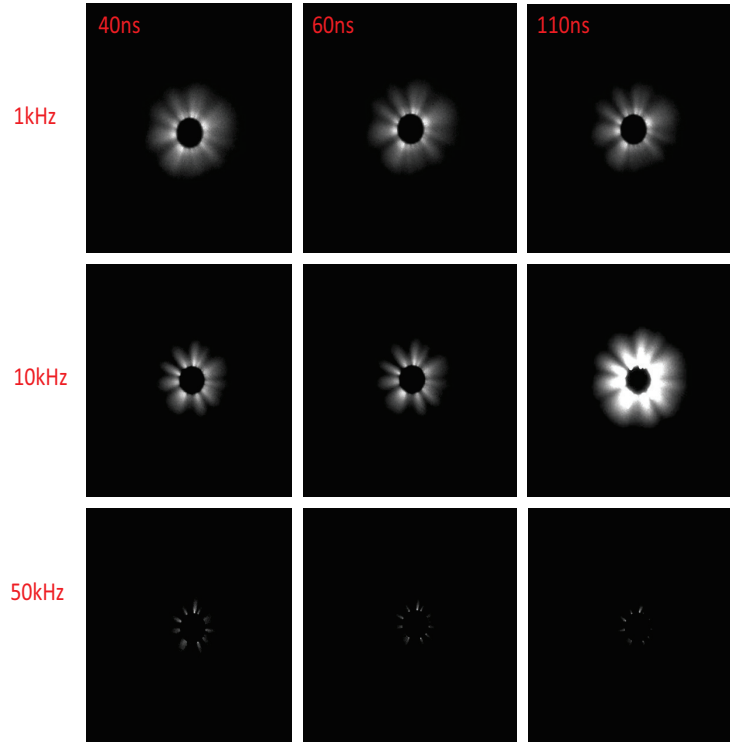


Fig. 3.12.: Negative polarity discharge with central electrode as cathode and pulser input voltage=14.6 kV

appear to be getting stronger at 1 kHz and behave similar to the low voltage case at higher PRF as shown in Figure 3.15. A further increase in voltage to 18.75 kV shows that the negative polarity discharge show the same structure as the low voltage case at low and intermediate PRF and behave same as positive polarity discharges at high PRF as shown in Figures 3.16 and 3.17. At the highest input voltage, the two polarity discharge have the same structure except at low pulse width of 40 ns and low to intermediate PRF of 1-10 kHz as shown in Figures 3.18 and 3.19.

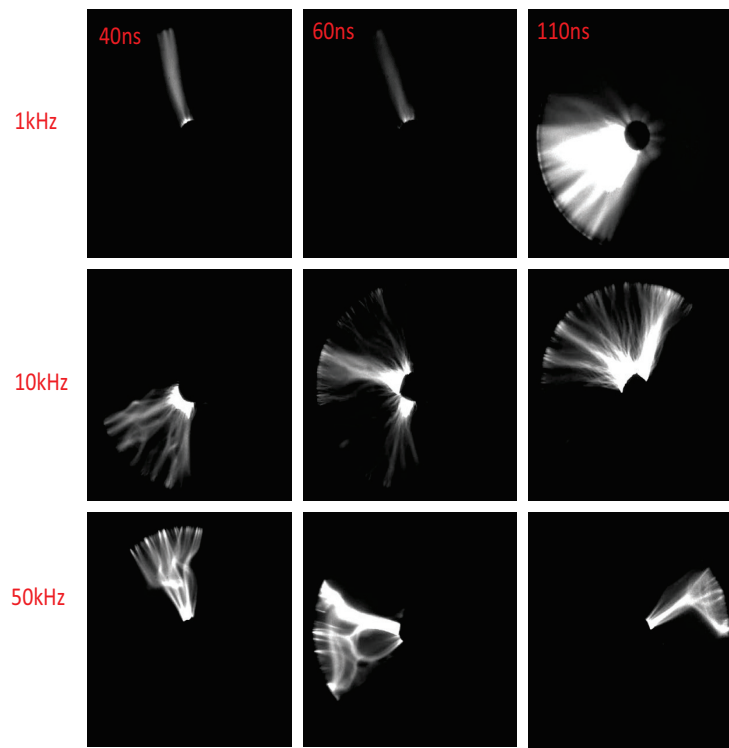


Fig. 3.13.: Positive polarity discharge with central electrode as anode and pulser input voltage=14.6 kV

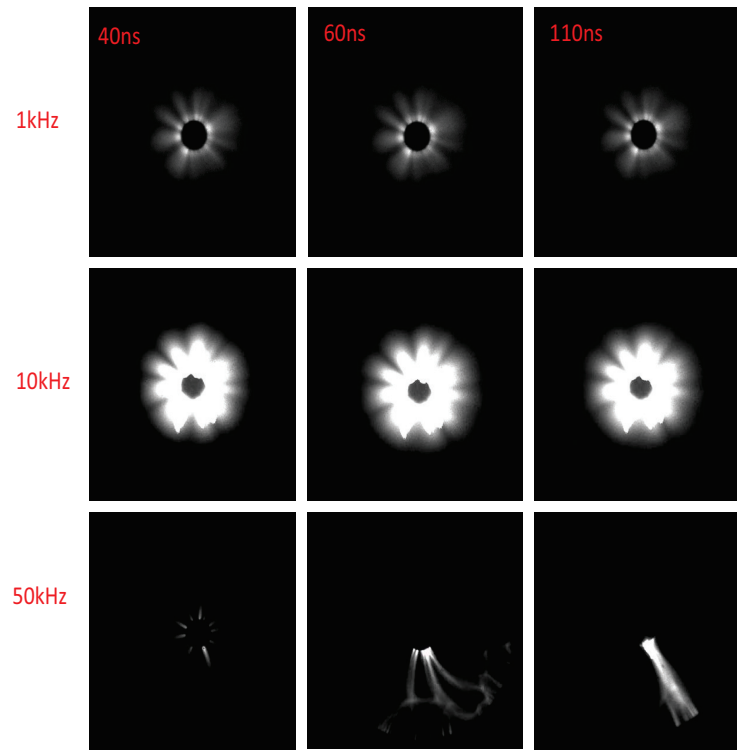


Fig. 3.14.: Negative polarity discharge with central electrode as cathode and pulser input voltage=16.7 kV

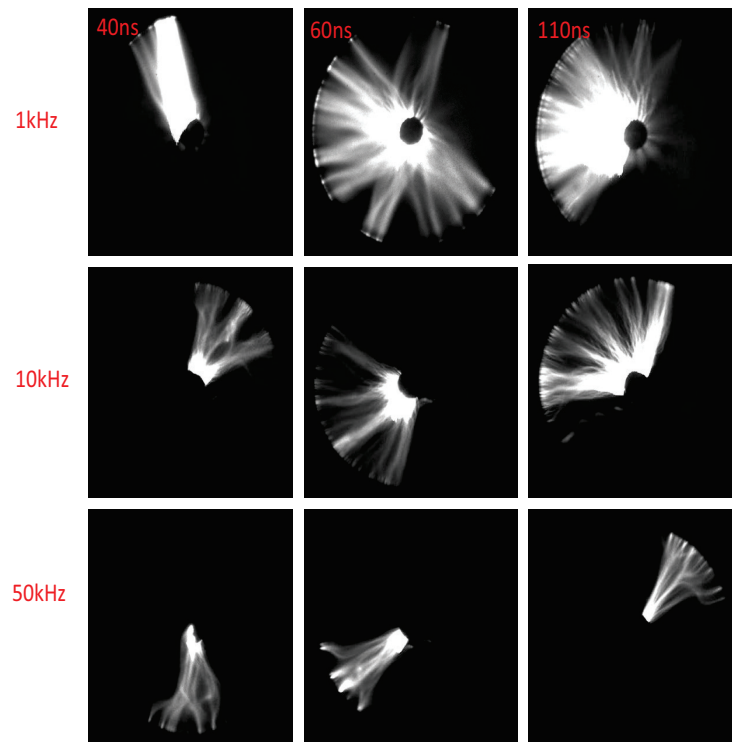


Fig. 3.15.: Positive polarity discharge with central electrode as anode and pulser input voltage=16.7 kV

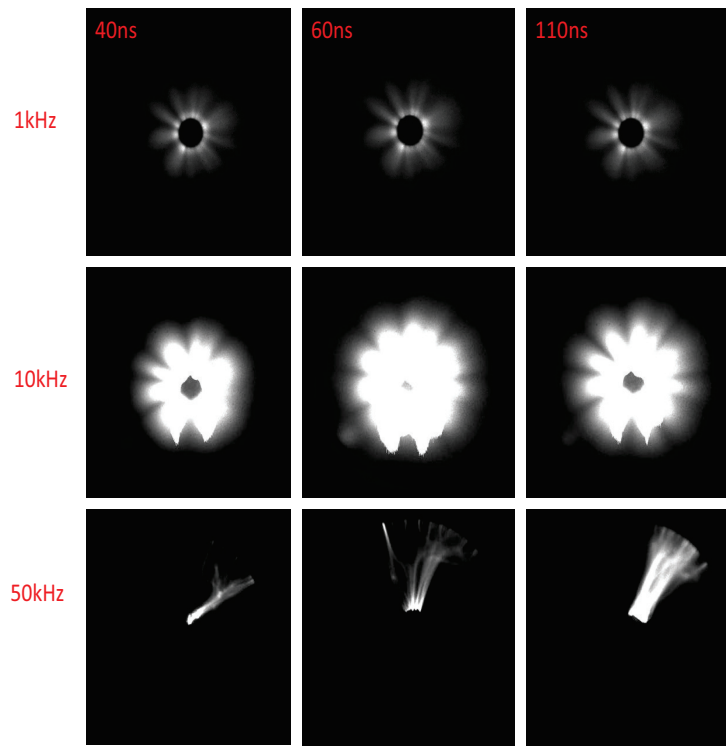


Fig. 3.16.: Negative polarity discharge with central electrode as cathode and pulser input voltage=18.75 kV

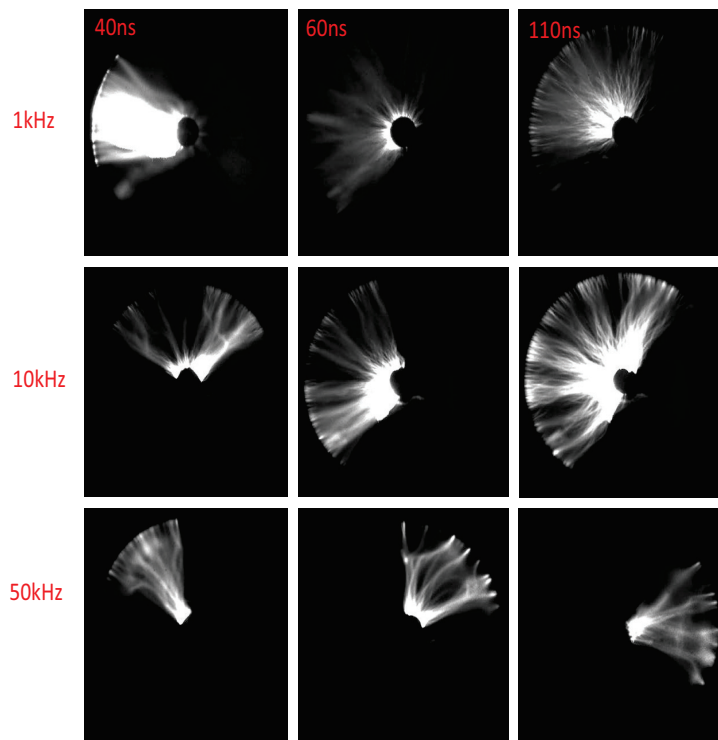


Fig. 3.17.: Positive polarity discharge with central electrode as anode and pulser input voltage=18.75 kV

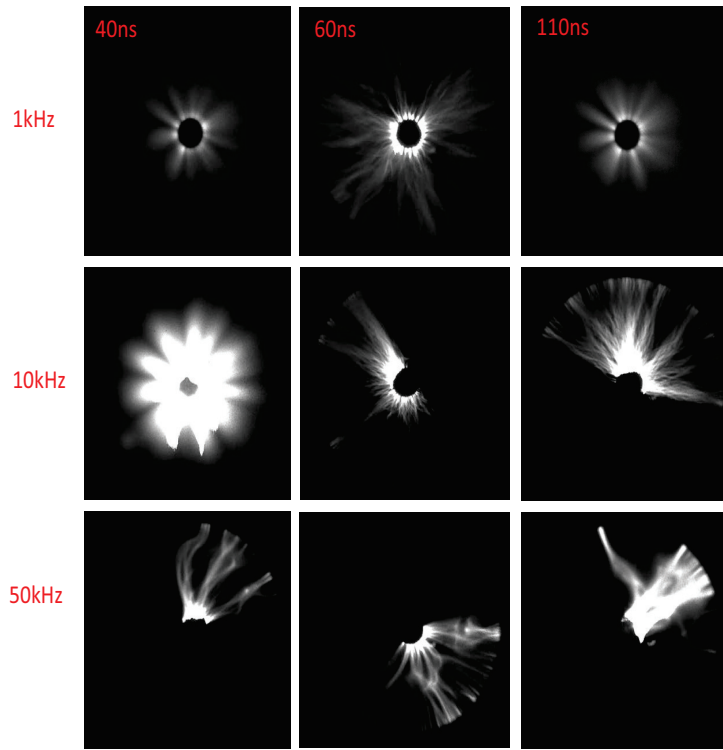


Fig. 3.18.: Negative polarity discharge with central electrode as cathode and pulser input voltage=20.8 kV

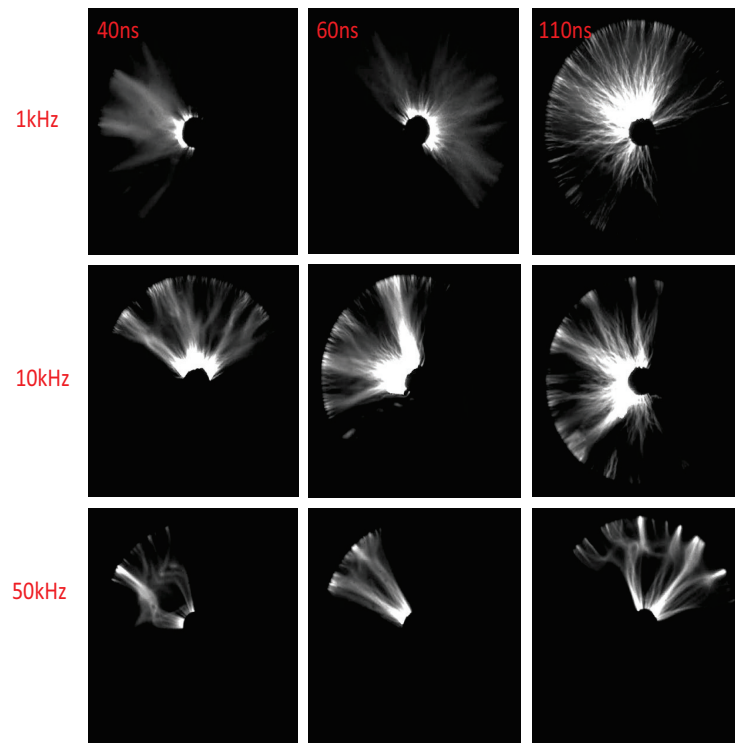


Fig. 3.19.: Positive polarity discharge with central electrode as anode and pulser input voltage=20.8 kV

4. DEVELOPMENT OF A NOVEL EXPERIMENTAL TECHNIQUE FOR MAKING ULTRAFAST MEASUREMENTS OF PLASMA DISCHARGES

4.1 Introduction to Streak Camera and its Working Principle

Streak cameras are designed to capture ultrafast events such as laser pulses, detonation waves and plasma discharges and provides information on intensity. vs time. vs. position. The use of streak cameras dates back to the 1920s when it was developed by the mines and explosives research community to study the propagation of a detonation wave from an explosive impacting the ground. Streak photography as it was known back then was performed using a slit type high speed camera. In this type of camera, a film fixed to a rapidly rotating drum is made to move past a fixed slit [39,40]. A variant to the rotating drum system is the rotating mirror type, where a mirror is rotated at high speed with respect to a fixed slit [41].

Streak photography was started with these rotating drum cameras, but invention of electron camera at Bell Labs moved the device forward [42]. In the electron camera which is also used as a television transmitter, an image is incident on a photoelectric cathode resulting in a stream of electrons. By applying a suitable electromagnetic field, the stream of electrons is made to move across a scanning aperture. Once the electrons pass through the aperture, they are multiplied and reconverted to photons which are then displayed on the detector.

The transition from a rotating drum streak photography system to electronically operated device happened in 1966 with the use of Electron-optical image tubes and image tube streak camera for measurement of ultrafast laser sources [43]. In this camera, a slit image that needs to be time resolved is focused on a photocathode that converts the incoming photons to electrons. The electrons are then accelerated

through a deflection plate. As the electron pass through the two deflecting plates, they are deflected in a direction perpendicular to both the deflecting field and axial magnetic field applied. In this design, there was a gating mesh that would reflect the electrons back though the deflecting field. After multiple reflections, the electrons are spatially separated in a direction perpendicular to the slit. The spatially distributed electrons are converted back to photons and read on a detector, but it was recorded over multiple frames and not single shot. The same research group used a commercially available image tube and applied a streak deflection voltage ramp to write an image having a time resolution of roughly 6ps and was photographed on a polaroid film [44, 45]. The same was patented by Bradley [46].

The streak camera was commercialized by Hamamatsu Photonics through the introduction of compact streak tubes and cameras [47, 48]. The streak tubes had temporal resolution from 2-10ps and consisted of streak tubes, automatic data acquisition system vidicon camera and video analyzer employing a microcomputer. The same company modified the design by using a multi-channel plate instead of intensifier tube and real time processing instead of using photographic film. The principle still remains the same, with input optics focusing slit image onto the photocathode, then the electrons pass through streaking field and multiplied by an multi-channel plate. After the MCP gain, the streak image at the phosphor screen is then focused using output optics onto an external focal plane. The device also consists of sweep generator with avalanche transistors and control circuitry. The image was readout using vidicon cameras [49, 50]. For more historical background into streak cameras, one can refer to other review papers [51–53].

In the current work, a high dynamic range Streak tube/CCD system (C13410A/Orca R2 CCD) from Hamamatsu is used. A schematic of the streak tube is shown in Figure 4.1. Consider a space and time varying light pulse like a flashing LED, moving shock wave, detonation wave or decay of photon emission at the probe volume as shown on the left of Figure 4.1. Obtaining a single shot acquisition of the entire event is impossible with any available CCD or CMOS cameras. However, the use of streak

camera makes capturing ultrafast light phenomena possible. In a streak camera, the light pulse enters through a fine slit of say $20\text{-}50\ \mu\text{m}$. The slit image is then projected on the photocathode using input coupling optics. The photons are converted to electrons at the photocathode and then accelerated through an accelerating mesh. The main part of the streak tube is the sweep electrode, where an electric field is applied by a sweep circuit. As the electrons arrive at the sweep electrode, an electric field is applied based on the sweep time which in the current system can be between 500 femtosecond to 1 millisecond. Based on the time of arrival of electrons at the sweep electrode, they are swept at different angles. The swept electrons then enter the multi-channel plate where they get multiplied according to the applied gain. The electrons are then converted to photons at the phosphor screen. The photons are then detected using a CCD camera, where the vertical axis represents time and horizontal axis represents space. So when a streak sweep of 100 nanoseconds is applied to the streak tube, the 1024 pixels along the vertical direction will be swept in 100 ns, providing a temporal resolution of 100 picoseconds. The streaked image on the CCD represents a space-time or wavelength-time plot. In the current work, the streak tube/CCD assembly is used to directly image nanosecond plasma discharges and also coupled with a spectrometer to perform time resolved spectroscopic measurements.

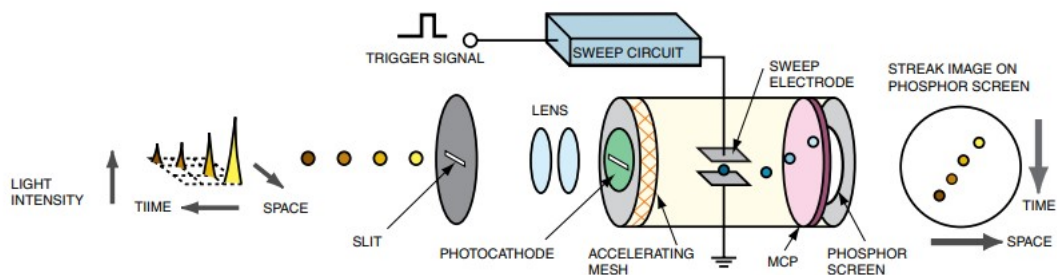


Fig. 4.1.: Schematic to show internal working principle of a streak tube [54]

4.2 Need for Streak Camera Based System to Study Plasma Discharges

The streak camera was initially developed to study ultrafast phenomenon such as ultrafast laser pulses. Plasma discharges and its emission also occur over ultrafast timescales, making it an ideal application for the streak camera system. However, the use of streak camera for plasma discharges has been limited over the past decade, even though the progress of application of plasma discharges to various applications have increased.

Over the past decade, the streak camera has been used for laser induced breakdown spectroscopy, thin film spectroscopy and plasma discharges. Aleksandrov *et.al.* used a sub-picosecond streak camera with a broadband spectrometer to obtain temporal and spectral profiles of the emission from the plasma assisted ignition [55]. The imaging was obtained in a stoichiometric mixture of propane and oxygen diluted with argon at a pressure of 0.4 bar and 1500 K. Rakitin *et.al.* used a streak camera to image a nanosecond plasma discharge in air at 1 and 0.3 bar [56]. Ceccato *et.al.* used a streak camera to image a plasma discharge for a pin-plane electrode configuration, however the streak sweep was slow at $1\mu s$ [57]. Morris *et.al.* used a streak-spectrograph combination to perform temperature analysis from electrically exploded Ni/Al nanolaminates. Popov *et.al.* used a streak-spectrograph combination to obtain time resolved emission from a cathode spot at vacuum discharges [58]. Thomas *et.al.* used a streak camera for time resolved spectroscopy of laser induced breakdown in water [59]. The streak camera system should have been ideally utilized more for nanosecond plasma discharge applications, but so far an intensified CCD has been preferred for imaging and optical emission spectroscopy of nanosecond plasma discharges.

In order to understand the physics of formation of nanosecond plasma discharges, radical production and ultrafast heating, it has been a standard practice to use fast gate intensified CCDs for directly imaging the plasma and optical emission spectroscopy. Direct imaging of plasma discharge provides time resolved information

regarding formation of plasma and understanding how different regimes appear in these discharges. In the case of optical emission spectroscopy, molecules excited to higher electronic states by the plasma discharge, emit photons which are dispersed through a spectrometer and imaged on the CCD. The spectral information can be compared to simulation to obtain quantitative information such as rotation and vibration temperature. The temporal resolution for both the experiments are restricted by the gating time of the CCD which is generally 2-3 ns. Since the readout rate of CCDs are not high enough compared to CMOS cameras, the repetition rate of CCDs are slow to capture the entire emission from a single plasma discharge. In such a case, a single image with high time resolution of 2-3 ns is captured from one plasma discharge and many such images from multiple plasma discharges are accumulated to improve signal to noise ratio. If the plasma discharge produced has a pulse duration of 100 ns, this single image acquired will represent only a fraction of the plasma discharge. The delay on the camera is then altered to get images at different time instants of the plasma discharge. The images acquired at different time instants are then stitched together to obtain time resolved images or spectra of plasma discharge.

There is a fundamental flaw in this approach which makes the use of streak camera absolutely necessary. First, in the case of direct imaging, since a short gate is used, the signal to noise ratio is not great and generally to improve signal to noise ratio, multiple images are accumulated. However there is a lot of electronic jitter in the experimental system due to different components such as high voltage power supply, delay generators and BNC cables. This creates an uncertainty in the accumulation of images with respect to the time of plasma discharge. Second, in the case of optical emission spectroscopy, there is still the same uncertainty described for accumulation, but in addition to jitter uncertainty, the temporal resolution is not good enough for spectroscopy. The overall emission from an excited molecule is roughly 15-20 ns, unless the species emits for a longer time, which means that if the gating time of the detector is 2-3 ns, then the number of data points will be less than 10. The gating time of 2-3 ns is also too long and tends to average the temperature.

The use of streak camera eliminates all the uncertainties involved in timing the experiment and provides a single shot acquisition of the entire event instead of changing the delay to record the event from multiple discharges and stitching them together later. The entire event is captured by the streak camera as long as it stays within the sweep window.

4.3 Characterization of Experimental System Using a CW LightSource

4.3.1 Experimental System

In the current work, a streak camera was used with and without spectrometer for optical emission spectroscopy [60] and direct imaging [61], respectively, of nanosecond plasma discharges with extremely high temporal resolution. The experimental systems for the two experiments have different light collection optics. The two experimental systems are shown in Figure 4.2 and Figure 4.3. In the experiment to image the plasma directly, shown in Figure 4.2, an off-axis parabolic mirror with 4 inch reflected focal length was used to collect the plasma emission and a spherical lens with 10 inch focal length was used to form the image on the slit of spectrometer. The use of 10 inch focal length lens magnified the image at the streak slit in the ratio of two focal lengths. However, since the spherical lens magnified the image in both the vertical and horizontal direction, a cylindrical lens was added downstream of the spherical lens to reduce magnification in the vertical direction. This stretches the image of the 1 to 3 mm electrode gap to 2.5-7.5 mm at the streak tube slit so that a higher percentage of pixels along the horizontal direction are used while imaging the plasma.

For optical emission spectroscopy the streak camera needs to be coupled with the spectrometer as shown in Figure 4.3. The experiment used a Hamamatsu C13410-01A/Orca R2 streak tube/CCD assembly along with Princeton Instruments 2500i spectrometer. In order to place the image plane of the spectrometer on the streak tube slit, a lab jack and motorized translation stage are used for vertical and horizontal

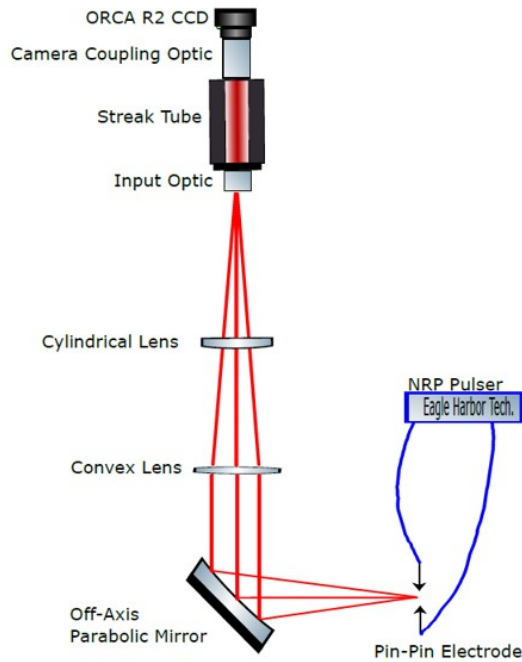
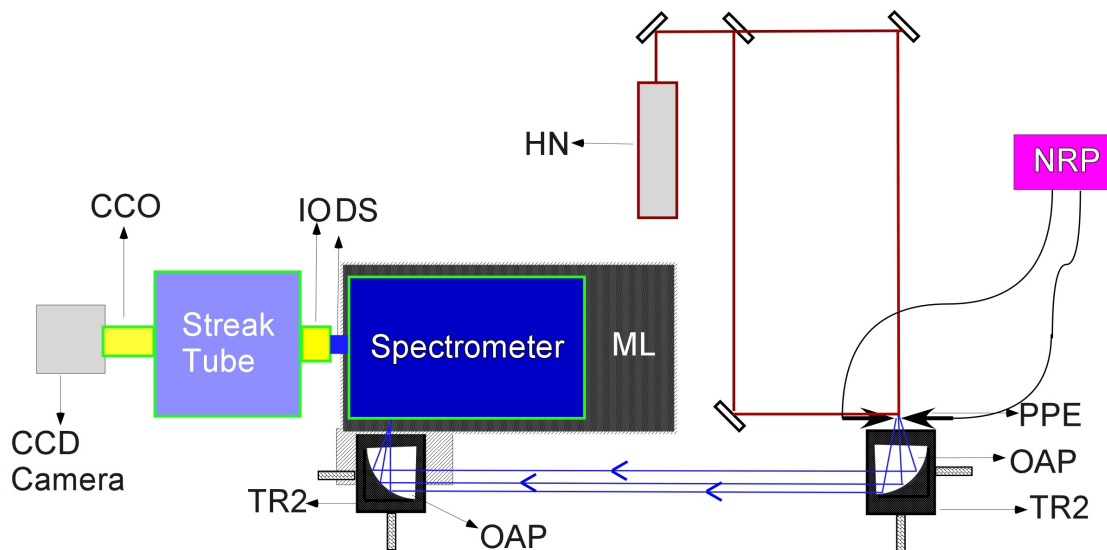


Fig. 4.2.: Schematic of the experimental system for Streak-Direct Imaging of NRP plasma discharges [61]

motion of the spectrometer. Two 90 off-axis parabolic (OAP) mirrors of 4 reflected focal length were used to collimate and focus light from the probe volume on the spectrometer slit. The optical alignment was first done using a fiber coupled 502 nm LED at the probe volume. Once the LED was focused to a tight spot on the spectrometer slit, the lab jack and motorized translation stage were used to raise and translate the spectrometer in order to optimize the dispersed LED signal on the streak tube/CCD assembly in focus mode. Once the signal was optimized, the LED coordinates at the probe volume was marked by making a cross with a He-Ne laser. The LED was then replaced by the electrodes used to create plasma. It was observed that the collection efficiency from plasma emission was very sensitive to the electrodes coordinates relative to the LED fiber tip. The spatial resolution of the probe volume



OAP : Off-Axis Parabolic Mirror , CCO: Camera Coupling Optics , IO: Input Optics, DS: Dispersed Signal, ML: Motorized Stage on a Labjack, TR2: 2D Translation Stage, PPE: Pin to Pin Electrodes, HN : HeNe Alignment Laser, NRP: NRP Pulser

Fig. 4.3.: Schematic of the experimental system for streak-OES of NRP plasma discharges [60]

can be controlled by varying the slit opening of the spectrometer. Depending on spectrometer slit opening, the experiment can be used for lifetime measurement or quantitative spectroscopy. The temporal resolution of the streak camera corresponds to the number of horizontal rows exposed on the camera by the slit of the streak camera. For the measurements reported in this manuscript the slit of the streak camera was fixed at 30 m. This corresponded to 4 horizontal rows on the CCD camera.

For both direct imaging and optical emission spectroscopy, an Eagle Harbor 3300-20-F high voltage pulser was used to generate the plasma. The pulser can generate pulses with duration ranging from 20-110 ns, pulse repetition frequency of 1-400 kHz and peak pulse voltage from 1-30 kV. For the experiment on direct imaging using streak camera, single plasma pulse was generated using the pulser. While for the

experiment on optical emission spectroscopy, a pulse repetition frequency from 5 to 100 kHz was used.

4.3.2 Timing and Trigger System(excluded part of psst paper)

The streak camera has three modes of operation and gate mode is preferred when background noise needs to be eliminated. In the gate mode, the camera requires two triggers: one to open the camera gate and the other to start the streak sweep. The two triggers were supplied using Channels A and B on the delay generator separated by $1 \mu\text{s}$ as recommended in the camera manual. There is an internal delay (τ_{int}) between when the camera receives the streak trigger and when it actually starts the sweep. Each streak speed has a different internal delay, which is provided in the camera manual. The goal of the experiment is to capture the plasma emission within the streak sweep window (τ_{streak}), so ideally Channel C should be set to Channel B + τ_{int} . However, there are additional delays associated with the internal circuits in the waveform generator, the BNC cable length, jitter of high voltage pulser and the time between voltage rise and plasma emission. The total time delay from when Channel C triggered the waveform generator to the start of plasma emission, τ_{plasma} was actually longer than the internal delay of the camera, τ_{int} . Therefore, the delay of Channel C with respect to Channel B was adjusted to match the difference between τ_{plasma} and τ_{int} . While the delays associated with the waveform generator and BNC cables are fixed, the high-voltage pulser jitter is variable and causes τ_{plasma} to vary from shot to shot, making it very difficult to capture the plasma emission at a particular time step. One significant advantage of the current technique is that as long as the voltage pulse lies within the streak sweep window, the complete plasma emission spectrum was acquired; hence the spectral data acquired is jitter free. Channel D from the delay generator was set equal to Channel B and recorded on the oscilloscope along with voltage and current. A sample voltage and current trace are shown in Figure 2 along with overall timing and trigger diagram.

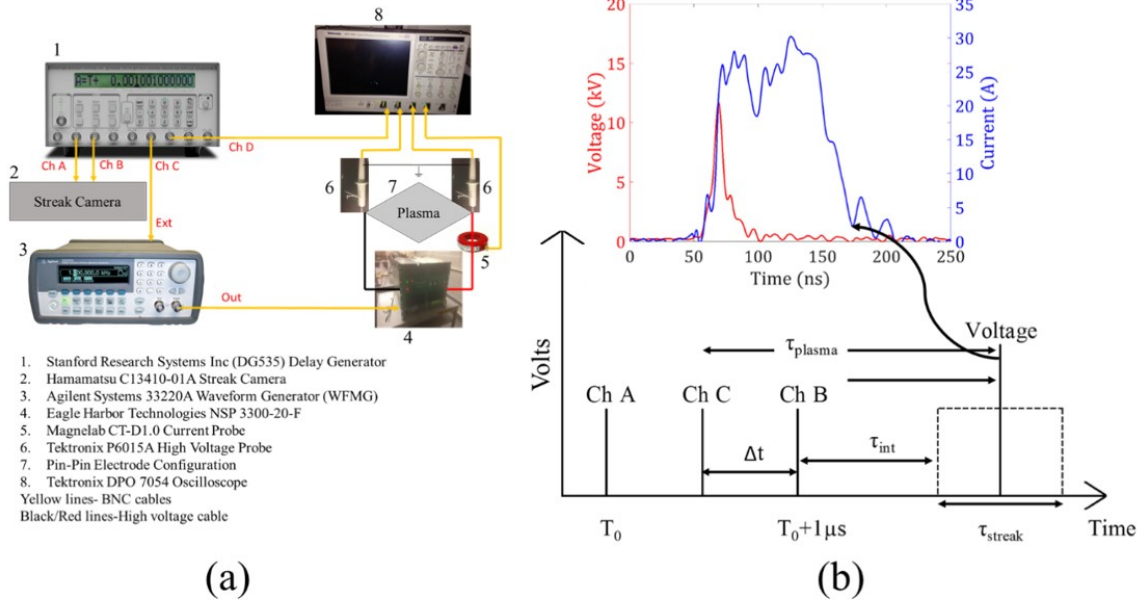


Fig. 4.4.: Schematic of the experimental system for streak-OES of NRP plasma discharges [61]

4.3.3 Results

4.4 Characterization of the Streak Camera System With CW LED Light

The first step in any optical system is to understand its performance with a known light source such as a laser or a light emitting diode of known wavelength. The streak camera system consists of an intensifier that provides signal gain and high speed gating. The presence of intensifier adds intensifier noise to the overall image and this is different from readout noise since it appears only when a photon hits the multi-channel plate. So increasing the gain on the streak tube increases the signal level but also increases the intensifier noise. After a certain gain level is reached on the streak camera, the advantage of an intensifier would diminish. In order to test this, the camera is used to image a light source and the signal to noise ratio is plotted as a function of intensifier gain. As the gain is increased, the signal to noise ratio

would drop at some point, providing the gain limit of the intensifier. In the case of a streak camera, since the image recorded is one-dimensional and varying in time, a light source which is constant in time needs to be used. For the current experiment, a light emitting diode centered at 502nm is dispersed through a spectrometer and imaged on the streak camera with a streak sweep time of 500 μs . Since the light source has a constant intensity in time, the dispersed streak image should ideally be constant in time. The line spectra of the LED at different time instants should overlap since its a constant intensity light source, however there could be some stray fluctuations in the signal while the streak sweep is applied. The mean of signal intensity of streaked image is estimated along with the standard deviation and the ratio of the two would provide information of the extent of deviation of the signal from its mean value. As the intensifier gain is increased, the mean signal intensity will increase, if the standard deviation stays constant then the ratio of the two would keep increasing and therefore allowing operation at any intensifier gain setting. If the standard deviation grows faster than the mean signal level, then at a certain gain level the ratio would begin to drop, providing an optimal gain setting on the camera.

The streak camera used in the current work can operate with an intensifier gain ranging from 1-63, so to characterize the system with the LED the camera was operated with a gain of 20, 30, 40 and 50. The input slit of the camera was kept at 30 μm , same as the slit width used for the experiment. The streak image for the different intensifier gain setting is shown in Figure 4.5. From the streak image it can be observed that the intensity counts increase from 70 to 2500 as the gain is increased from 20 to 50. The mean signal, standard deviation and the ratio of standard deviation and mean signal is plotted as a function of intensifier gain in Figure 4.6. From the ratio of mean signal counts and standard deviation it can be observed that the ratio increases and starts to drop rapidly beyond a gain of 40. Having an intensifier gain beyond 40 will start to increase intensifier noise on the camera so the streak camera system for the current work was operated with an intensifier gain of 40 for most cases.

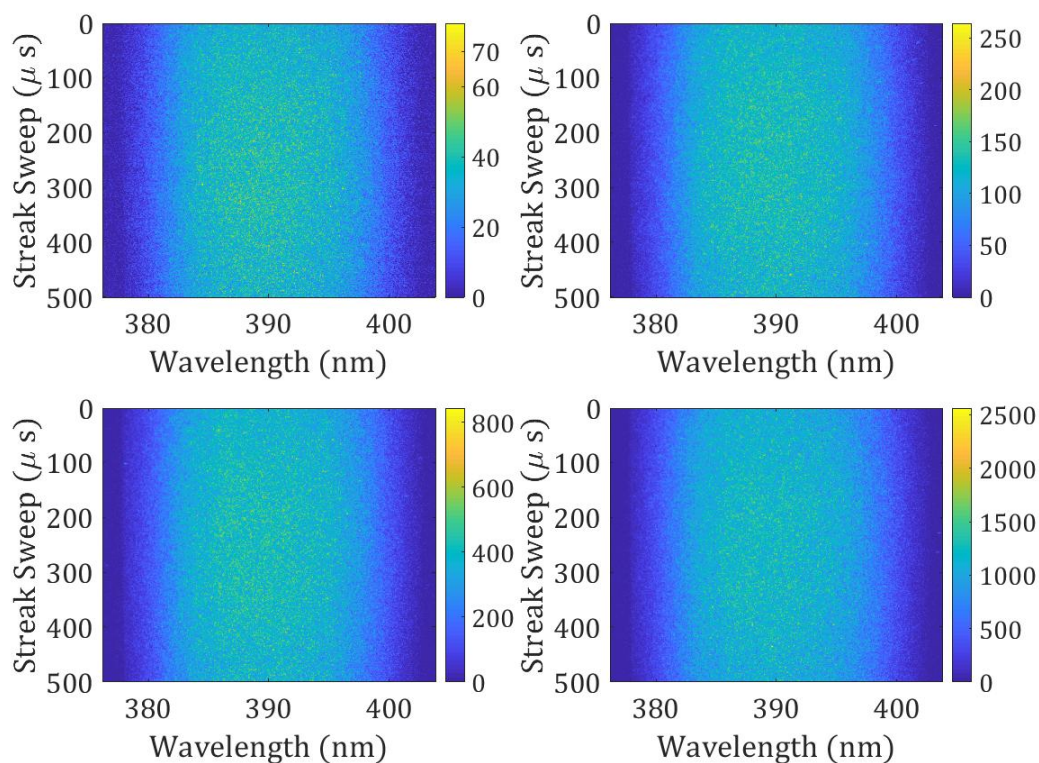
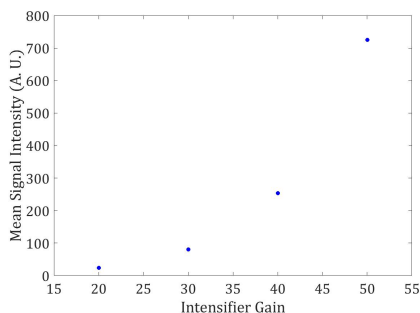


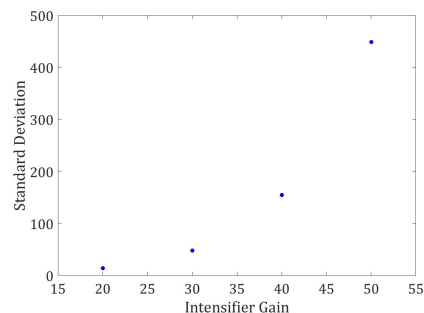
Fig. 4.5.: Streak image of a constant intensity Light Emitting Diode (LED) at intensifier gain setting of 20, 30, 40 and 50

4.5 Time Resolved Imaging of Plasma Luminescence using Streak Camera

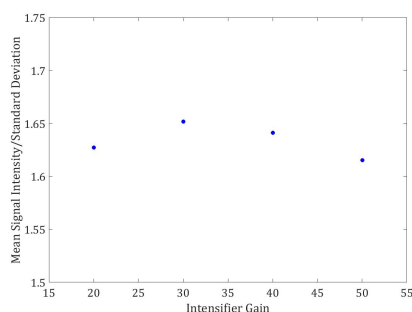
For all the experiments on time resolved imaging, the plasma discharge was created for a pin-pin electrode with electrode gaps ranging from 1 to 3 mm. The plasma was generated using the Eagle Harbor Technologies high voltage pulser with a pulse duration ranging from 35-100 ns and a pulse voltage of 25 kV for this particular experiment and only a single plasma pulse is created instead of repetitive pulsing. The effect of electrode gap, pulse voltage and pulse duration is investigated in this



(a) Mean signal level at different intensifier gain setting



(b) Standard deviation of the signal at different intensifier gain setting



(c) Ratio of standard deviation and mean signal level at different intensifier gain setting

Fig. 4.6.: Characterization of the Streak Camera System

work. The following sections will show results of variation of electrode gap, pulse duration and pulse voltage.

4.5.1 Effect of Electrode Gap

The streak image for the two electrode gaps is shown below in Figure 4.7 and Figure 4.8. The x-axis on the image represents spatial dimension while the Y-axis represents time. The image intensity is binned along the spatial direction and plotted as a function of time to show the rise and decay of emission intensity. The intensity as a function of time is plotted as blue line alongside the voltage and current which are

recorded for the particular streak image. The intensity profile resembles the current waveform. For both the 3 mm and 1 mm electrode gap, the plasma luminescence looks similar. The streaked image of the plasma discharge indicates 3 distinct phases. In the first phase the plasma emission is very high and develops and decays extremely rapidly. There is a second dimmer phase which begins to rise when the first phase has decayed by approximately 80 percent. The second phase is characterized by a slower emission decay. Therefore, the emission curve over the first few nanoseconds exhibits a bi-exponential decay behavior. The second phase is followed by a period where there is no emission at the center of the electrode gap, while emission starts from the electrode tips and propagates towards the center, leading into phase 3. The phase 3 emission persists for a much longer time than the emission of phases 1 and 2. The time scale of phases 1 and 2 is similar to the time scale of decay of the nitrogen second positive system. However phase 3 is considerably long, on the order of 100 ns and further investigation is needed to understand the excited species that are emitting photons during phase 3.

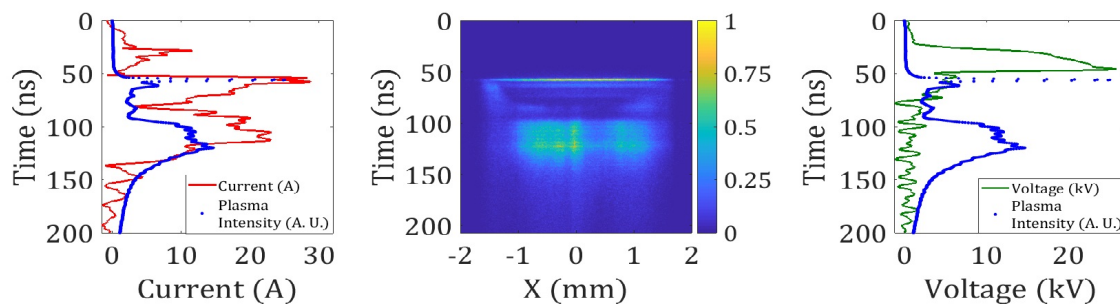


Fig. 4.7.: Streak camera imaging of a pin to pin single plasma discharge with 3 mm electrode gap, 25 kV breakdown voltage and 100 ns pulse duration

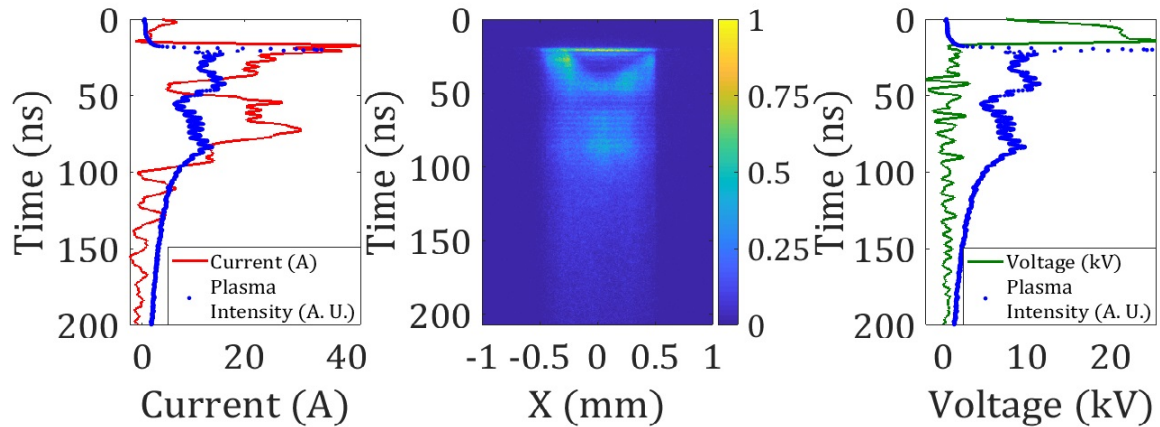


Fig. 4.8.: Streak camera imaging of a pin to pin single plasma discharge with 1 mm electrode gap, 25 kV breakdown voltage and 100 ns pulse duration

4.5.2 Effect of Pulse Width

In order to study the effect of pulse duration, the plasma was generated with pulse duration ranging from 35 ns to 100 ns, the pulse breakdown voltage was still maintained at 25 kV. The streak images for the different pulse durations are shown in Figures 4.9-4.12. It is interesting to note that as the pulse duration is decreased from 100 ns to 35 ns, the emission in phase 3 begins to disappear. The same can be observed even in the current profile where the width of the current decreases with pulse duration. Having an overlay of current and emission profile, it can be observed that the emission profile follows the current and phase 3 emission happens during the second peak of the current. The second peak in the current profile could be due to impedance mismatch between the electrode and the pulser causing internal pulser reflection. However, the internal reflection is causing bright plasma emission from some species which needs to be further investigated through use of optical filters and streak camera. This plasma emission during phase 3 for longer pulse durations is changing the dynamics of plasma discharge like contribution to gas heating and

other oxidation reactions. This effect at longer pulse durations must be carefully investigated in future work.

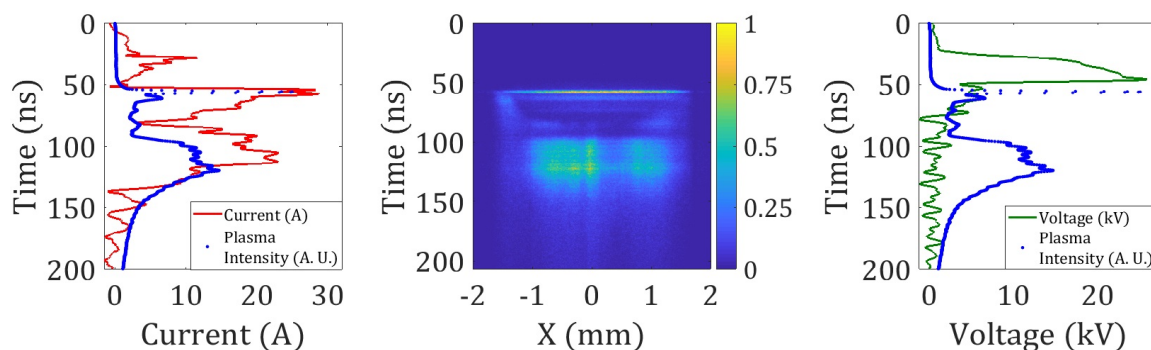


Fig. 4.9.: Streak camera imaging of a pin to pin single plasma discharge with 3 mm electrode gap, 25 kV breakdown voltage and 100 ns pulse duration

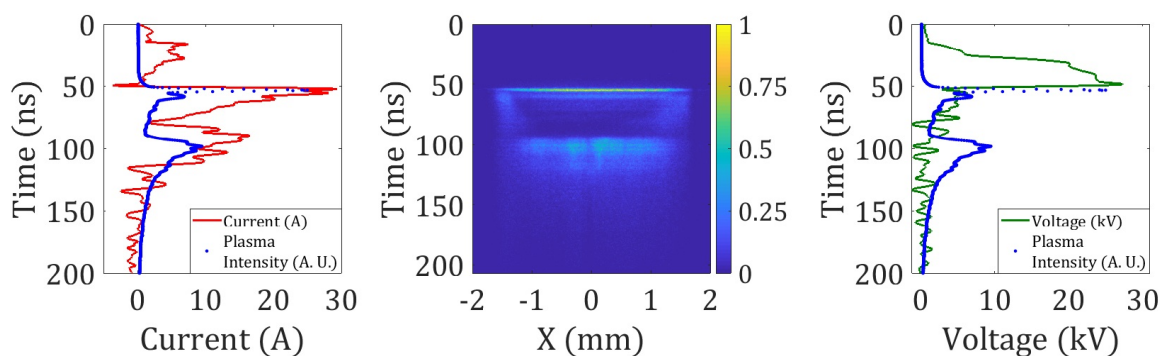


Fig. 4.10.: Streak camera imaging of a pin to pin single plasma discharge with 3 mm electrode gap, 25 kV breakdown voltage and 75 ns pulse duration

4.5.3 Effect of Pulse Voltage

In this section the input voltage on the pulser is lowered to investigate the effect of breakdown voltage on plasma emission. The supply voltage was lowered to 17.5

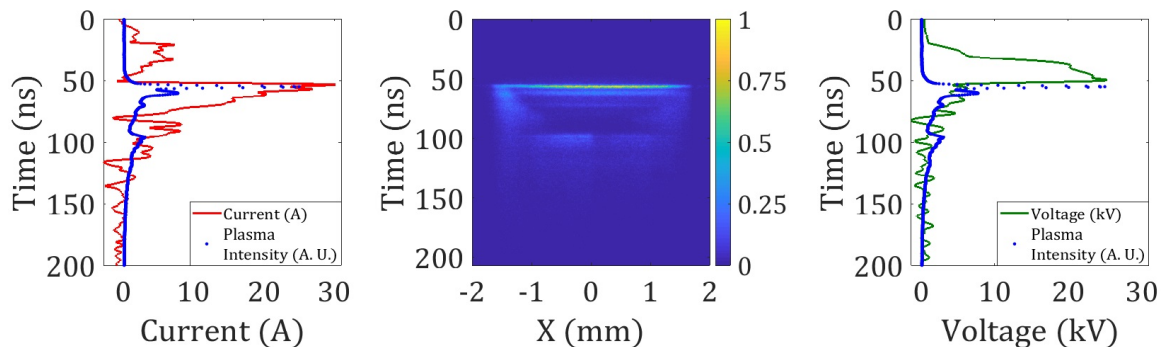


Fig. 4.11.: Streak camera imaging of a pin to pin single plasma discharge with 3 mm electrode gap, 25 kV breakdown voltage and 50 ns pulse duration

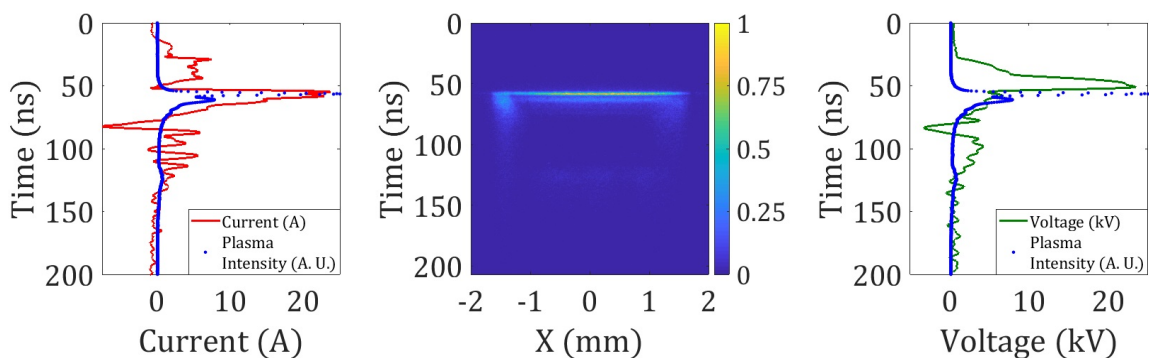


Fig. 4.12.: Streak camera imaging of a pin to pin single plasma discharge with 3 mm electrode gap, 25 kV breakdown voltage and 35 ns pulse duration

kV from 25 kV and the pulse duration was still maintained at 100 ns. The streak image along with current and voltage is shown below in Figure 4.13. Comparing the plasma emission from 17.5 and 25 kV, with the same pulse duration, there seems to be little effect from change in pulse voltage. The first part of the emission is bright, followed by a dark region and then a reappearance of the glow. The current waveform also has the same shape as that with 25 kV breakdown voltage, with the presence of a second peak. The intensity profile matches the current profile.

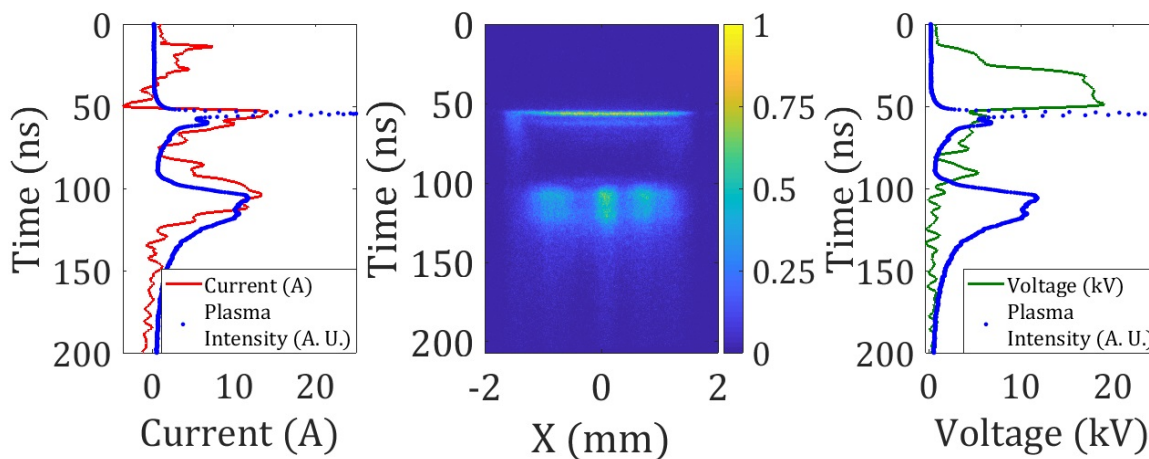


Fig. 4.13.: Streak camera imaging of a pin to pin single plasma discharge with 3 mm electrode gap, 17.5 kV breakdown voltage and 100 ns pulse duration

4.6 Time Resolved Optical Emission Spectroscopy for Lifetime and Temperature Measurements

4.6.1 Lifetime Measurements of Excited Nitrogen Created from Plasma Discharge

The experimental system for optical emission spectroscopy was used to measure emission from the nitrogen second positive system. The streak camera slit was $30 \mu\text{m}$ and spectrometer slit was 1 mm which is equal to the electrode gap width. Plasma discharges were generated in a 1 mm electrode gap with the same supply voltage and pulse duration as in the experiments discussed in the previous section, but were pulsed at a frequency of 5 kHz. The number of pulses in the burst was maintained at 50 to produce a total discharge time of 10 ms, and all streak sweeps were performed on a single discharge 6 ms into the pulse burst. The burst was repeated every 10 s and the streak sweep measurement was performed on exactly the same pulse for every burst. Since there was jitter in the pulser output, the emission appeared at different regions on the streak camera sensor. Emission of the (0-0) vibrational band of the second

positive system of nitrogen was captured in these streaks by tuning the spectrometer center wavelength to 337 nm with a grating of 1200 gr/mm. The species decay time is inferred from the measurements by summing the pixel intensity along the wavelength direction to provide total intensity at each time instant and emission is then be plotted as a function of time. The use of the streak camera to make a decay measurement is much faster than a traditional PMT-type measurement and also ultimately jitter-free since a streak image picks up the entire emission from a single plasma discharge. Figure shows a background corrected streak image of a single plasma discharge within the 5 kHz pulse burst. The camera was streaked at 100 ns with a temporal resolution less than 400 ps. The emission of N2(C) decayed completely within 15 ns, with two distinct phases with different decay rates, indicating a bi-exponential nature to the decay. In the first phase, which extends from approximately 10 ns to 12.5 ns, the N2(C) emission decays rapidly and was fit with an exponential with $R^2=0.98$ and $1/e$ time of 2.14 ns. The second phase starts at 13 ns and the during this phase the emission decays slowly compared to the first phase and was fit with an exponential curve with $R^2=0.96$ and $1/e$ time of 7.14 ns.

4.6.2 Ultrafast Heating from the Plasma Discharge

To perform quantitative spectroscopy, the spectrometer slit was closed down to improve spectral/spatial resolution. The experiment reported in Figure 4.4 is now performed with a spectrometer slit width of 100 μm . The plasma was pulsed at 5, 20 and 50 kHz with varying number of pulses in the pulse burst providing 10 ms of discharge time. The spectrum of a single discharge, 6 ms into within the burst, was collected with a streak sweep of 100 ns. The burst was repeated every 10 s and spectra were continuously collected. The collected spectra for roughly 500 streak images were accumulated during post-processing after accounting for pulse jitter. The accumulated spectrum for pulse repetition frequency of 5 kHz is shown in Figure 4.14(a). The accumulated streak spectrum provides time-resolved information on the

production and decay of the nitrogen second positive system; a slice along the time axis provides spectral information at that particular time instant. To infer the temperature, a sliced spectrum from Figure 4.14(a) was obtained by binning 4 pixels along the time axis and imported into the spectral fitting software Specair [62, 63]. The software was used to obtain fits for rotational and vibrational temperature as shown in Figure 4.14(b-d). The spectral fits indicate that the plasma pulse heats the surrounding air by close to 500 K in a few nanoseconds and the results are close to the gas heating obtained by Tholin et. al. in their numerical simulations [64]. The time resolved rotational and vibrational temperatures for a PRF of 5, 20 and 50 kHz are shown in Figure 4.15 and 4.16 respectively. The time resolved rotational temperature shows that the degree of ultrafast heating is about 400 Kelvin for most PRFs. The rotational temperature equilibrates with translational temperature quickly, so the gas temperature is assumed to be equal to rotational temperature. As the pulse repetition frequency is increased, the starting temperature of the pulse is hotter, which indicates that the gas has not had sufficient time to cool down to 300 Kelvin before the subsequent pulse in the train arrives at the electrode gap. The time resolved vibrational temperature indicates that the vibrational temperature is lower at higher pulse repetition frequencies. This could be because of lower energy deposited per pulse at higher pulse repetition frequency. The trend for time resolved vibrational temperature is interesting that it drops initially and then begins to rise again. This is the first time that vibrational temperature is measured to such high temporal resolution and there is no computational simulations to compare with, so more measurements needs to be made in order to confirm the findings without any uncertainty. This seems to be an interesting phenomenon and needs to be investigated further. The rotational and vibrational temperatures shown here are only preliminary results from the streak-spectroscopy system. More experiments need to be performed to confirm these findings and also report uncertainty on these measurements. At high pulse repetition frequency the signal level is low so more accumulations will be needed to remove any fluctuations in the measured temperature.

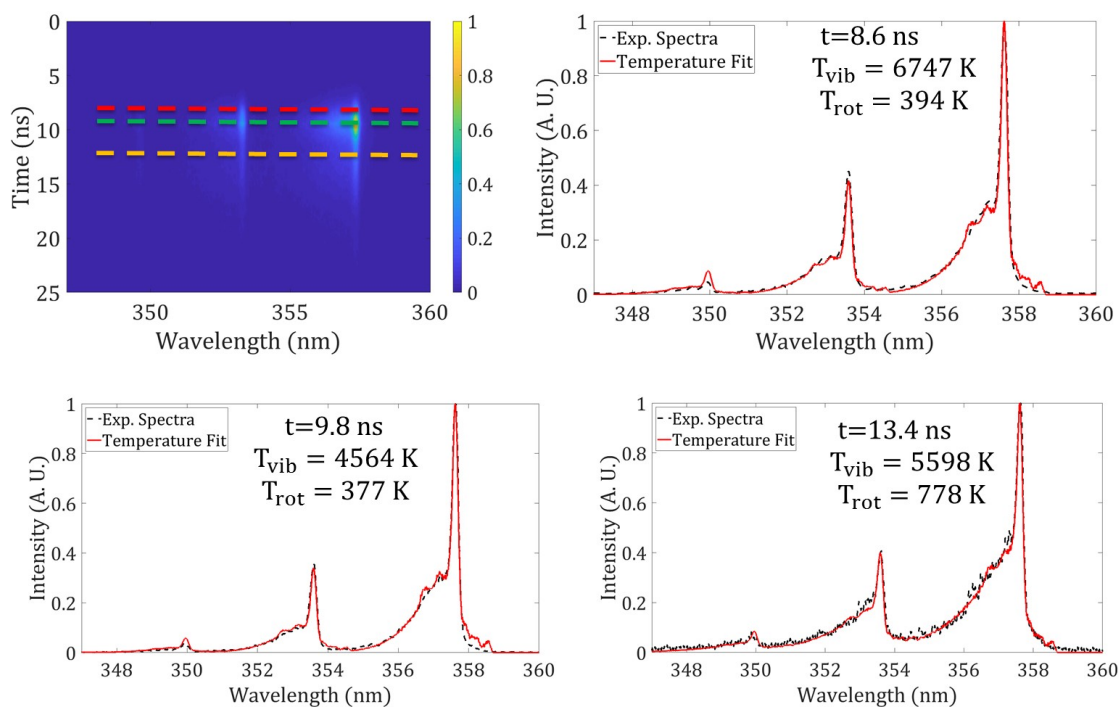


Fig. 4.14.: Accumulated streak spectrum of a single plasma pulse with temperature fits at $t = 8.6, 9.8,$ and 13.4 ns

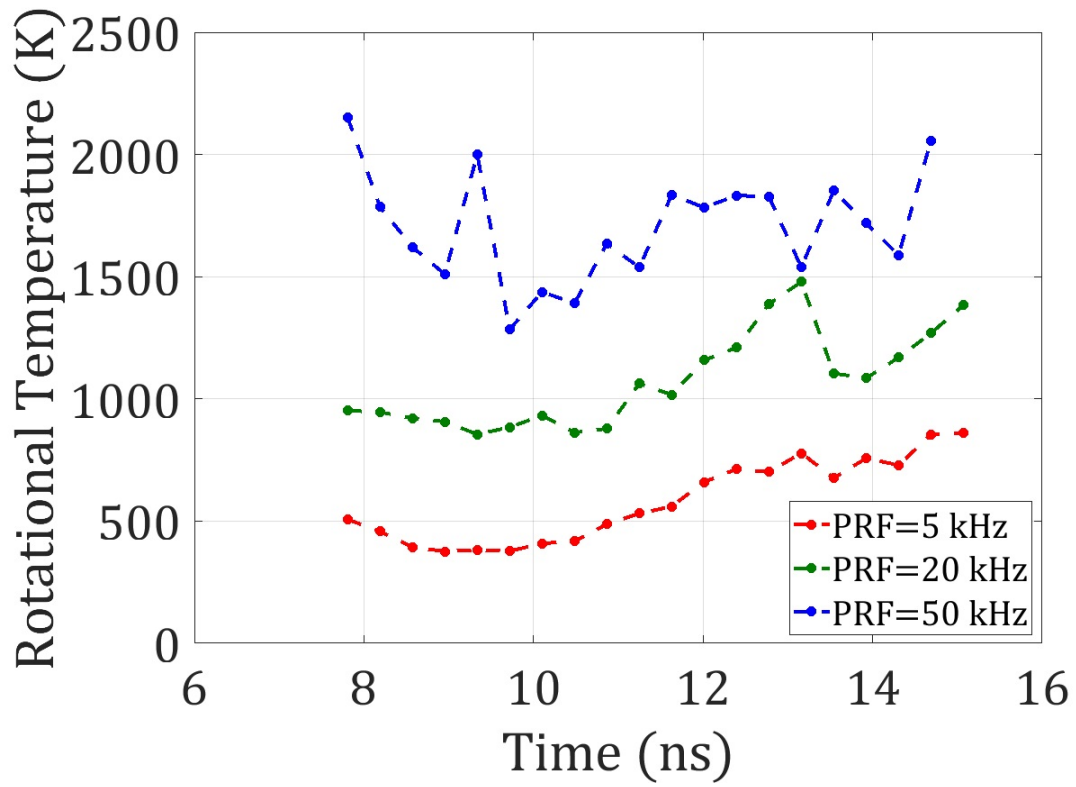


Fig. 4.15.: Time resolved rotational temperature at PRF of 5, 20 and 50 kHz for pin-to-pin electrode with 1 mm electrode gap

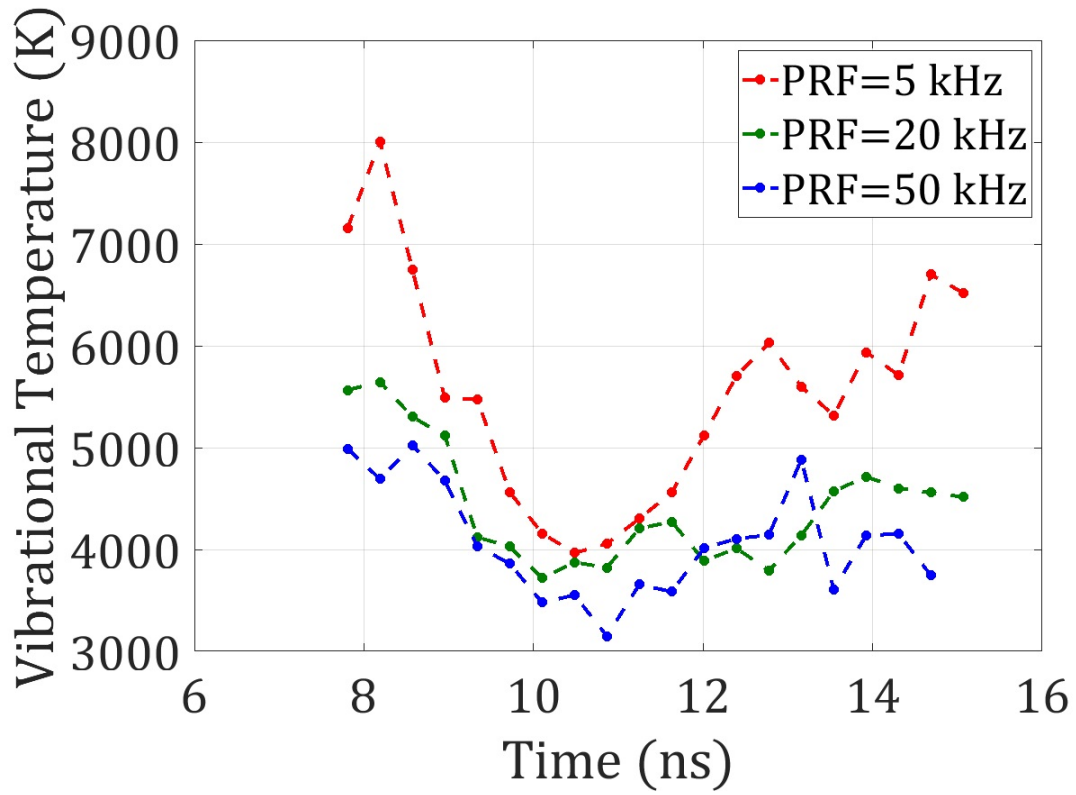


Fig. 4.16.: Time resolved vibrational temperature at PRF of 5, 20 and 50 kHz for pin-to-pin electrode with 1 mm electrode gap

5. DEMONSTRATION OF PLASMA ASSISTED IGNITION INSIDE CONSTANT VOLUME VESSEL

5.1 Literature review

As discussed in the first part of the thesis, the wave rotor can support internal combustion. The main challenge is to get the fuel air mixture across the length of the channel and to ignite this mixture quickly before the exhaust port opens. In the current wave rotor design, ignition is achieved using a turbulent hot jet that penetrates into the wave rotor channel. In this thesis, an alternate ignition mechanism using pulsed plasma discharges is investigated. The plasma assisted ignition (PAI) approach is investigated in a constant volume vessel using an electrode geometry similar to what might be used in the wave rotor in future designs.

There has been tremendous progress in the area of plasma assisted ignition (PAI) and combustion (PAC) over the past 10 to 15 years. Research has shown that using plasma discharges in combustion can modify transport processes through new reaction pathways such as O atom production from collisions of electrons, ions and oxygen molecules which can then modify fuel oxidation reactions [2]. Kimura *et.al.* were the first to use plasma discharges in supersonic combustion [65] where, a plasma jet was used to ignite hydrogen in supersonic crossflow. Following this groundbreaking work, there have been further efforts on PAC in supersonic combustion using a variety of plasmas, including plasma torches, [66–71], filamentary plasma discharges [72, 73], microwave discharges [74] and nanosecond pulsed discharges [75]. Plasma discharges have been used to enhance ignition, flame stabilization, and fuel/air mixing in gas turbine and internal combustion engines, as well as to extend the lower lean blowout limit and lean flammability limit.

In general, plasmas can be categorized as equilibrium or non-equilibrium. In the case of equilibrium plasma such as spark plugs, the electronic, vibrational and rotational temperatures are in equilibrium and the gas temperature and electron number density are very high. In the case of non-equilibrium plasma, the electronic, vibrational and rotational temperatures are different and the neutral gas temperature and electron number density are relatively low. Microwave discharges, dielectric barrier discharges (DBDs), streamers and glow discharges are examples of non-equilibrium plasmas. In these plasmas, the electronic temperature is extremely high, on the order of 100 eV, and thus these plasmas are highly efficient at production of excited species and active radicals through electron impact dissociation, excitation and energy relaxation [76]. Generally for ignition, a spark discharge is preferred. A spark discharge is a good conductor with high electrical current. If this high current is sustained for time scales on the order of a few microseconds, then the spark transforms to an arc with high neutral gas temperature and electron number density, but low electron temperature. If the spark current is cut off within a few tens or hundreds of nanoseconds, then only the electron temperature is increased. The energy distributions in these nanosecond-duration pulsed discharges are non-Boltzmann. In the different plasma discharges, the rate at which energy is transferred between different excited electronic levels are different. Rotational energy levels equilibrate with translational levels faster than vibrational and electronic levels. Vibrational-translational relaxation requires about $10^3 - 10^8$ collisions [77]. The desired characteristics of the plasma discharge is dependent on the combustion timescale. For example, For high speed combustion, excitation of rotational levels is important because energy transfer to the translational levels occurs much faster.

Plasma discharges interact with the combustion environment through thermal, kinetic and hydrodynamic pathways. In the case of the thermal mechanism, the plasma discharge produces ultrafast heating of the surrounding gas on a nanosecond time scale which will then lead to acceleration of chemical reactions. In the kinetic pathway, the high electronic temperature of non-equilibrium plasma leads to electron

impact dissociation, which can generate active radicals and reaction catalysts that promote low temperature fuel oxidation. In the hydrodynamic pathway, the plasma can induce local flow fields through the generation of ionic wind. Additionally, the steep thermal gradients in the vicinity of the plasma produce pressure waves and fluid instabilities, leading to vorticity generation and mixing. The three pathways for plasma-combustion interaction are generally coupled and therefore it is difficult to understand the main mechanism of plasma enhancement. In the current work, the individual pathways are not isolated and studied individually, but rather the overall plasma enhancement is investigated to assess the applicability of plasma assisted ignition for wave rotor combustion.

Several studies have demonstrated the use of plasma discharge has reduced ignition delays for a range of fuels such as hydrogen and hydrocarbons and this improvement is attributed to enhancement of radicals driving the high temperature chain branching reaction [78–80]. However, the degree of enhancement is dependent on the type of fuel. For practical applications such as gas turbine and internal combustion engines, it is important to understand how plasma discharges alter combustion chemistry in alkanes. A hydrocarbon fuel undergoes oxidation during combustion and is dependent on temperature and pressure. The entire ignition process occurs through a chain of reactions, some occurring at high temperature and some at low temperature. The high temperature reactions involve oxygen molecule reacting with atomic hydrogen to form OH and atomic oxygen. The low temperature reaction involves oxygen molecule reacting with alkyl radical to form alkylperoxy radicals. The reaction rate decreases with increase in temperature through a phenomenon called negative temperature coefficient.

Based on experiments by Tsolas et. al. [81] who performed ignition tests for C1-C7 alkanes, a significant effect of plasma is observed for all the alkanes tested. Without the plasma discharge Tsolas et. al. observed the onset of fuel consumption to occur at temperatures greater than 900 K as shown in Figure 5.1(a). But when the plasma discharge is used for ignition, the low temperature decomposition of the fuel was

enhanced. Plasma discharge also lowers the temperature for complete consumption of fuel. They observed that for C_2 and smaller fuels, the fuel consumption rate is slow initially and then transitions to faster rate at temperature greater than 900 K. For larger fuels, the reaction is fast initially but transitions to slower rate at higher temperature as shown in Figure 5.1(b). For larger fuel molecules, a negative temperature coefficient was observed between 670 and 870 Kelvin, indicating change in chain branching. At temperatures higher than what is required for fuel consumption, thermal branching starts to dominate and plasma enhancement diminishes. Only in the case of Methane, plasma enhancement can be observed at higher temperatures. For almost all fuels, it is found that plasma can accelerate the high temperature chemistry at much lower temperatures [81]. In some larger fuels greater than C_3 , there were multiple transitions in the overall reaction rate [81].

To provide context for the current work, a brief overview of relevant prior work on PAI and PAC in high-speed flow is necessary. Matsubara *et.al.* used a combination of plasma torch and dielectric barrier discharge for supersonic combustion [82]. They found that the dielectric barrier discharge produces radicals at the recirculation zone of their backward facing step. They also showed that ignition was possible with just the use of a dielectric barrier discharge. They concluded that the plasma thermal effect is needed to stabilize the flame in high speed flow and the plasma kinetic effect can only enhance flame stabilization near its stabilization limit. Do *et.al.* used nanosecond repetitively pulsed discharges with 15 kV peak voltage, 20 ns pulse width and 50 kHz pulse repetition rate for ignition of hydrogen and ethylene in supersonic crossflow with Mach number between 1.7 and 3. They found that flame stability was enhanced in the presence of the plasma discharge [75]. They concluded that the addition of atomic H and atomic O through electron impact dissociation leads to shorter ignition delay time. Leonov *et.al.* used multiple electrode, quasi-DC discharges behind a backward step cavity in hydrogen and ethylene mixtures [83]. They concluded that the flame could exist only in the presence of plasma. They postulated a two zone model of combustion due to the plasma discharge. In zone 1, there is cold combustion

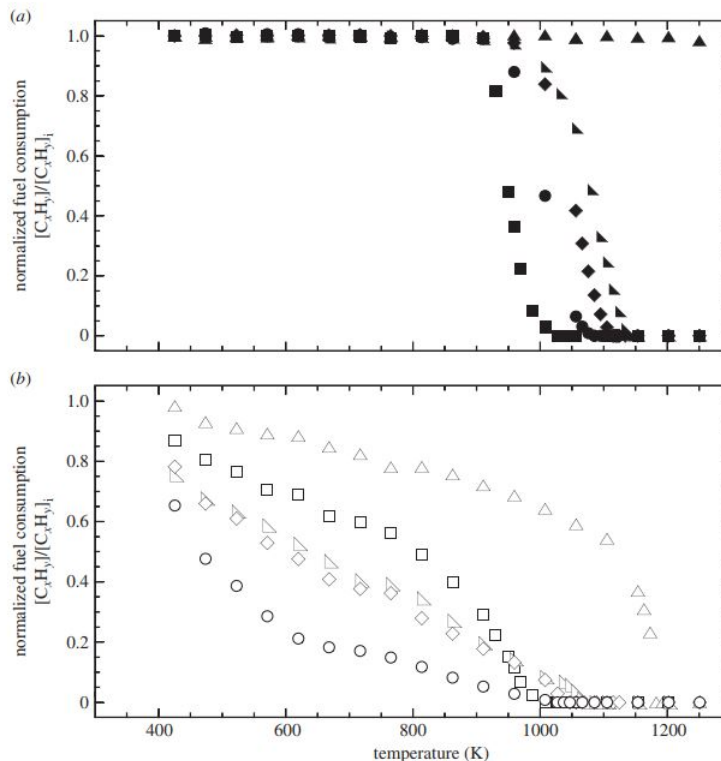


Fig. 5.1.: Fuel consumption for different fuels as a function of temperature (a) with plasma and (b) without plasma. CH_4 (triangle), C_2H_6 (square), C_3H_8 (right angle triangle), C_4H_{10} (diamond), C_7H_{16} (circle)

accompanied by plasma-induced fuel conversion with minimal heat release. In zone 2, where there is complete combustion, there is high energy release. Esakov *et.al.* used microwave-assisted combustion of propane air in supersonic flow. They found that a deeply undercritical microwave discharge where the input electric field is lower than the electric field required to create electrode less breakdown, can improve combustion efficiency in cold supersonic flow. These experiments have shown that, in high speed flow ,it is difficult to achieve combustion enhancement using the plasma non-thermal effect alone, rather a combination of thermal and non-thermal effects is required.

Plasma discharges have been used extensively in internal combustion engines, gas turbine engines and constant volume combustion devices such as pulse detonation

engines [84–94]. Wolk *et.al.* used microwave-assisted spark ignition of methane-air mixture in a constant volume combustion chamber to show improvements in lean and rich ignition limits from 1 to 7 bar. They observed enhancement of flame development time which is the time required for 0 to 10 percent of total heat release and no enhancement of flame rise time which is the time required for 10 to 90 percent of heat release. Based on these results, they concluded that plasma discharges can initiate ignition but cannot help in increasing flame speed with microwave-assisted spark ignition of methane-air mixtures in a constant volume combustion chamber. The Gunderson research group at University of Southern California have developed several transient plasma igniters for gasoline engines [86–88]. The transient plasma was generated using 20-85 ns pulse duration and pulse energy of close to 60 mJ, compared to a traditional spark igniter with a pulse duration and energy of 2 ms 80 mJ, respectively. The transient plasma creates a distributed array of streamers which produce a larger volume of active radicals. Cathey *et.al.* used a transient plasma with 70 ns pulse duration, 60 kV peak voltage and 800 mJ pulse energy for ignition of a methane/air mixture. They found that the OH production from the plasma decayed within 1 μs while ignition started at 1 ms, showing that production of OH in the volume is not entirely responsible for ignition. These results suggested that the plasma thermal effects play a role in ignition in addition to the kinetic effect.

The same research group has collaborated with the Naval Postgraduate School on using plasma discharges for ignition pulse detonation engines (PDEs) [95]. They demonstrated that at high mass flow rates where spark discharges could not initiate a flame, a transient plasma was able to ignite the mixture effectively and trigger a detonation.

These prior efforts have shown the effectiveness of using plasma discharges for ignition and flame enhancement in a variety of combustion systems and that the effect from the plasma is both thermal and nonthermal. In the current work, PAI using nanosecond repetitively pulsed discharges will be examined in a novel electrode

geometry similar to Gunderson's group at USC to assess its potential for ignition in a wave rotor channel at high rotation speeds.

5.2 Experimental System

The plasma-assisted ignition experiment is conducted in a constant volume vessel made from steel. The vessel has a 3.5" x 3.5" square cross-section with 0.5 inch thick walls and a height of 10 inches. The dimensions provide roughly 2 liters in internal volume. A stoichiometric mixture of methane and air is used for the experiment. The reacting mixture is filled remotely using LabVIEW and the desired mixture ratio is obtained using the method of partial pressures. The gas mixture is introduced into the vessel through a series of pneumatic and hand valves. At the start of the experiment, pneumatic valves 4 and 5 are opened and closed to evacuate and create vacuum inside the vessel. The hand valves are opened to meter the flow and pneumatic valves 1, 2 or 3 are opened depending on the gas introduced into the vessel. This will fill the line with the desired gas until pneumatic valve 5. The vessel is filled with the desired gas by opening pneumatic valve 5. Once the vessel is filled with the desired gas up to a certain pressure, pneumatic valve 5 is closed and pneumatic valve 4 is opened to evacuate any residual gas in the fill line. This is followed by a cycle of filling the gas lines with nitrogen and opening the vacuum pump again to ensure any residual gas is eliminated. The same process is carried out for the three gases and once the vessel is filled to the desired equivalence ratio, the mixture is ignited. Once the ignition is complete, pneumatic valve 4 and 5 are opened to evacuate any residual gas from the vessel. This is followed by a cycle of nitrogen fill and use of vacuum pump to ensure the vessel has no residual reacting mixture. A schematic of the plumbing diagram is shown in Figure 5.2. The vessel used for ignition experiment is shown in Figure 5.3. The electrodes are mounted inside the vessel using an insulating fixture and a high voltage, high pressure electrical feed through is used to connect the electrodes to the high voltage power supply. The propagation of the flame is visualized using

high speed schlieren and background oriented schlieren (BOS). The optical layout is shown in Figure 5.4. For schlieren, a high power led is used as light source. The led is placed at the focal length of the concave mirror, which will collimate the light from led. The collimated light passes through the test section and a second concave mirror forms an image of the led at its focal length. The knife edge is placed at this image point, providing a cutoff. The high speed camera is placed behind the knife edge to focus on the test section. The frame rate of the camera for this experiment is set to 20000 frames per second. For background oriented schlieren a dot pattern is placed on the window of the vessel. An arc lamp is used to illuminate the dot pattern. Another high speed camera is used to visualize light from the dot pattern. When there is density gradient in the test section, the light rays from these dots are bent in the direction of increasing density and the dot pattern is shifted with respect to the reference image on the camera. This shift in dot pattern is proportional to the gradient in density. Background oriented schlieren under certain circumstances can be used to obtain density in the flow field. The electrodes for this experiment is machined from stainless steel and ceriated tungsten. The pin electrode which is ceriated tungsten is 0.125 inches in diameter and is sharpened using a grind wheel. The ring electrode is machined from stainless steel and is 1 inch in diameter. Both electrodes are held in a fixture machined from acrylic. The plasma was generated using the Eagle Harbor 3300-20-F power supply that can generate nanosecond high voltage pulses ranging from 20 to 110 ns, voltage of 1-25 kV and pulse repetition frequency of 1-400 kHz. The filling of gas into the pressure vessel is done using the method of partial pressures. The gas used for the current experiment is methane and synthetic air, the equivalence ratio for all the tests is 1 and the total pressure for all experiments is 1 atmosphere. The chemical reaction for stoichiometric combustion of methane is



From the chemical reaction, the mole fraction for methane, oxygen and nitrogen are 0.095, 0.19 and 0.72. The partial pressure for each gas is mole fraction multiplied by

the total pressure. The partial pressure for methane, oxygen and nitrogen is calculated to be 1.40 psia, 2.79 psia and 10.58 psia respectively. Since the fuel pressure is the lowest, it is filled first after the vessel is evacuated to vacuum. The fuel is followed by an inert gas which in this case is nitrogen. The inert gas is filled second so that the mixture is not combusted by mistake. Oxygen is filled last to make up the total pressure of 14.7 psia. In between filling of each gas the gas lines are evacuated using the vacuum pump so we don't mix the different gases inside the gas lines. Once the gas mixture is filled in the vessel, LabVIEW sends an external trigger to the delay generator which will then send a burst of pulses at the desired pulse repetition frequency to the nanosecond pulser and a single pulse to the high speed camera to start recording the event. A pressure rise recorded by the pressure transducer indicates successful ignition. If there is no pressure rise after the pulser is fired from LabVIEW, the mixture has not ignited. This would mean a faulty signal from the pulser or stratification of the gases inside the vessel. For safety purposes, the vessel is first evacuated using the vacuum pump so we don't have a reacting mixture settling inside the vessel. This is followed by a purge using nitrogen. After evacuating and purging, the experimental system is inspected for reasons of failed ignition. The test is then repeated to achieve successful ignition.

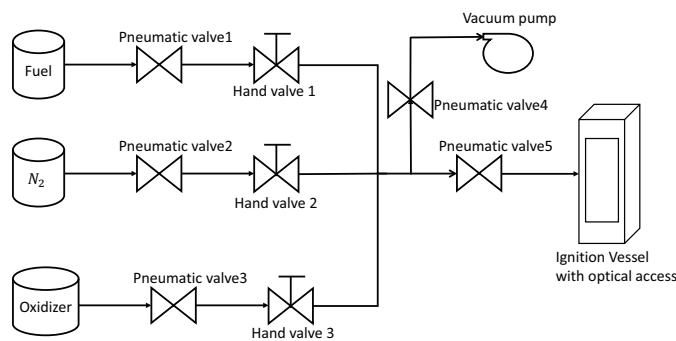


Fig. 5.2.: Plumbing diagram for plasma assisted ignition

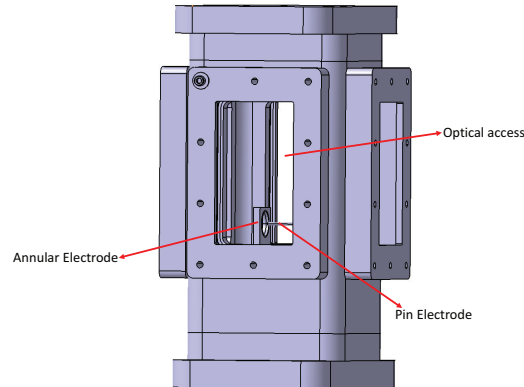


Fig. 5.3.: Schematic of the vessel used for ignition experiments

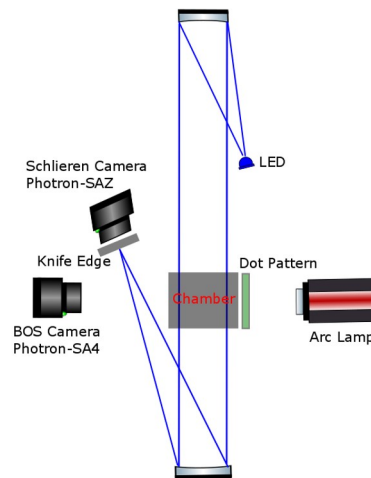


Fig. 5.4.: Optical setup for plasma assisted ignition experiment

5.3 Study of Plasma Assisted Ignition for Pin-Pin Discharges

Two sharp-tipped electrodes separated by a gap ("pin-to-pin" electrodes) is a canonical electrode configuration for applied plasma research. It is preferred over other configurations due to the formation of a single spark channel which makes it relatively easier to explore the plasma kinetics, thermal and hydrodynamic effects and also the coupling with reacting mixture. Prior to testing with the pin-to-ring electrode configuration, ignition tests are performed with the pin-to-pin electrode configuration.

The electrode gap for this experiment is maintained at 1 mm to be consistent with the streak spectroscopy measurements presented in CHAPTER 4. To examine the effect of the pulse repetition frequency (PRF) on ignition, experiments are conducted with PRFs of 5, 10, 20 and 50 kHz. The pulse duration for all experiments is kept at 100 ns and the peak voltage is kept at 25 kV. The number of pulses is adjusted to maintain a total discharge time of 10 ms. Three experiments were conducted at each PRF to assess repeatability. The schlieren and background oriented schlieren (BOS) cameras are triggered simultaneously to capture the ignition event and record at 20000 frames per second. A representative schlieren image is shown in Figure 5.5 identifying the objects in the field of view. The electrodes are placed inside the pressure vessel and are connected to the nanosecond high voltage pulser using two high pressure feedthroughs. The voltage and current probes are connected to the feedthroughs outside the vessel and the discharge voltage and current are recorded by a high bandwidth oscilloscope. The pressure and temperature inside the vessel are measured using a pressure transducer and a thermocouple mounted on the top flange of the vessel. The pressure transducer and thermocouple do not have sufficient time response to accurately measure the time evolution of the pressure and temperature, and thus are only used to verify successful ignition and combustion. The schlieren images are post-processed to obtain binary images that are used to estimate the ignition kernel radius in each frame in the sequence until the flame is no longer in the field of view. The kernel radius is then plotted as a function of time and a linear fit is made in MATLAB. The slope of the linear fit gives the stretched flame speed or flame propagation speed. The schlieren images of the flame development at 0.1, 2, 4, 6, 8 and 10 ms are shown in Figures 5.6-5.9 for the different pulse repetition frequencies. From the schlieren images for the different frequencies, the initial kernel at 0.1 ms is about 3 mm for all the PRFs. Even the final radius of the flame at 10 ms appears to be about 30-40 mm for the different frequencies. This suggests that increasing the pulse repetition frequency beyond 10 kHz has little effect on the initial ignition kernel size and the flame propagation speed for a pin-to-pin electrode configuration.

The flame has also developed by 2 ms, which is 10 pulses at 5 kHz and 100 pulses at 50 kHz. Therefore, a smaller discharge burst duration compared to 10 ms used in the current experiment is needed to ignite a reacting mixture and develop a self propagating flame. More experiments need to be performed in future to study the effect of pulse repetition frequency.

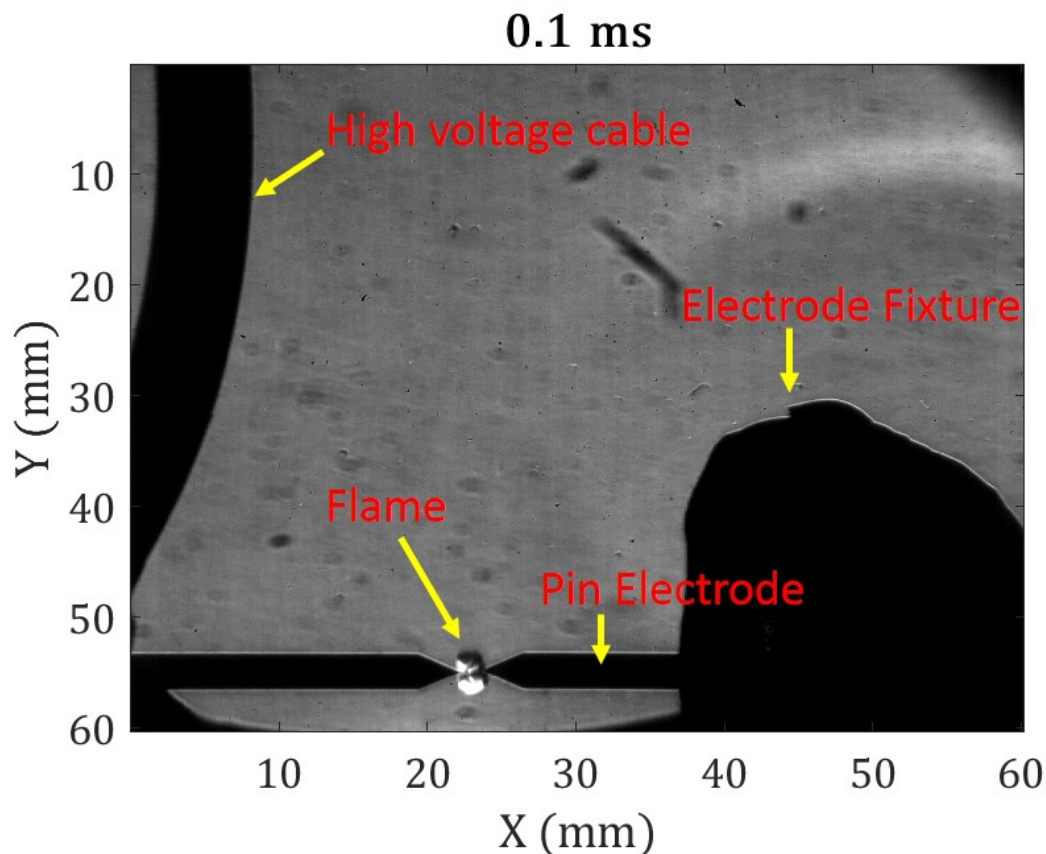


Fig. 5.5.: A schlieren image to explain the objects in the field of view

The schlieren images are post-processed using MATLAB. The steps followed for processing the image are as follows. First, the images are subtracted for background which remove any random spots on the image that are not related to the flow field, for example dust on the vessel windows or schlieren/camera lenses. Once the image is subtracted for background, the pixels having intensity in the range of 0.005 to -0.005

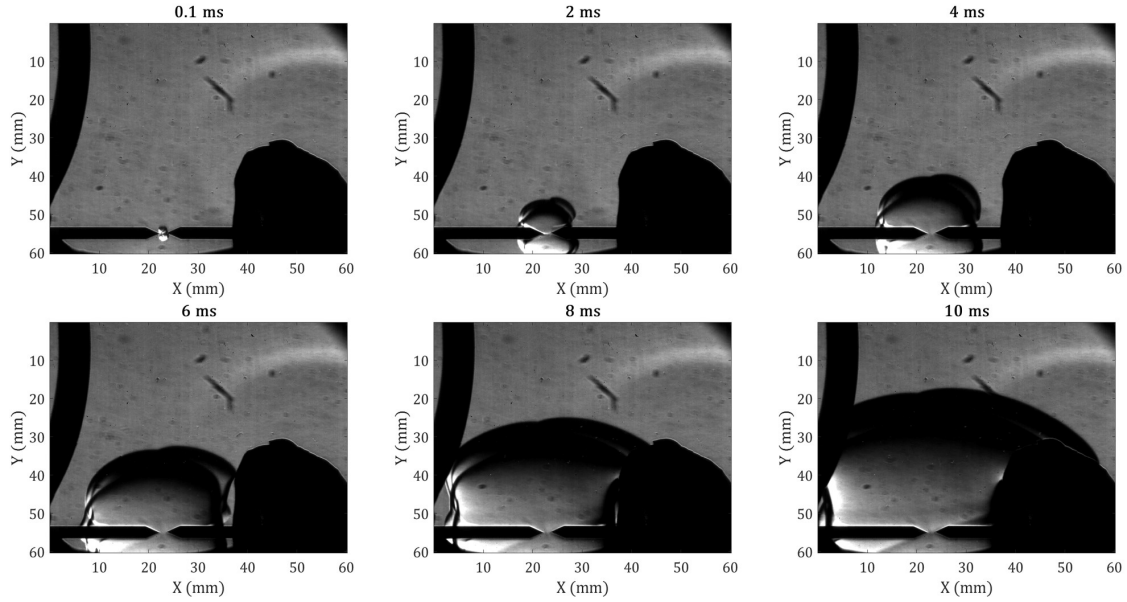


Fig. 5.6.: Schlieren images of flame development at 0.1, 2, 4, 6, 8 and 10 ms for pulse repetition frequency of 5 kHz

are made equal to zero. The image is then converted to binary format using an inbuilt function on MATLAB, specifically an adaptive binary function with a sensitivity of 0.9. The kernel area is then calculated in MATLAB. The radius of the flame front is estimated in the vertical direction using the center of the electrode gap as the origin. This process is followed for each frame in the sequence and the ignition/flame kernel radius and area can then be plotted as a function of time. The binary image for the corresponding schlieren image on Figure 5.6 is shown in Figure 5.10. The flame radius as a function of time for the different pulse repetition frequencies is shown in Figure 5.11. The flame propagation speed as a function of energy deposited per pulse of the plasma discharge is shown in Figure 5.12. The energy deposited per pulse decreases from 0.9 mJ to 0.3 mJ with increase in pulse repetition frequency. However, since there are more pulses at higher frequency, the energy per 10 ms pulse burst increases with frequency. To illustrate clearly that increasing the PRF decreases the energy deposited per pulse, only energy per pulse will be shown here. The flame propagation

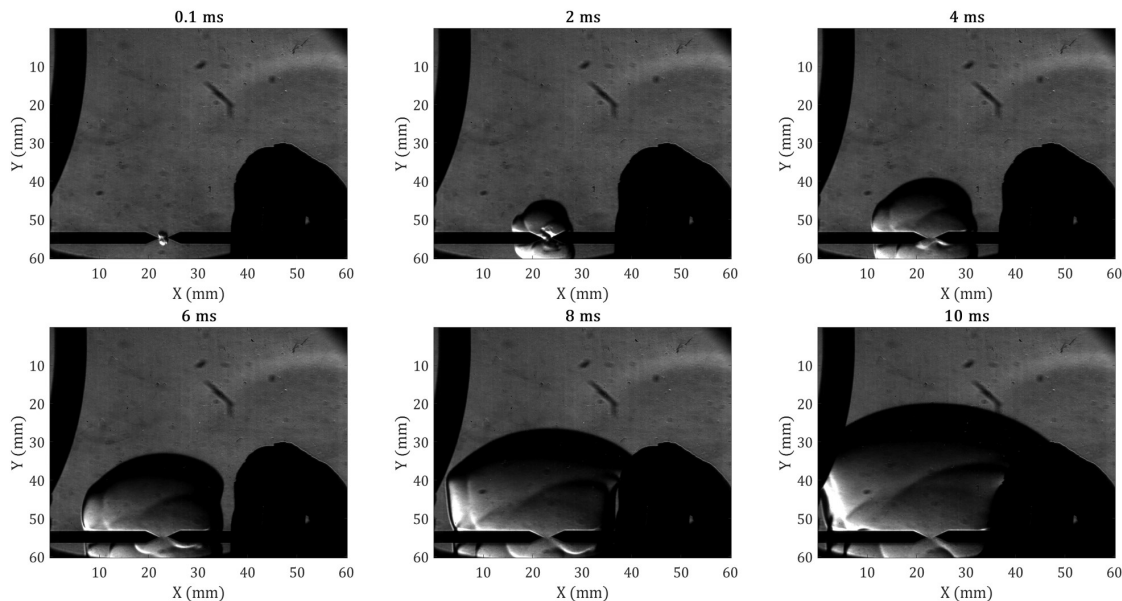


Fig. 5.7.: Schlieren images of flame development at 0.1, 2, 4, 6, 8 and 10 ms for pulse repetition frequency of 10 kHz

speed increases slightly by about 20 cm/s as the pulse repetition frequency is increased from 5 kHz to 10 kHz but remains approximately constant for further increase in PRF. The flame speed reported here is the stretched burning velocity of the flame and the values are within the range of flame speeds reported for laminar flames [96].

5.4 Study of Plasma Assisted Ignition for Pin-Ring Discharges

Having demonstrated plasma assisted ignition with a pin-to-pin electrode and observed that it produces an approximately laminar flame without significant change in flame speed with pulse repetition frequency, the electrode configuration is replaced by the intended pin-to-ring electrode configuration. In this electrode configuration the pin electrode is a 0.125 inch diameter tungsten rod which is sharpened to a point at one end using a grinding wheel. This pin electrode is similar to the one used in pin-to-pin electrode ignition experiments. The ring electrode is 0.25 inches thick and

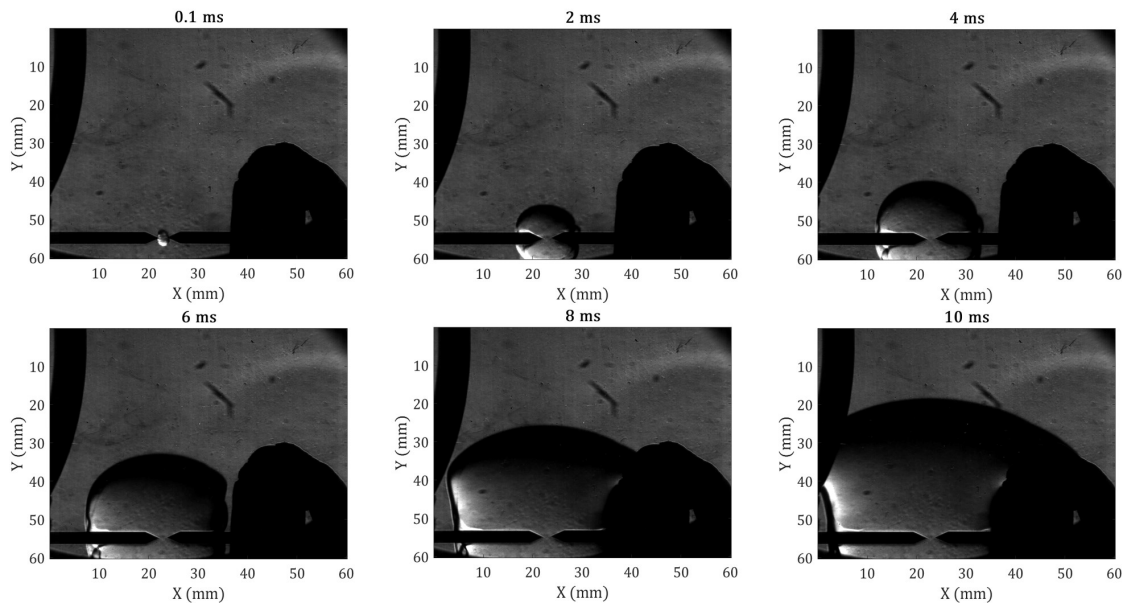


Fig. 5.8.: Schlieren images of flame development at 0.1, 2, 4, 6, 8 and 10 ms for pulse repetition frequency of 20 kHz

1 inch inner diameter. The pin electrode is concentric with the ring electrode and the axial separation between the pin and the ring electrode is 2 mm. A representative schlieren image is shown in Figure 5.13 to identify the different objects in the field of view. As with the pin-to-pin electrodes, experiments are conducted with PRFs of 5, 10, 20 and 50 kHz with a fixed pulse duration of 100 ns and 25 kV peak voltage. As before, the number of pulses is adjusted to obtain a total discharge time of 10 ms. The flame development over 10 ms for the different pulse repetition frequencies is shown in Figure 5.14-5.17. The first image in these figures is taken at 0.1 ms for all pulse repetition frequencies except 5 kHz, where the first visible density gradient was seen at 0.3 ms. For a PRF of 5 kHz, the flame propagation is slower compared to the pin-to-pin electrode configuration. This could be because with only 50 pulses at 5 kHz, there are fewer streamers and the ignition starts at a single point close to the pin electrode as opposed to volume ignition. At higher pulse repetition frequencies, the flame propagation speed is higher after ignition in the pin-to-ring

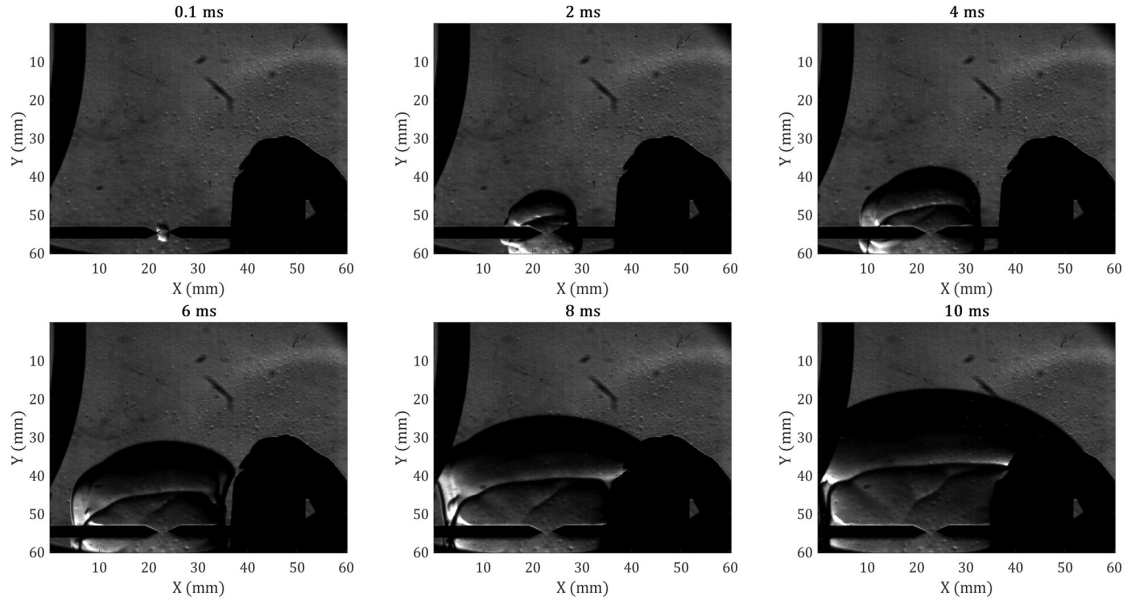


Fig. 5.9.: Schlieren images of flame development at 0.1, 2, 4, 6, 8 and 10 ms for pulse repetition frequency of 50 kHz

configuration compared to the pin-to-pin case. At PRFs greater than 10 kHz the initial ignition kernel size at 2 ms is much larger in the pin-to-ring configuration. Comparing the flame radius at the discharge end time of 10 ms for pin-to-pin and pin-to-ring electrode, at PRF of 5 kHz, the pin-to-pin electrode is about 35 mm, while in the pin-ring electrode the radius is about 20 mm. At higher frequencies, the pin-pin electrode produces a slightly flame radius of 35-40 mm, while the pin-ring electrode produces a flame radius of about 35-50 mm. This indicates that the pin-ring electrode enhances the flame speed at higher pulse repetition frequencies much more than pin-pin electrode. To obtain the flame radius evolution as a function of time, the schlieren images are processed using a similar method to described in Section 5.3 for the pin-to-pin electrodes. The image is first subtracted for background then converted to a binary image and the edge position is obtained. Since in the pin-to-ring electrode configuration there is considerable blockage of field of view in the vertical direction due to the presence of ring electrode, the edge position along the horizontal

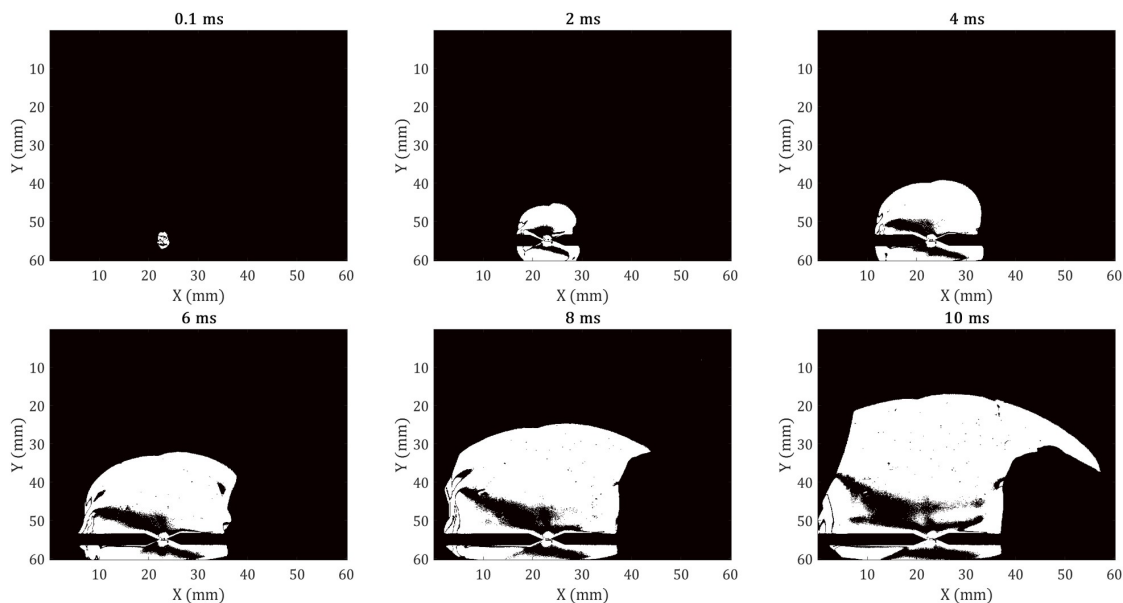


Fig. 5.10.: Binary images of flame development at 0.1, 2, 4, 6, 8 and 10 ms for pulse repetition frequency of 5 kHz

is obtained and the flame radius is estimated from the tip of the pin electrode. This analysis is performed for every frame and the flame radius is plotted as a function of time. A linear fit is then made to this plot and the slope of the fit gives the flame propagation velocity. The binary image for the corresponding schlieren image in Figure 5.17 is shown in Figure 5.18. The change in flame radius as a function of time for the different pulse repetition frequencies is shown in Figure 5.19. The slope of the lines change as the PRF is increased from 5 kHz to 50 kHz indicating an increase in the flame propagation velocity with pulse repetition frequency. The flame speed as a function of energy deposited per pulse is shown in Figure 5.20. As in the pin-to-pin electrode case, the energy per pulse decreases with increase in PRF but the energy is higher overall for the pin-to-ring configuration. It was observed that in the pin-to-pin electrode configuration the flame speed remained approximately constant with PRF increasing past 10 kHz, but in the case of the pin-to-ring electrodes the flame speed increases monotonically PRF. The speed increases from 265 cm/s to 388 cm/s as the

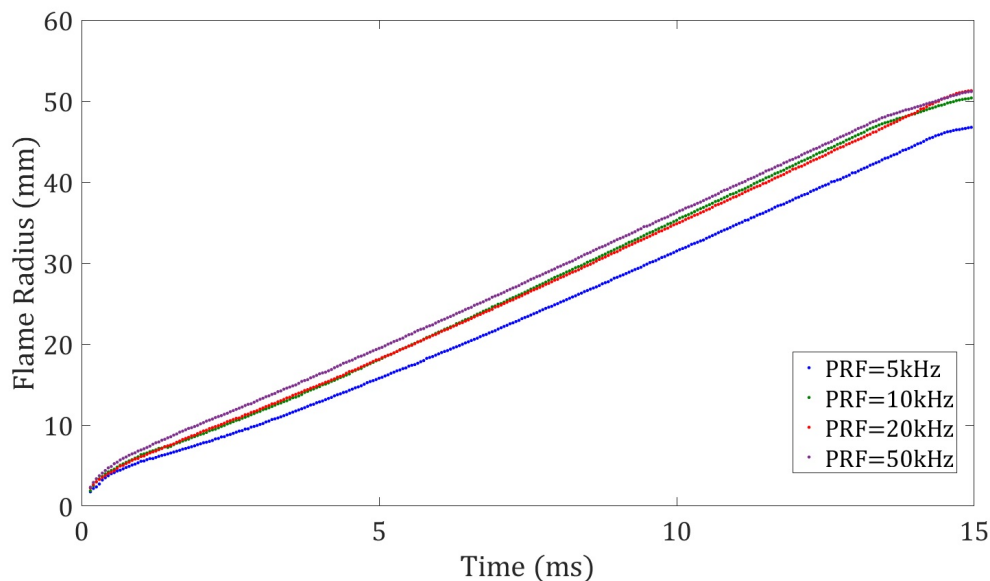


Fig. 5.11.: Comparison of radius evolution as a function of time for the different pulse repetition frequencies for the pin to pin electrode configuration

PRF is increased from 5 kHz to 50 kHz. Comparison of the flame speed vs. PRF between the pin-to-pin and pin-to-ring electrode configurations is shown on Figure 5.21. At PRFs of 10 and 20 kHz, the flame speeds for the pin-to-pin and pin-to-ring configurations are quite close, however at 50 kHz the flame speed for the pin-to-ring configuration is significantly higher.

5.5 Discussion of Flame Dynamics

The PAI results for both the pin-to-pin electrodes and the pin-to-ring electrodes show interesting trends. With the pin-to-pin electrode the flame speed increases slightly for an increase in PRF from 5 to 10 kHz but is minimally effected by a further increase in PRF. With the pin-to-ring electrode configuration, however, the flame speed increases monotonically with pulse repetition frequency. To explain the effect of plasma discharges on the flame dynamics, the relatively simple reaction

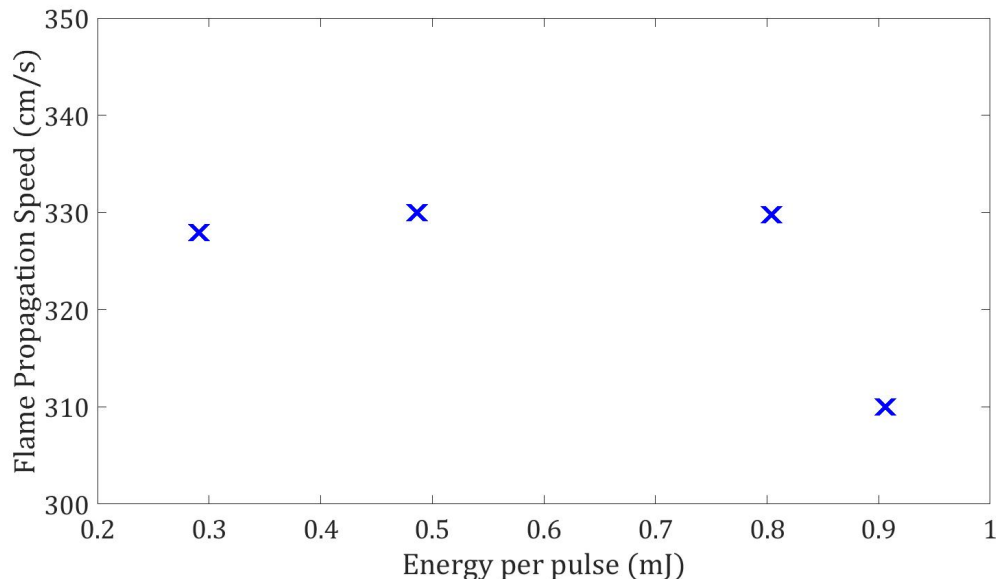


Fig. 5.12.: Flame propagation speed as a function of energy deposited per plasma pulse

mechanism of hydrogen and oxygen is considered like in the recent PAI/PAC review paper by Ju and Sun [2]. The main reactions of interest, namely the chain initiation, branching, and termination reactions, are given as Reactions 1-7 in Figure 5.22 [2].

First the reactions without plasma (R1-R7) are considered to explain the ignition behavior. For a flame to be initiated, the chain initiation reaction must first generate a sufficient pool of radicals, followed by chain branching reaction which leads to exponential increase in temperature. There are also chain termination reactions that can overtake the chain branching and lead to flame blow out. The chain initiation reaction in the hydrogen-oxygen-nitrogen mixture is R1 in Figure 5.22 where the fuel breaks up into H and HO₂. The atomic hydrogen produced in R1 initiates the chain branching through reaction R2 which produces atomic oxygen and OH, which then generate more hydrogen radicals through reactions R3 and R4. Reaction R2 in this mechanism has high activation energy and is accelerated at high temperature.

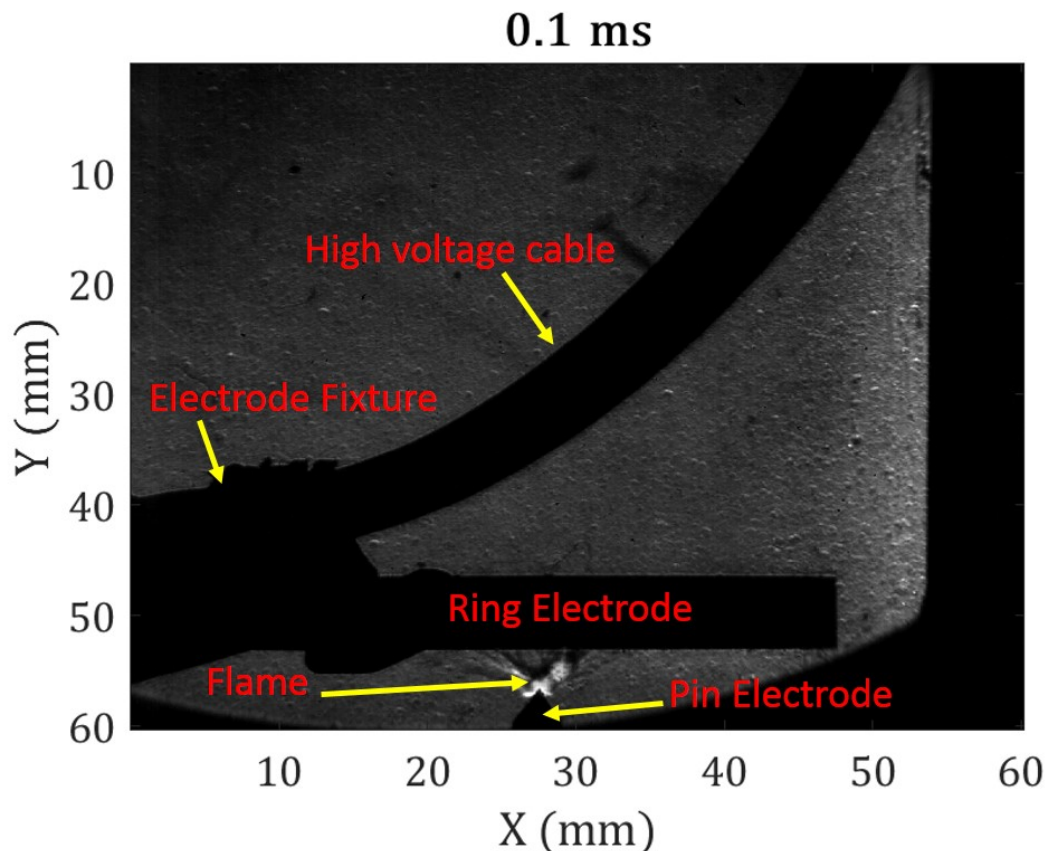


Fig. 5.13.: A schlieren image to explain the objects in the field of view

In this case the ignition delay is controlled by reactions R1 and R2 which are the slow reactions in this mechanism. When there is a plasma discharge, there is electron impact dissociation, plasma activated reaction and catalytic branching. These plasma reactions produce atomic oxygen and nitric oxide. The atomic oxygen produced by plasma assists in bypassing reactions R1 and R2, leading to faster production of atomic hydrogen through reactions R3 and R4.. Additionally, the nitric oxide produced by the plasma at low temperature acts as a catalyst in the ignition reaction chain. Therefore plasma is more effective in reducing ignition delay.

As discussed in section 1 of the chapter, plasma discharges enhance ignition in almost all fuel molecules. But the chemistry for hydrocarbon fuels is slightly compli-

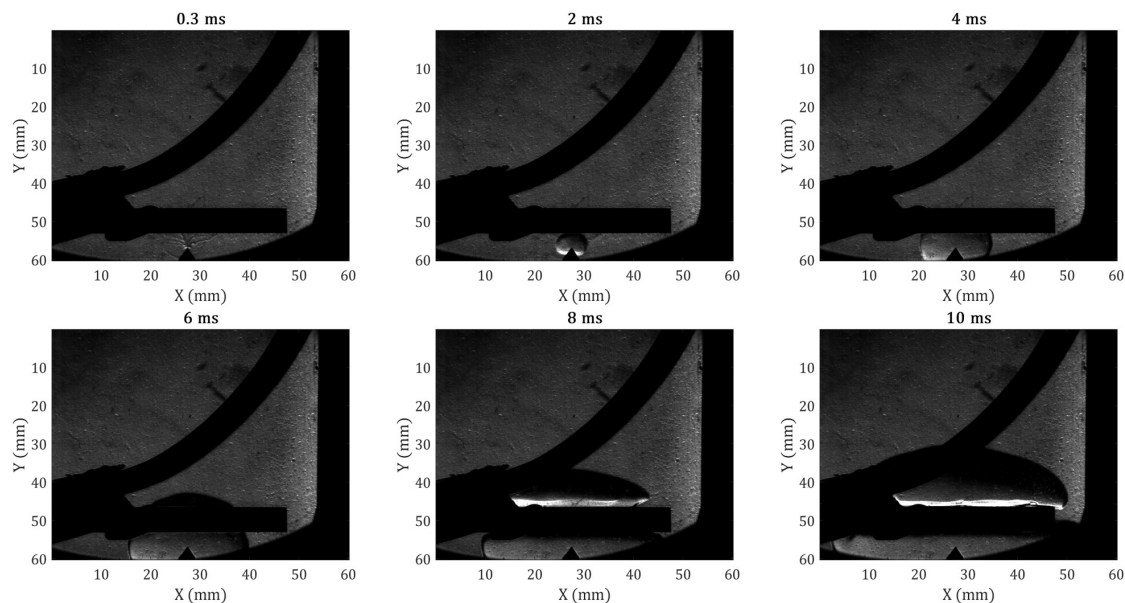


Fig. 5.14.: Schlieren images of flame development at 0.3, 2, 4, 6, 8 and 10 ms for pulse repetition frequency of 5 kHz

cated compared to Hydrogen. Generally in hydrocarbon fuels, there are two ignition delay times, a low temperature ignition and high temperature ignition. Some of the important reactions for hydrocarbon fuels are shown below in Figure 5.23. In the low temperature regime, reaction R15 is slow due to insufficient radicals, therefore it limits the formation of hydrocarbon radicals. The branching reactions of R18-R20 plays an important role in low temperature ignition. At intermediate temperatures, reaction R6 is accelerated and leads to a transition towards high temperature ignition. This is dependent on presence of active radicals. Creation of a pool of external radicals and heat will accelerate the process of high temperature ignition through reactions R21-R24. When the mixture is fuel rich, then there are additional plasma induced reactions in the form of R25 and R26. At temperatures below 1000 Kelvin, the electron impact reactions from plasma discharge dominates over chain branching reactions, but at temperatures greater than 1000 Kelvin the conventional chain branching dominates over plasma reactions. Therefore at low temperatures, plasma

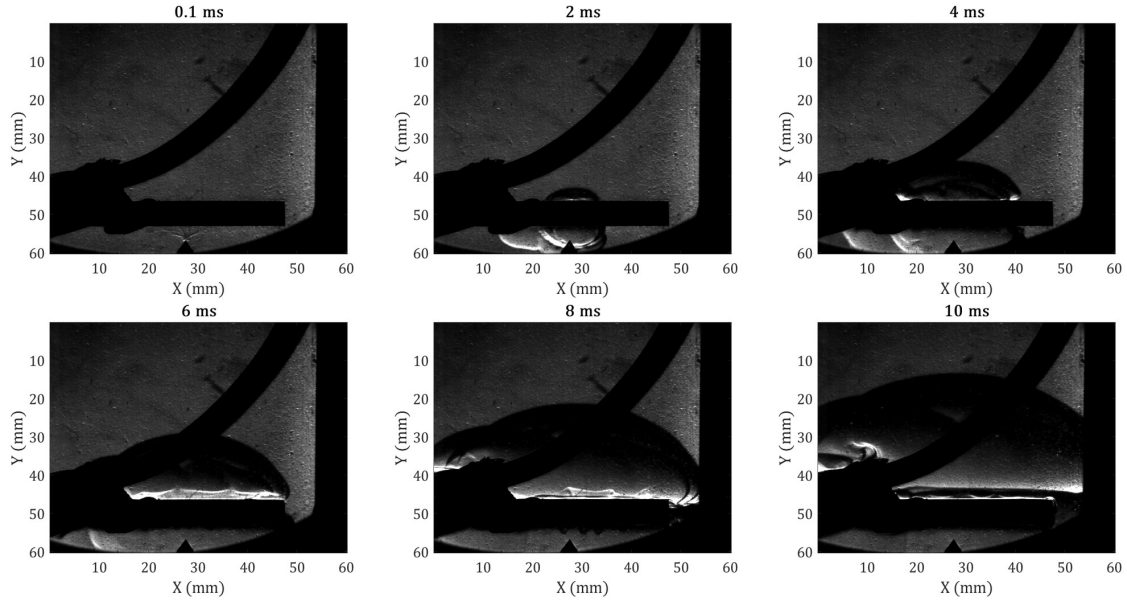


Fig. 5.15.: Schlieren images of flame development at 0.1, 2, 4, 6, 8 and 10 ms for pulse repetition frequency of 10 kHz

enhancement is mostly kinetic, while at high temperatures the thermal enhancement starts to dominate.

Once a flame is initiated, it self propagates exothermically as a "thermal diffusion auto ignition front" [2]. The burning velocity is dependent on fuel oxidation chemistry, transport properties, adiabatic flame temperature, and heat and mass losses. Heat loss from the flame leads to reduction in flame speed and addition of radicals by the plasma leads to increase in flame speed. The flame speed with radiation heat loss normalized by the adiabatic flame speed can be written in terms of the heat loss normalized by the chemical heat release rate of the fuel mixture, the Lewis number, Karlovitz number and heating from the plasma:

$$U^2 \ln(U^2) = -\beta^* H + \beta^* Q^* - \beta^* (Le^* - 1) Ka^* \quad (5.1)$$

Where U is the flame speed, β is the global activation energy given as:

$$\beta = (E_a(T_{ad} - T_u)) / (R_o T_{ad}^2) \quad (5.2)$$

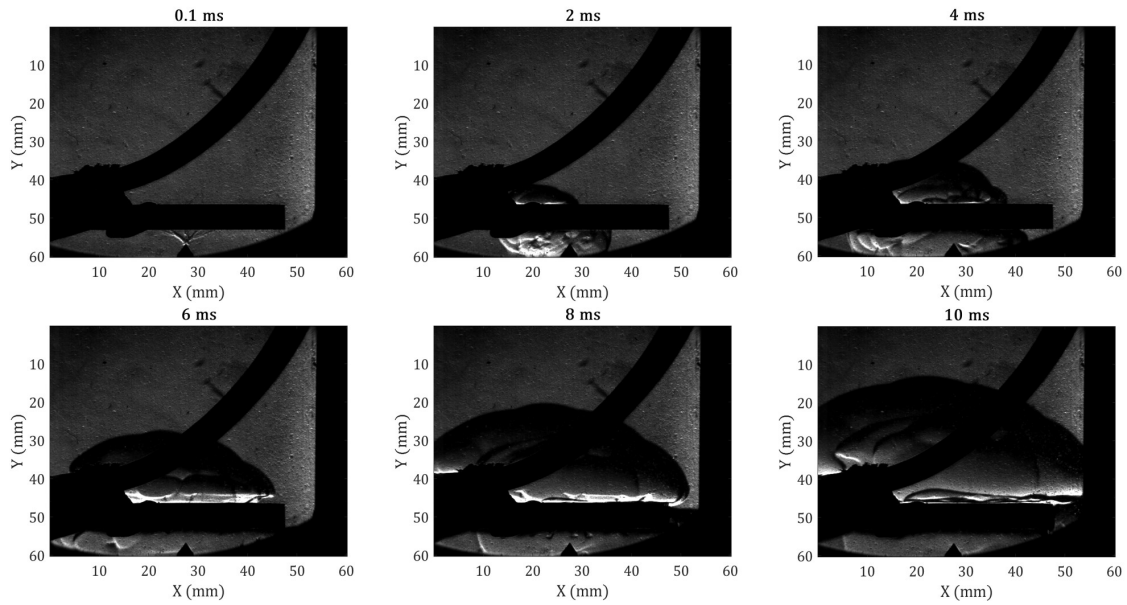


Fig. 5.16.: Schlieren images of flame development at 0.1, 2, 4, 6, 8 and 10 ms for pulse repetition frequency of 20 kHz

Q is the heating from the plasma to the flame, H is the heat loss from the flame, Le is the Lewis number which is the ratio of thermal diffusivity to mass diffusivity, and Ka is the Karlovitz number which is the ratio of the chemical timescale to the Kolmogorov time scale or can be written as the ratio of square of flame thickness to the square of Kolmogorov length scale. When the Lewis number is more than 1, the thermal diffusion from the flame is dominant over the transport of fuel radicals. When the Lewis number is less than one, the mass transport of the fuel is dominant and more radicals get transported to the flame front, resulting in positive stretch and increase in flame speed. A Karlovitz number less than one indicates that the flame thickness is smaller than the Kolmogorov length scale and therefore the flame speed is not affected by turbulence in the flow field.

There are three terms in the Equation 5.1 that affect the flame speed and thus provide potential avenues for plasma enhancement. The first term is the global activation energy which gets reduced due to production of radicals by plasma (kinetic

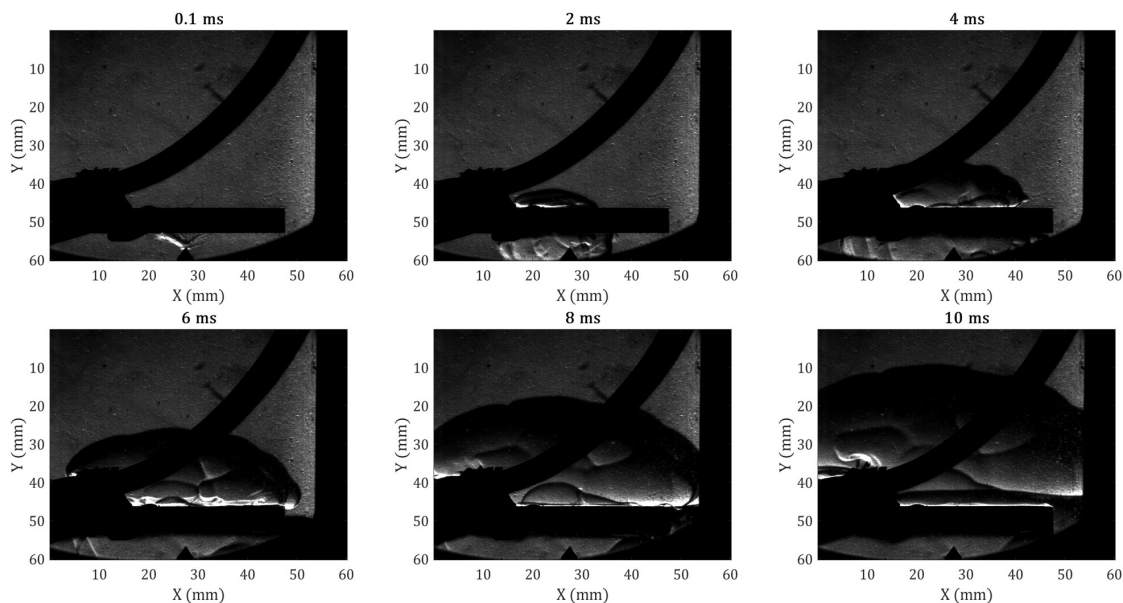


Fig. 5.17.: Schlieren images of flame development at 0.1, 2, 4, 6, 8 and 10 ms for pulse repetition frequency of 50 kHz

effect). However, this reduction is dominant at low temperature, but once the flame is created and is hot, the reaction R2 is dominant and the radical production rate of the plasma is slower compared to R2 at high temperatures. Therefore, the first term in the equation has a weak effect on flame speed. The second term is the heat deposited by plasma, which can accelerate the flame. This thermal effect is stronger than the kinetic effect because an increase in temperature due to plasma greatly accelerates reaction R2 because its rate is highly temperature dependent. The third term in Equation 5.1 is the Lewis number which can be less than one in plasma-assisted ignition because the plasma can break large fuel molecules into lighter ones and thus increase the rate of mass transport vs. thermal diffusion. The plasma discharge can change the local flow field through production of ionic wind or through ultrafast heating where the heat release produces pressure waves leading to flow instabilities and vorticity generation. This hydrodynamic flow results in change of Karlovitz number.

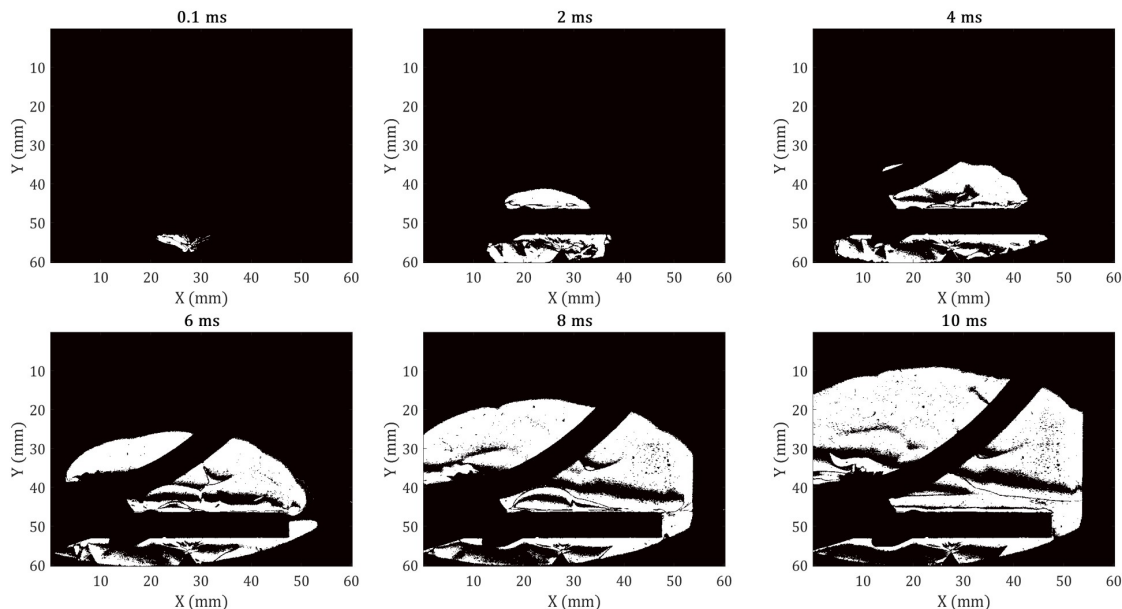


Fig. 5.18.: Binary images of flame development at 0.1, 2, 4, 6, 8 and 10 ms for pulse repetition frequency of 50 kHz

With these factors influencing the flame speed in mind, the effect of the plasma discharges on the flame speed is now discussed. First, the pin-to-pin electrode configuration is considered in a quiescent gas mixture of fuel and oxidizer. The results presented in Section 5.3 indicate that the flame speed changes from 310 cm/s to 329.8 cm/s as the pulse repetition frequency is increased from 5 to 10 kHz and stays constant for PRF of 10 to 50 kHz. As discussed in the preceding paragraphs, oxygen atoms are important in ignition. A single plasma discharge can dissociate oxygen molecules into oxygen atoms and if the circulation time is faster than the pulse repetition frequency, a fresh volume of oxygen molecules are brought into the electrode gap by this vortex, which results in further dissociation to oxygen atoms by subsequent pulses. Once the flame has been initiated, the temperature rises significantly and now the radical production rate is slower from the plasma. The 3-D direct numerical simulations from Castela et. al. It is possible that at higher frequencies the radicals

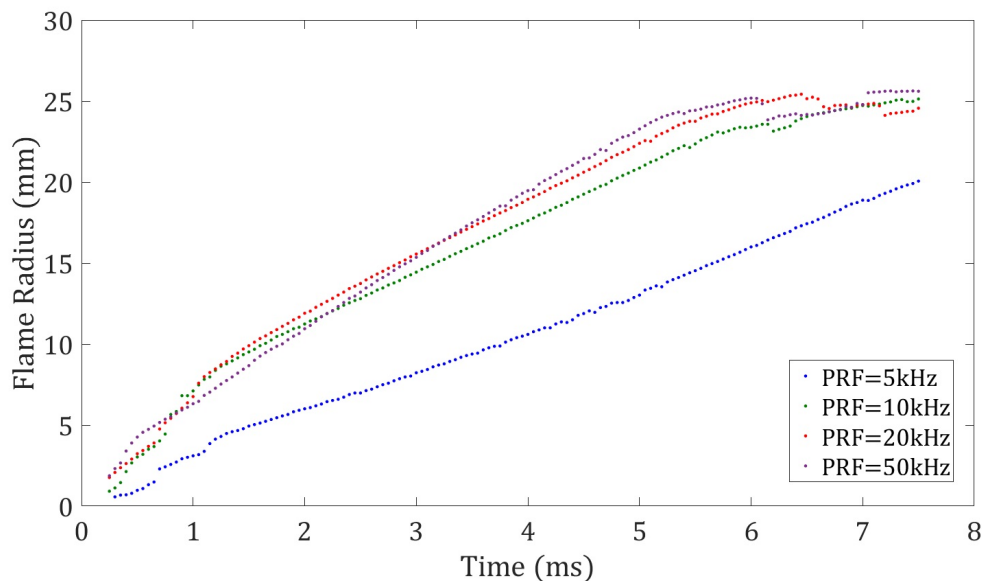


Fig. 5.19.: Comparison of radius evolution as a function of time for the different pulse repetition frequencies for the pin to ring electrode configuration

are produced faster but once all the O atoms are depleted at the electrode gap, there is no effect of increasing frequency. The Lewis number might change with increase in pulse repetition frequency but once the fuel molecules at the electrode gap has been transported, there is no change of the Lewis number. These reasons could explain why there is no change in flame speed.

With the pin-to-ring electrodes, as the pulse repetition frequency is increased, the number of pulses is also higher and a larger number of spark channels are produced. Each spark channel breaks the fuel molecules at different locations, adding to mass transport of fuel, which leads to reduction of overall Lewis number, therefore creating a positive effect of flame speed at higher pulse repetition frequencies. These individual spark channels also contribute to adding heat to the flame, therefore increasing Q in the flame speed equation, leading to positive effect of flame speed at higher frequencies. Therefore, overall the pin-to-ring electrode configuration has a positive

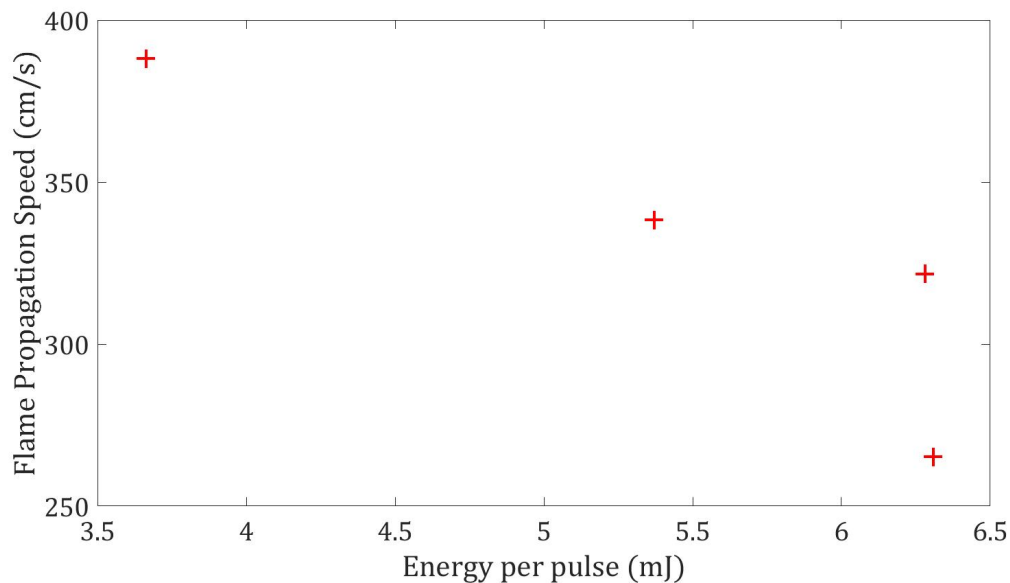


Fig. 5.20.: Flame propagation speed as a function of energy deposited per plasma pulse for the pin to ring electrode

effect on flame speed as the pulse repetition frequency is increased, however, further work is needed to fully understand these effects. In the current experiment, the schlieren images only provide information on density gradients, but no information on the chemical species present in the kernel. High-speed chemiluminescence could be implemented to detect OH or CH in the flame. It might also be useful to perform two photon laser induced fluorescence (LIF) measurements to detect O atoms created by the plasma prior to ignition or formaldehyde LIF to investigate fuel break up and its enhancement of mass transport.

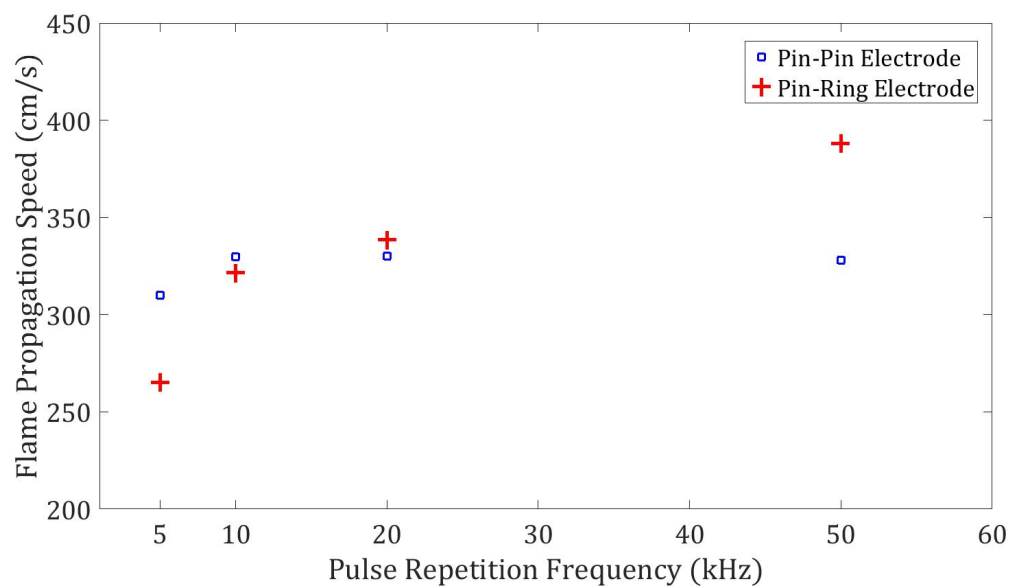


Fig. 5.21.: Flame speed comparison for the two electrode configurations at different pulse repetition frequencies

<i>Chain-initiation</i>	
$H_2 + O_2 = HO_2 + H$	(R1)
<i>Chain-branching/propagation</i>	
$H + O_2 = OH + O$	(R2)
$O + H_2 = OH + H$	(R3)
$OH + H_2 = H_2O + H$	(R4)
$HO_2 + H = OH + OH$	(R5)
$H_2O_2 = OH + OH$	(R6)
<i>Chain-termination</i>	
$H + O_2(+M) = HO_2(+M)$	(R7)
$HO_2 + H = H_2 + O_2$	(R1)
<i>Electron and $N_2(^*)$ impact dissociation</i>	
$e + O_2 = O + O(^1D)$	(R8a)
$e + O_2^+ = O + O$	(R8b)
$N_2(A,B,C) + O_2 = O + O + N_2$	(R9a)
$N^+ + O_2 = O^+ + NO$	(R9b)
<i>Plasma activated reactions</i>	
$H + O_2(^1\Delta_g) = O + OH$	(R10)
$O_3 + O_2 = O + O_2 + O_2$	(R11)
$O(^1D) + H_2 = OH + H$	(R12)
<i>NO catalytic branching</i>	
$NO + HO_2 = NO_2 + HO$	(R13)
$H + NO_2 = NO + OH$	(R14)

Fig. 5.22.: The main reactions for hydrogen nitrogen and oxygen mixture [2]

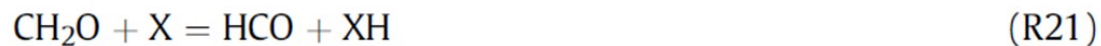
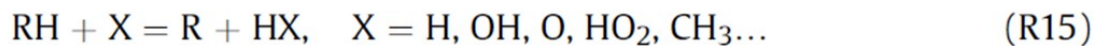


Fig. 5.23.: The main reactions for a hydrocarbon ignition [2]

6. SUMMARY

The current work has two primary goals: to investigate the wave rotor combustor as a highly-efficient pressure gain combustion device, and to explore the use of plasma-assisted ignition in such a system.

Wave rotors are expensive to fabricate and require precise design of the rotor geometry, and thus numerical tools are critical for design iteration and optimization. A quasi 1-D numerical model of a wave rotor combustor was developed nearly three decades ago and was used to design the wave rotor experimental rig at Purdue's Zucrow Labs."

Performing experiments on wave rotor combustion device requires precise design of the wave rotor geometry. However, this model is limited to axial flow wave rotor devices which do not produce shaft work. In the current work, the conservation equations for the axial flow machine were modified to account for blade curvature and implemented in the computational model. After validating the updated model, it was used to simulate a three port wave rotor cycle with non-reacting flow and two different methods were used to estimate the shaft work.

Two components were identified to contribute to shaft work production: 1) incidence of flow turning from the inlet to duct to inside of the wave rotor, 2) flow turning from the inlet plane of the wave rotor to the exit plane of the wave rotor. The flow incidence at the inlet leads to flow separation at the inlet and stagnation pressure loss. Therefore it is important to minimize incidence loss at the inlet. The incidence loss model implemented in the overall wave rotor model was used to design the inlet duct such that the incidence loss was minimized and the only flow turning that produced shaft work was due to turning of flow from inlet plane to exit plane.

The computational model was then used to simulate a wave rotor with non-axial channels and internal combustion. First, an axial flow wave rotor was modeled and the

inlet and exit port timings were optimized to minimize flow leakage and the inlet duct was optimized for zero incidence loss. After the initial optimization, the blade exit angles were changed in steps of 5° . The change in blade curvature added extra path length for the pressure waves, the ports and thus the port closing and opening was adjusted again to minimize additional leakage. The shaft work was then estimated for the optimized wave rotor with non-axial channels and internal combustion. It was observed that at higher blade curvatures, it was getting harder to transport fuel air mixture from inlet to exit plane of the rotor and initiate combustion.

The outcome from meeting the first primary research goal is a computational design tool that will be used for designing optimal wave rotor with non-axial channels and internal combustion for experimental research. Specifically, the computational tool will be used to design the wave rotor geometry including the curvature of the passages and the port timing, saving significant time and resources associated with costly experimental campaigns. Another aspect of the wave rotor that needs to be optimized is the ignition source. Therefore, the second primary goal of this work was to investigate the possibility of using plasma assisted ignition for wave rotor combustors.

Designing plasma actuators for ignition in wave rotors is challenging. In the wave rotor there is a port to initiate ignition. The plasma actuator needs two electrodes to create the plasma and should be designed to integrate with this ignition port. The actuator is designed to create the plasma discharge from a pin electrode to the walls of the wave rotor channel. The channels of the wave rotor create a rectangular cross-section for the pin electrode, giving a pin-rectangle plasma actuator. Such a plasma actuator provides multiple pathways to create the spark channel and is rarely studied to characterize the discharge. There has been some work in studying plasma discharge with a pin-ring electrode. Prior to investigating a pin-rectangle actuator, a pin-ring actuator is selected to make some comparisons with published work. Understanding the working of a pin-ring actuator will make it an easy transition to pin-rectangle actuator. The research had three steps: characterize the actuator in atmospheric

pressure, room temperature air, develop diagnostics to investigate plasma associated chemistry and third is to investigate ignition with the pin-ring actuator.

Characterizing the plasma is important because ignition of a reacting mixture depends on kinetics, thermal and hydrodynamic effect from the plasma. The formation of plasma discharge in the pin-ring actuator is studied using intensified CCD camera, the induced fluid flow is studied using high speed schlieren and the kinetics and thermal effect is studied using a novel experimental technique using the streak camera. In the long exposure imaging study using the ICCD camera, three different modes of the plasma discharge are observed: streamer channels, distributed spark and localized spark. At low pulse repetition frequencies and smaller number of pulses, a number of spark channels are observed. As the frequency and number of pulses are increased the discharge becomes distributed throughout the circumference of the ring electrode. The plasma discharge is then imaged with a high speed camera and it was observed that in the pin-ring actuator, the plasma is formed as a single channel and it moves around the circumference of the ring electrode. Additional diagnostics will be needed to understand the movement of the discharge around the ring electrode. A distributed plasma in the pin-ring actuator induces fluid motion which can be investigated using schlieren and particle image velocimetry. In this research, schlieren is used to characterize the fluid motion. It was observed that as the frequency and number of pulses are increased, the net induced flow increases. There is flow in the axial direction pushing the fluid out from the electrode location and there is tangential motion providing swirl. Quantitative schlieren and piv needs to be performed in future to quantify this induced motion. The third aspect on kinetic and thermal effect is investigated using a streak camera system. The experiment is used to with a pin-pin electrode since its an easier discharge to work with. The system was used for optical emission spectroscopy. It was observed that lifetime of electronically excited nitrogen is shortlived and quickly forms oxygen atoms, resulting in ultrafast heating. The ultrafast heating is measured be recording emission spectra of nitrogen second positive system and later using a temperature fitting sotware to obtain rotational and

vibrational temperature. It was observed that ultrafast heating is on the order of 800 Kelvin within 10 ns of the discharge.

The outcome from meeting the second and third primary research goal is a preliminary understanding of plasma discharge in a pin-ring actuator and an experimental technique to make ultrafast measurements of plasma kinetics and thermal effects. This preliminary work on characterizing the hydrodynamic flow induced by the plasma formation in pin-ring actuator has motivated future efforts to quantify the induced fluid flow using background oriented schlieren and particle image velocimetry. Preliminary work with the streak-spectroscopy has shown that the glow from Nitrogen second positive system lasts few tens of nanoseconds and the shock induced fluid flow happens much later. This limitation has motivated the exploration of coherent Anti-Stokes Raman spectroscopy to measure heating in the afterglow of the plasma discharge.

In the second phase of this component of the research, plasma-assisted ignition experiments were conducted to understand how the advantages of plasma identified during characterization helps in ignition. First an experimental facility for plasma ignition was developed, including an optically accessible combustion vessel so the ignition and flame propagation processes could be observed. With this facility, plasma assisted ignition experiments are carried out with a pin to pin electrode and pin to ring electrode configuration and the flame development was observed using high-speed schlieren visualization.

The results with the two electrode configurations show that the pin to pin electrode has a slight increase in flame velocity as the pulse repetition frequency is increased, but remains approximately constant for further increase of PRF up to 50 kHz. In the case of pin to ring electrode the flame velocity keeps increasing with pulse repetition frequency. From the schlieren images, it can be observed that the initial flame volume for pin to ring configuration is larger compared to the pin to pin electrode. Measuring voltage and current simultaneously allowed for calculation of the energy deposited in the plasma pulse. It was found that the energy per pulse for pin to ring configuration

was higher compared to pin to pin electrode. However in the case of pin to ring electrode the number of spark channels is higher so the energy is distributed over those spark channels. Overall the results show that creating a plasma with a pin to ring electrode configuration produces a faster flame and a higher volume of the gas is burned in lesser time compared to the pin-pin actuator. This suggests that using a pin electrode at the ignition port and creating plasma discharge to the channel walls leads to penetration into the channel which can then ignite a volume of gas simultaneously. The plasma can be created in a controlled fashion at high repetition rates and requires fewer mechanical parts compared to hot jet ignition. Further investigation is required with larger gaps and using a rectangular cross-section instead of the ring electrode to closely simulate the channel geometry of the wave rotor. These continued investigations will help to develop an efficient ignition source for the wave rotor.

This research has therefore provided tools to make significant progress in designing a wave rotor with non-axial blades and internal combustion. Firstly, the current work has produced a validated computational tool that can be used to design and optimize non-axial channel wave rotors, Secondly, in the research new experimental techniques and facilities were developed for investigating ultrafast phenomenon in plasma discharges and plasma assisted ignition.

7. RECOMMENDATIONS FOR FUTURE WORK

7.1 Wave Rotor Combustion Turbine Development

In this current work, the numerical model only investigated wave rotors without any loss generating factors such as frictional effects along the length of the channel, internal leakage of gas from the wave rotor and heat transfer to the wall. The other effect is the opening time of the channel. These factors are already there as empirical model in the code, but haven't been used in this work. The empirical model is calibrated with past experiments with axial channel wave rotors. These factors need to be considered as part of future work in order to estimate shaft work in the non-ideal case. Currently the numerical model uses a parabolic profile for the channel, but in future this can be modified with any arbitrary non-linear equation to consider generic blade profiles as in the case of turbines. The numerical model for incidence needs to be further investigated for cases with non-axial inlet of the wave rotor. The numerical model for combustion is currently based on temperature of the computational cell and species mass fraction. A better combustion model needs to be implemented in future to account for species from plasma initiated reactions. The shaft work is estimated using two methods for numerical validation, however it needs to be verified with experimental data in future. Finally, the convergence of a wave rotor cycle is checked by doing mass balance between inlet and exhaust ports, however there needs to be an additional check on energy balance for total convergence. If the convergence is not reached then the shaft work from energy conservation will be different compared to angular momentum conservation.

7.2 Use of Streak Camera for Future Measurements

In this current work, the development of experimental technique using streak camera with and without spectrometer took considerable time and effort. The measurement technique is useful to make ultrafast measurements on plasma discharge. So far with this technique, measurement of lifetime of electronically excited nitrogen has been made along with temperature measurement. Without the spectrometer, it has been used to image the broadband luminescence of plasma discharge. It has been observed that for longer pulse durations there is a reappearance of glow which lasts for a longer time. This has given the idea to perform spectrally resolved direct imaging of plasma with the streak camera. This can be done by adding spectral filters in front of the streak camera and correlating the streak image with current waveform. This will then provide information regarding emission during different parts of the current waveform. Such information can provide experimental evidence of how the kinetic reactions evolve as the plasma progresses in time. This can be extremely crucial for numerical model validations. It will also provide a full picture of the plasma glow. For instance in the current work, the second positive system is used to estimate gas temperature, but the emission lasts only for 20 ns, therefore providing information during the first few nanoseconds of the discharge. However in the streak imaging of the plasma, a longer glow lasting for hundred nanoseconds was observed. If the spectrally resolved imaging provided information regarding the wavelength of emission then the streak spectroscopy can be performed at this wavelength to obtain temperature at later point in the discharge. Another interesting experiment for streak imaging would be to use in experiment on two photon PLIF of oxygen atoms, first to get its lifetime and then correlate it with voltage and current wave forms to check where in the plasma regime it gets generated. In general, where ever an intensified CCD is used, it can be replaced with a streak camera.

7.3 Improvement to Plasma Assisted Ignition

In the current work plasma assisted ignition was performed with electrode fixtures that were big and blocking optical access. The blockage was not a big concern in the case of pin to pin electrode, but in the case of pin to ring electrode the ring electrode was blocking the flame propagation. For future work, the ring electrode needs to be designed thinner so that it is not blocking the optical view. It is also observed that since the chamber dimensions are small, the electrical cables that connect to the electrodes were harder to keep out of the optical field of view since they had to be two inches from the walls of the chamber. So for future experiments it is advisable to design the electrodes without a fixture and such that they connect directly to feedthroughs, therefore avoiding use of electrical cables. It is important for schlieren to capture both the initial parts of flame kernel and also the propagation of the flame without optical blockage. It might also be useful to redesign the chamber and its flanges that hold the optical windows since they were prone to cracks while tightening the flange. In the current experiment, only schlieren is used to visualize the flame. But a schlieren only records changes in density across the flame and no information is obtained regarding chemical species or start of ignition. It will be nice for future work to add high speed chemiluminescence and laser induced fluorescence to provide information regarding species formation prior to ignition and during flame propagation. This will help understand the impact of plasma discharge on ignition and flame speed. It will help to understand the effect of mass transport on flame speed. It will be useful to perform ignition tests at different equivalence ratios and pressures to understand the range of ignition with pin to ring electrode. Future work will also need to perform ignition tests with larger axial gaps between pin and ring electrode to show that the plasma can penetrate deep into the wave rotor channel and initiate ignition and fast combustion. This data will help compare plasma assisted ignition with hot jet ignition which is the current method used for wave rotors and check the possibility of replacing hot jet ignition with plasma assisted ignition.

REFERENCES

REFERENCES

- [1] G. Sun, P. Akbari, B. Gower, and N. Mueller, "Thermodynamics of the Wave Disk Engine," in *48th AIAA/ASME/SAE/ASEE Joint Propulsion Conference & Exhibit*. Reston, Virginia: American Institute of Aeronautics and Astronautics, jul 2012. [Online]. Available: <http://arc.aiaa.org/doi/abs/10.2514/6.2012-3704>
- [2] Y. Ju and W. Sun, "Plasma assisted combustion: Dynamics and chemistry," *Progress in Energy and Combustion Science*, vol. 48, pp. 21–83, jun 2015. [Online]. Available: <https://www.sciencedirect.com/science/article/pii/S0360128514000781?via%3Dihub>
- [3] P. Akbari, R. Nalim, and P. Snyder, "Numerical Simulation and Design of a Combustion Wave Rotor for Deflagrative and Detonative Propagation," in *42nd AIAA/ASME/SAE/ASEE Joint Propulsion Conference and Exhibit*. Reston, Virginia: American Institute of Aeronautics and Astronautics, jul 2006. [Online]. Available: <http://arc.aiaa.org/doi/abs/10.2514/6.2006-5134>
- [4] A. Meyer, "Recent Developments in Gas Turbines," *Journal of Mechanical Engineering*, vol. vol. 69, no. no. 4, pp. pp. 273–277, 1947.
- [5] H. Weber, *Shock wave engine design*. John Wiley & Sons, Inc., 1995.
- [6] P. Akbari and N. Mueller, "Wave rotor research program at michigan state university," *41st AIAA/ASME/SAE/ASEE Joint Propulsion Conference and Exhibit*, jul 2005. [Online]. Available: <http://arc.aiaa.org/doi/abs/10.2514/6.2005-3844>
- [7] M. R. Mataczynski, D. E. Paxson, M. D. Polanka, and J. Hoke, "Experimental Performance of a Small Scale Pressure Wave Supercharger," in *54th AIAA Aerospace Sciences Meeting*. Reston, Virginia: American Institute of Aeronautics and Astronautics, jan 2016. [Online]. Available: <http://arc.aiaa.org/doi/10.2514/6.2016-0768>
- [8] M. Mataczynski, D. E. Paxson, J. Hoke, and F. Schauer, "Design and Testing of a Small Pressure Wave Supercharger for an Industrial Diesel Engine," in *55th AIAA Aerospace Sciences Meeting*. Reston, Virginia: American Institute of Aeronautics and Astronautics, jan 2017. [Online]. Available: <http://arc.aiaa.org/doi/10.2514/6.2017-1624>
- [9] M. R. Nalim, P. H. Snyder, and M. Kowalkowski, "Experimental Test, Model Validation, and Viability Assessment of a Wave-Rotor Constant-Volume Combustor," *Journal of Propulsion and Power*, vol. 33, no. 1, pp. 163–175, jan 2017. [Online]. Available: <http://arc.aiaa.org/doi/10.2514/1.B36174>

- [10] A. Mathur, R. P. Shreeve, and S. Eidelman, "Numerical Techniques for Wave Rotor Cycle Analysis," *American Society of Mechanical Engineers, Fluids Engineering Division (Publication) FED, Presented at the 1984 Winter Annual Meeting of the American Society of Mechanical Engineers, USA.*, vol. 15, 1984.
- [11] D. E. Paxson, "A General Numerical Model for Wave Rotor Analysis," *NASA STI/Recon Technical Report N 92 TM 31484*, 1992. [Online]. Available: <https://ntrs.nasa.gov/search.jsp?R=19920022240>
- [12] D. Paxson, "An incidence loss model for wave rotors with axially aligned passages," in *34th AIAA/ASME/SAE/ASEE Joint Propulsion Conference and Exhibit*. Reston, Virginia: American Institute of Aeronautics and Astronautics, jul 1998. [Online]. Available: <http://arc.aiaa.org/doi/10.2514/6.1998-3251>
- [13] G. E. Welch, "Two-dimensional computational model for wave rotor flow dynamics," *ASME 1996 International Gas Turbine and Aeroengine Congress and Exhibition.*, 1996. [Online]. Available: <http://proceedings.asmedigitalcollection.asme.org/proceeding.aspx?articleid=2110219>
- [14] J. Wilson, G. Welch, and D. Paxson, "Experimental Results of Performance Tests on a Four-Port Wave Rotor," in *45th AIAA Aerospace Sciences Meeting and Exhibit*. Reston, Virginia: American Institute of Aeronautics and Astronautics, jan 2007. [Online]. Available: <http://arc.aiaa.org/doi/10.2514/6.2007-1250>
- [15] J. Wilson, "An experimental determination of losses in a three-port wave rotor," *Transactions-American Society of Mechanical Engineers Journal of Engineering For Gas Turbines And Power*, vol. 120, pp. 833–842, 1998.
- [16] P. Akbari, R. Nalim, and N. Mueller, "A Review of Wave Rotor Technology and Its Applications," *Journal of Engineering for Gas Turbines and Power*, vol. 128, no. 4, p. 717, 2006. [Online]. Available: <http://gasturbinespower.asmedigitalcollection.asme.org/article.aspx?articleid=1424189>
- [17] P. Akbari and R. Nalim, "Review of Recent Developments in Wave Rotor Combustion Technology," *Journal of Propulsion and Power*, vol. 25, no. 4, pp. 833–844, jul 2009. [Online]. Available: <http://arc.aiaa.org/doi/10.2514/1.34081>
- [18] T. Elharis, S. Wijeyakulasuriya, and M. Nalim, "A Two-Step Reaction Model for Stratified-Charge Combustion in Wave-Rotors," in *47th AIAA/ASME/SAE/ASEE Joint Propulsion Conference and Exhibit*. Reston, Virginia: American Institute of Aeronautics and Astronautics, jul 2011. [Online]. Available: <http://arc.aiaa.org/doi/abs/10.2514/6.2011-5748>
- [19] T. Elharis, *A multi-step reaction model for stratified charge combustion in wave rotors*. ProQuest Dissertations and Theses, 2011. [Online]. Available: <http://search.proquest.com/openview/d6bb2882ab9fb6ff0395e1f3c1efa192/1?pq-origsite=gscholar&cbl=18750&diss=y>
- [20] R. R. Jagannath, S. P. M. Bane, and M. R. Nalim, "Wave Rotor Combustor Turbine Model Development," in *51st AIAA/SAE/ASEE Joint Propulsion Conference*. Reston, Virginia: American Institute of Aeronautics and Astronautics, jul 2015. [Online]. Available: <http://arc.aiaa.org/doi/10.2514/6.2015-4188>

- [21] A. Karimi, M. Rajagopal, and M. R. Nalim, "Traversing hot-jet ignition in a constant-volume combustor," *Journal of Engineering for Gas Turbines and Power*, vol. 136, no. 4, p. 041506, 2014.
- [22] A. Karimi and M. R. Nalim, "Ignition by Hot Transient Jets in Confined Mixtures of Gaseous Fuels and Air," *Journal of Combustion*, vol. 2016, no. 9565839, 2016.
- [23] V. Kilchyk, M. R. Nalim, and C. Merkle, "Scaling interface length increase rates in RichtmyerMeshkov instabilities," *ASME Journal of Fluids Engineering*, vol. 135, no. 3, p. 031203, 2013. [Online]. Available: <http://proceedings.asmedigitalcollection.asme.org/article.aspx?articleid=1677149>
- [24] Y. Matsutomi, S. Meyer, S. Wijeyakulasuriya, Z. Izzy, M. Nalim, M. Shimo, M. Kowalkowski, and P. Snyder, "Experimental Investigation on the Wave Rotor Constant Volume Combustor," in *46th AIAA/ASME/SAE/ASEE Joint Propulsion Conference and Exhibit*. Reston, Virginia: American Institute of Aeronautics and Astronautics, jul 2010. [Online]. Available: <http://arc.aiaa.org/doi/abs/10.2514/6.2010-7043>
- [25] M. R. Nalim, "Longitudinally Stratified Combustion in Wave Rotors," *Journal of Propulsion and Power*, vol. 16, no. 6, pp. 1060–1068, nov 2000. [Online]. Available: <http://arc.aiaa.org/doi/10.2514/2.5676>
- [26] M. Razi Nalim, "Thermodynamic Limits of Work and Pressure Gain in Combustion and Evaporation Processes," *Journal of Propulsion and Power*, vol. 18, no. 6, pp. 1176–1182, nov 2002. [Online]. Available: <http://arc.aiaa.org/doi/10.2514/2.6076>
- [27] M. R. Nalim, H. Li, and P. Akbari, "Air-standard aerothermodynamic analysis of gas turbine engines with wave rotor combustion," *ASME Journal of Engineering for Gas Turbines and Power*, vol. 131, no. 5, p. 054506, 2009. [Online]. Available: <http://appliedmechanics.asmedigitalcollection.asme.org/article.aspx?articleid=1427722>
- [28] G. E. Welch and L. Larosiliere, "Passage-averaged description of wave rotor flow," in *33rd Joint Propulsion Conference and Exhibit*. Reston, Virginia: American Institute of Aeronautics and Astronautics, jul 1997. [Online]. Available: <http://arc.aiaa.org/doi/10.2514/6.1997-3144>
- [29] G. E. Welch and D. E. Paxson, "Wave turbine analysis tool development," in *34th AIAA/ASME/SAE/ASEE Joint Propulsion Conference and Exhibit*. Reston, Virginia: American Institute of Aeronautics and Astronautics, jul 1998. [Online]. Available: <http://arc.aiaa.org/doi/10.2514/6.1998-3402>
- [30] Paxson D E, "Comparison between numerically modeled and experimentally measured wave-rotor loss mechanisms," *arc.aiaa.org*, vol. 11, no. 5, pp. 908–914, 1995. [Online]. Available: <https://arc.aiaa.org/doi/abs/10.2514/3.23916>
- [31] R. R. Jagannath, S. P. M. Bane, and M. Razi Nalim, "Numerical Modeling of a Wave Turbine and Estimation of Shaft Work," *Journal of Fluids Engineering*, vol. 140, no. 10, p. 101106, may 2018.
- [32] L. M. Larosiliere, "Wave rotor charging process - Effects of gradual opening and rotation," *Journal of Propulsion and Power*, vol. 11, no. 1, pp. 178–184, jan 1995. [Online]. Available: <http://arc.aiaa.org/doi/10.2514/3.23856>

- [33] A. Karimi, M. Rajagopal, and R. Nalim, "Traversing Hot-Jet Ignition in a Constant-Volume Combustor," *Journal of Engineering for Gas Turbines and Power*, vol. 136, no. 4, p. 041506, dec 2013.
- [34] D. Z. Pai, D. A. Lacoste, and C. O. Laux, "Transitions between corona, glow, and spark regimes of nanosecond repetitively pulsed discharges in air at atmospheric pressure," *Journal of Applied Physics*, vol. 107, no. 9, p. 093303, may 2010. [Online]. Available: <http://aip.scitation.org/doi/10.1063/1.3309758>
- [35] A. Starikovskiy, A. Rakitin, G. Correale, A. Nikipelov, T. Urushihara, and T. Shiraishi, "Ignition of Hydrocarbon-Air Mixtures with Non-Equilibrium Plasma at Elevated Pressures," in *50th AIAA Aerospace Sciences Meeting including the New Horizons Forum and Aerospace Exposition*, 2012. [Online]. Available: <http://arc.aiaa.org>
- [36] W. J. Yi and P. F. Williams, "Experimental study of streamers in pure N₂ and N₂/O₂ mixtures and a 13 cm gap," *Journal of Physics D: Applied Physics*, vol. 35, no. 3, pp. 205–218, feb 2002. [Online]. Available: <http://stacks.iop.org/0022-3727/35/i=3/a=308?key=crossref.f28a54b5efcb07b9c00a4c7135906816>
- [37] C. Jiang, M. T. Chen, and M. A. Gundersen, "Polarity-induced asymmetric effects of nanosecond pulsed plasma jets," *Journal of Physics D: Applied Physics*, vol. 42, no. 23, p. 232002, dec 2009. [Online]. Available: <http://stacks.iop.org/0022-3727/42/i=23/a=232002?key=crossref.93f4596ef6aab2dd42997f3dbf482b9>
- [38] R. R. Jagannath, K. Newnam, P. W. Stockett, P. Wu, S. P. M. Bane, and M. R. Nalim, "Volumetric Plasma Discharge in a Coaxial Electrode Configuration Using Repetitively Pulsed Nanosecond Discharges," in *AIAA SciTech Forum*, Grapevine, Texas, 2017. [Online]. Available: <http://arc.aiaa.org>
- [39] G. Perrott and D. Gawthrop, "Photographic measurement of rate of detonation of explosives," *Journal of the Franklin Institute*, vol. 203, no. 1, pp. 103–110, jan 1927. [Online]. Available: <https://www.sciencedirect.com/science/article/pii/S001600322790101X>
- [40] I. Vigness and R. C. Nowak, "Streak Photography," *Journal of Applied Physics*, vol. 21, no. 5, pp. 445–448, may 1950. [Online]. Available: <http://aip.scitation.org/doi/10.1063/1.1699682>
- [41] E. G. Whitbread, "A High-speed Rotating Mirror Camera," Explosives Research & Development Establishment, Tech. Rep., 1949.
- [42] H. E. Ives and N. J. Montclair, "Electron camera," sep 1940. [Online]. Available: <https://patents.google.com/patent/US2315621A/en>
- [43] D. J. Bradley and S. Majumdar, "A New Electron Image Time Dissector Framing Camera for High Speed Photography in the Nanosecond Region," *The Journal of Photographic Science*, vol. 14, no. 3, pp. 134–142, 1966. [Online]. Available: <http://www.tandfonline.com/action/journalInformation?journalCode=yims19>
- [44] D. Bradley, B. Liddy, and W. Sleat, "Direct linear measurement of ultrashort light pulses with a picosecond streak camera," *Optics Communications*, vol. 2, no. 8, pp. 391–395, jan 1971. [Online]. Available: <https://www.sciencedirect.com/science/article/pii/0030401871902525>

- [45] D. J. Bradley, A. J. F. Durrant, F. O’neill, and B. Sutherland, “PICOSECOND PULSES FROM MODE-LOCKED DYE LASERS,” *PHYSICS LETTERS*, vol. 30A, no. 9, pp. 535–536, 1969. [Online]. Available: https://ac.els-cdn.com/0375960169902928/1-s2.0-0375960169902928-main.pdf?_tid=fc0117dc-a127-440c-acaf-d90d80af65b2&acdnat=1537883768_351708ac6411659ea8018d635902aae4
- [46] D. Bradley, “Electron-optical image tubes,” jul 1973. [Online]. Available: <https://patents.google.com/patent/US3973117A/en>
- [47] K. Kinoshita and Y. Suzuki, “Streak Tube With Microchannel Plate,” in *13th Intl Congress on High Speed Photography and Photonics International Society for Optics and Photonics.*, S.-I. Hyodo, Ed., vol. 0189. International Society for Optics and Photonics, jul 1979, pp. 504–507. [Online]. Available: <http://proceedings.spiedigitallibrary.org/proceeding.aspx?articleid=1228780>
- [48] Y. Tsuchiya, E. Inuzuka, Y. Suzuki, and W. Yu, “Ultrafast Streak Camera,” in *13th Intl Congress on High Speed Photography and Photonics*, S.-I. Hyodo, Ed., vol. 0189. International Society for Optics and Photonics, jul 1979, pp. 517–520. [Online]. Available: <http://proceedings.spiedigitallibrary.org/proceeding.aspx?articleid=1228783>
- [49] Y. Suzuki, Y. T. Suchiya, K. K. Inoshita, M. Sugiyama, and E. I. Nuzuka, “Recent developments in picosecond streak camera systems,” *Trans. R. Soc. Lond. A*, vol. 298, pp. 295–302, 1980. [Online]. Available: <http://rsta.royalsocietypublishing.org/>
- [50] Y. Tsuchiya, “Advances in streak camera instrumentation for the study of biological and physical processes,” *IEEE Journal of Quantum Electronics*, vol. 20, no. 12, pp. 1516–1528, dec 1984. [Online]. Available: <http://ieeexplore.ieee.org/document/1072316/>
- [51] C. B. Johnson, “Photoelectronic Streak-Tube Technology Review,” in *High Speed Optical Techniques: Developments and Applications.*, M. A. Duguay and R. K. Petersen, Eds., vol. 0094. International Society for Optics and Photonics, jan 1977, pp. 13–18. [Online]. Available: <http://proceedings.spiedigitallibrary.org/proceeding.aspx?articleid=1226104>
- [52] V. V. Korobkin, B. M. Stepanov, S. D. Fanchenko, and M. Y. Schelev, “Pico-femtosecond electron-optical photography,” *Optical and Quantum Electronics*, vol. 10, no. 5, pp. 367–381, sep 1978. [Online]. Available: <http://link.springer.com/10.1007/BF00620303>
- [53] A. Campillo and S. Shapiro, “Picosecond streak camera fluorometry - A review,” *IEEE Journal of Quantum Electronics*, vol. 19, no. 4, pp. 585–603, apr 1983. [Online]. Available: <http://ieeexplore.ieee.org/document/1071909/>
- [54] Hamamatsu Photonics K. K., “High dynamic range streak camera C13410 series Temporal resolution less than 100 ps,” Hamamatsu Photonics K. K., Tech. Rep., 2018. [Online]. Available: https://www.hamamatsu.com/resources/pdf/sys/SHSS0021E_C13410.pdf
- [55] N. Aleksandrov, G. Ivanov, S. Kindysheva, I. Kosarev, P. Sagulenko, S. Starikovskaia, and A. Starikovskii, “Kinetics of Plasma Assisted

- Ignition at Elevated Temperatures: Experiments and Modelling,” in *46th AIAA Aerospace Sciences Meeting and Exhibit*. Reston, Virginia: American Institute of Aeronautics and Astronautics, jan 2008. [Online]. Available: <http://arc.aiaa.org/doi/10.2514/6.2008-1363>
- [56] A. E. Rakitin and A. Y. Starikovskii, “Mechanisms of deflagration-to-detonation transition under initiation by high-voltage nanosecond discharges,” *Combustion and Flame*, vol. 155, no. 1-2, pp. 343–355, oct 2008. [Online]. Available: <https://www.sciencedirect.com/science/article/pii/S001021800800179X>
- [57] P. H. Ceccato, O. Guaitella, M. R. Le Gloahec, and A. Rousseau, “Time-resolved nanosecond imaging of the propagation of a corona-like plasma discharge in water at positive applied voltage polarity,” *Journal of Physics D: Applied Physics*, vol. 43, no. 17, p. 175202, may 2010. [Online]. Available: <http://stacks.iop.org/0022-3727/43/i=17/a=175202?key=crossref.462f85770ffe201b93cfb03221bcd812>
- [58] K. D. Batrakov, A. V., Popov, S. A., Methling, R., Uhrlandt, D., & Weltmann, “Time-and spectrum-resolved study of a single cathode spot in vacuum,” *IEEE Transactions on Plasma Science*, vol. 39, no. 6, pp. 1296–1302, 2011. [Online]. Available: http://www.conferences-2008.hcei.tsc.ru/cat/proc_2008/shce/140-143.pdf
- [59] R. J. Thomas, D. X. Hammer, G. D. Noojin, D. J. Stolarski, B. A. Rockwell, and W. P. Roach, “Time-resolved spectroscopy of laser- induced breakdown in water,” *PROCEEDINGS OF SPIE*, no. May 1996, 2018.
- [60] R. R. Jagannath, A. Satija, R. P. Lucht, and S. P. M. Bane, “Characterization of time-resolved emission of N₂ (C) in an atmospheric pressure nanosecond pulsed air-plasma using streak spectroscopy,” *Plasma Sources Science and Technology*, vol. 28, no. 1, p. 01LT02, jan 2019. [Online]. Available: <http://stacks.iop.org/0963-0252/28/i=1/a=01LT02?key=crossref.ba90ec37361e66e9b9e312f8b5a8a328>
- [61] R. R. Jagannath, A. Satija, N. Numa, P. W. Stockett, N. Y. Joel, R. P. Lucht, and S. P. M. Bane, “Application of a Streak Camera for Optical Diagnostics of Nanosecond Repetitively Pulsed Plasma Discharges,” in *AIAA SciTech Forum*, San Diego, California, 2019. [Online]. Available: <http://arc.aiaa.org>
- [62] “Specair 3.0.” [Online]. Available: <http://www.specair-radiation.net>
- [63] C. O. Laux, T. G. Spence, C. H. Kruger, and R. N. Zare, “Optical diagnostics of atmospheric pressure air plasmas,” *Plasma Sources Science and Technology*, vol. 12, no. 2, pp. 125–138, may 2003. [Online]. Available: <http://stacks.iop.org/0963-0252/12/i=2/a=301?key=crossref.c1d6e6ee041199344a20baea814fcdac>
- [64] F. Tholin and A. Bourdon, “Simulation of the hydrodynamic expansion following a nanosecond pulsed spark discharge in air at atmospheric pressure,” *Journal of Physics D: Applied Physics*, vol. 46, no. 36, p. 365205, sep 2013. [Online]. Available: <http://stacks.iop.org/0022-3727/46/i=36/a=365205?key=crossref.fc1a6bb8ec1f39efc85364604e456d82>

- [65] I. Kimura, H. Aoki, and M. Kato, "The use of a plasma jet for flame stabilization and promotion of combustion in supersonic air flows," *Combustion and Flame*, vol. 42, pp. 297–305, jan 1981. [Online]. Available: <https://www.sciencedirect.com/science/article/pii/0010218081901644>
- [66] E. BARBI, J. R. MAHAN, W. O'BRIEN, and T. C. WAGNER, "Operating characteristics of a hydrogen-argon plasma torch for supersonic combustion applications," *Journal of Propulsion and Power*, vol. 5, no. 2, pp. 129–133, mar 1989. [Online]. Available: <http://arc.aiaa.org/doi/10.2514/3.23126>
- [67] T. C. WAGNER, W. F. O'BRIEN, G. B. NORTHAM, and J. M. EGGERS, "Plasma torch igniter for scramjets," *Journal of Propulsion and Power*, vol. 5, no. 5, pp. 548–554, sep 1989. [Online]. Available: <http://arc.aiaa.org/doi/10.2514/3.23188>
- [68] K. Takita, "Ignition and flame-holding by oxygen, nitrogen and argon plasma torches in supersonic airflow," *Combustion and Flame*, vol. 128, no. 3, pp. 301–313, feb 2002. [Online]. Available: <https://www.sciencedirect.com/science/article/pii/S0010218001003546>
- [69] K. Kobayashi, S. Tomioka, and T. Mitani, "Supersonic Flow Ignition by Plasma Torch and H₂/O₂ Torch," *Journal of Propulsion and Power*, vol. 20, no. 2, pp. 294–301, mar 2004. [Online]. Available: <http://arc.aiaa.org/doi/10.2514/1.1760>
- [70] K. Takita, N. Abe, G. Masuya, and Y. Ju, "Ignition enhancement by addition of NO and NO₂ from a N₂/O₂ plasma torch in a supersonic flow," *Proceedings of the Combustion Institute*, vol. 31, no. 2, pp. 2489–2496, jan 2007. [Online]. Available: <https://www.sciencedirect.com/science/article/pii/S1540748906001179>
- [71] L. S. Jacobsen, C. D. Carter, R. A. Baurle, T. A. Jackson, S. Williams, D. Bivolaru, S. Kuo, J. Barnett, and C.-J. Tam, "Plasma-Assisted Ignition in Scramjets," *Journal of Propulsion and Power*, vol. 24, no. 4, pp. 641–654, jul 2008. [Online]. Available: <http://arc.aiaa.org/doi/10.2514/1.27358>
- [72] S. B. Leonov, D. A. Yarantsev, A. P. Napartovich, and I. V. Kochetov, "Plasma-Assisted Combustion of Gaseous Fuel in Supersonic Duct," *IEEE Transactions on Plasma Science*, vol. 34, no. 6, pp. 2514–2525, dec 2006. [Online]. Available: <http://ieeexplore.ieee.org/document/4032894/>
- [73] S. B. Leonov and D. A. Yarantsev, "Plasma-induced ignition and plasma-assisted combustion in high-speed flow," *Plasma Sources Science and Technology*, vol. 16, no. 1, pp. 132–138, feb 2007. [Online]. Available: <http://stacks.iop.org/0963-0252/16/i=1/a=018?key=crossref.0a2cc932c4c3348d287ca79e3c4227da>
- [74] I. Esakov, L. Grachev, K. Khodataev, and D. Van Wie, "Experiments on Propane Ignition in High-Speed Airflow Using a Deeply Under Critical Microwave Discharge," in *42nd AIAA Aerospace Sciences Meeting and Exhibit*, 2004. [Online]. Available: <http://arc.aiaa.org>
- [75] H. Do, S.-k. Im, M. A. Cappelli, and M. G. Mungal, "Plasma assisted flame ignition of supersonic flows over a flat wall," *Combustion and Flame*, vol. 157, no. 12, pp. 2298–2305, dec 2010. [Online]. Available: <https://www.sciencedirect.com/science/article/pii/S001021801000194X>

- [76] A. Hicks, S. Norberg, P. Shawcross, W. R. Lempert, J. W. Rich, and I. V. Adamovich, "Singlet oxygen generation in a high pressure non-self-sustained electric discharge," *Journal of Physics D: Applied Physics*, vol. 38, no. 20, pp. 3812–3824, oct 2005. [Online]. Available: <http://stacks.iop.org/0022-3727/38/i=20/a=007?key=crossref.30653fbf4819e225b533da60dcc3a1fa>
- [77] A. Starikovskiy and N. Aleksandrov, "Plasma-assisted ignition and combustion," *Progress in Energy and Combustion Science*, vol. 39, no. 1, pp. 61–110, feb 2013. [Online]. Available: <https://www.sciencedirect.com/science/article/pii/S0360128512000354>
- [78] N. L. Aleksandrov, S. V. Kindysheva, I. N. Kosarev, S. M. Starikovskaia, and A. Y. Starikovskii, "Mechanism of ignition by non-equilibrium plasma," *Proceedings of the Combustion Institute*, vol. 32 I, no. 1, pp. 205–212, 2009. [Online]. Available: <http://dx.doi.org/10.1016/j.proci.2008.06.124>
- [79] M. A. Boumehdi, S. A. Stepanyan, P. Desgroux, G. Vanhove, and S. M. Starikovskaia, "Ignition of methane- and n-butane-containing mixtures at high pressures by pulsed nanosecond discharge," *Combustion and Flame*, vol. 162, no. 4, pp. 1336–1349, 2015. [Online]. Available: <http://dx.doi.org/10.1016/j.combustflame.2014.11.006>
- [80] I. N. Kosarev, N. L. Aleksandrov, S. V. Kindysheva, S. M. Starikovskaia, and A. Y. Starikovskii, "Kinetic mechanism of plasma-assisted ignition of hydrocarbons," *Journal of Physics D: Applied Physics*, vol. 41, no. 3, 2008.
- [81] N. Tsolas, J. G. Lee, and R. A. Yetter, "Flow reactor studies of plasma-assisted oxidation of n -alkanes Author for correspondence :," *Phil. Trans. R. Soc . A*, vol. 373, no. 20140344, 2015.
- [82] Y. Matsubara, K. Takita, and G. Masuya, "Combustion enhancement in a supersonic flow by simultaneous operation of DBD and plasma jet," *Proceedings of the Combustion Institute*, vol. 34, no. 2, pp. 3287–3294, jan 2013. [Online]. Available: <https://www.sciencedirect.com/science/article/pii/S1540748912002921>
- [83] S. B. Leonov, D. A. Yarantsev, A. P. Napartovich, and I. V. Kochetov, "Plasma-Assisted Ignition and Flameholding in High-Speed Flow," in *44th AIAA Aerospace Sciences Meeting and Exhibit*, 2006. [Online]. Available: <http://arc.aiaa.org>
- [84] K. Busby, J. Corrigan, S.-T. Yu, S. Williams, C. Carter, F. Schauer, J. Hoke, C. Cathey, and M. Gundersen, "Effects of Corona, Spark and Surface Discharges on Ignition Delay and Deflagration-to-Detonation Times in Pulsed Detonation Engines," in *45th AIAA aerospace sciences meeting including the new horizons forum and aerospace exposition*, Reno, Nevada, 2007. [Online]. Available: <http://arc.aiaa.org>
- [85] J. Lefkowitz, Y. Ju, C. Stevens, J. Hoke, T. Ombrello, and F. Schauer, "The Effects of Repetitively Pulsed Nanosecond Discharges on Ignition Time in a Pulsed Detonation Engine," in *49th AIAA/ASME/SAE/ASEE joint propulsion conference*, San Jose, CA, 2013. [Online]. Available: <http://arc.aiaa.org>
- [86] T. Shiraishi, T. Urushihara, and M. Gundersen, "A trial of ignition innovation of gasoline engine by nanosecond pulsed low temperature plasma ignition," *Journal of Physics D: Applied Physics*, vol. 42,

- no. 13, p. 135208, jul 2009. [Online]. Available: <http://stacks.iop.org/0022-3727/42/i=13/a=135208?key=crossref.ca3de4c68423373ee9d128209f885733>
- [87] Fei Wang, J. Liu, J. Sinibaldi, C. Brophy, A. Kuthi, C. Jiang, P. Ronney, and M. Gundersen, "Transient plasma ignition of quiescent and flowing air/fuel mixtures," *IEEE Transactions on Plasma Science*, vol. 33, no. 2, pp. 844–849, apr 2005. [Online]. Available: <http://ieeexplore.ieee.org/document/1420629/>
- [88] C. D. Cathey, T. Tang, T. Shiraishi, T. Urushihara, A. Kuthi, and M. A. Gundersen, "Nanosecond Plasma Ignition for Improved Performance of an Internal Combustion Engine," *IEEE Transactions on Plasma Science*, vol. 35, no. 6, pp. 1664–1668, dec 2007. [Online]. Available: <http://ieeexplore.ieee.org/document/4392536/>
- [89] G. Herdin, J. Klausner, E. Wintner, M. Weinrotter, J. Graf, and K. Iskra, "Laser Ignition: A New Concept to Use and Increase the Potentials of Gas Engines," in *ASME 2005 Internal Combustion Engine Division Fall Technical Conference (ICEF2005)*. ASME, jan 2005, pp. 673–681. [Online]. Available: <http://proceedings.asmedigitalcollection.asme.org/proceeding.aspx?articleid=1586997>
- [90] A. Mariani and F. Foucher, "Radio frequency spark plug: An ignition system for modern internal combustion engines," *Applied Energy*, vol. 122, pp. 151–161, jun 2014. [Online]. Available: <https://www.sciencedirect.com/science/article/pii/S0306261914001287>
- [91] Q. Wang, G. Zhang, Y. Liu, L. Hou, C. Liu, Z. Wang, and J. Huang, "Visual features of microwave ignition of methane-air mixture in a constant volume cylinder," *Applied Physics Letters*, vol. 103, no. 20, p. 204104, nov 2013. [Online]. Available: <http://aip.scitation.org/doi/10.1063/1.4830272>
- [92] B. Wolk, A. DeFilippo, J.-Y. Chen, R. Dibble, A. Nishiyama, and Y. Ikeda, "Enhancement of flame development by microwave-assisted spark ignition in constant volume combustion chamber," *Combustion and Flame*, vol. 160, no. 7, pp. 1225–1234, jul 2013. [Online]. Available: <https://www.sciencedirect.com/science/article/pii/S0010218013000461>
- [93] W. Kim, H. Do, M. G. Mungal, and M. A. Cappelli, "A Study of Plasma-Stabilized Diffusion Flames at Elevated Ambient Temperatures," *IEEE Transactions on Plasma Science*, vol. 36, no. 6, pp. 2898–2904, dec 2008. [Online]. Available: <http://ieeexplore.ieee.org/document/4694052/>
- [94] I. V. Adamovich, I. Choi, N. Jiang, J.-H. Kim, S. Keshav, W. R. Lempert, E. Mintusov, M. Nishihara, M. Samimy, and M. Uddi, "Plasma assisted ignition and high-speed flow control: non-thermal and thermal effects," *Plasma Sources Science and Technology*, vol. 18, no. 3, p. 034018, aug 2009. [Online]. Available: <http://stacks.iop.org/0963-0252/18/i=3/a=034018?key=crossref.7505a9d74bdf89f850a532d4d00bbc3e>
- [95] C. Cathey, F. Wang, T. Tang, A. Kuthi, M. Gundersen, J. Sinibaldi, C. Brophy, E. Barbour, R. Hanson, J. Hoke, F. Schauer, J. Corrigan, and J. Yu, "Transient Plasma Ignition for Delay Reduction in Pulse Detonation Engines," in *45th AIAA Aerospace Sciences Meeting and Exhibit*. Reston, Virginia: American Institute of Aeronautics and Astronautics, jan 2007. [Online]. Available: <http://arc.aiaa.org/doi/10.2514/6.2007-443>

- [96] X. Gu, M. Haq, M. Lawes, and R. Woolley, "Laminar burning velocity and Markstein lengths of methane-air mixtures," *Combustion and Flame*, vol. 121, no. 1-2, pp. 41-58, apr 2000. [Online]. Available: <https://www.sciencedirect.com/science/article/pii/S001021809900142X>